Universidade de São Paulo
Instituto de Astronomia, Geofísica e Ciências Atmosféricas
Departamento de Astronomia

Saqib Hussain

Cosmic Ray Propagation in Galaxy Clusters and the Production of Gamma Rays and Neutrinos

Propagação de Raios Cósmicos em Aglomerados de Galáxias e a Produção de Raios Gama e Neutrinos

Versão Corrigida. O original encontra-se disponível na Unidade.

São Paulo

2022

Saqib Hussain

Cosmic Ray Propagation in Galaxy Clusters and the Production of Gamma Rays and Neutrinos

Propagação de Raios Cósmicos em Aglomerados de Galáxias e a Produção de Raios Gama e Neutrinos

Tese apresentada ao Departamento de Astronomia do Instituto de Astronomia, Geofísica e Ciências Atmosféricas da Universidade de São Paulo como requisito parcial para obtenção do título de **Doutor em Ciências.**

Área de Concentração: Astronomia

Orientador: Profa. Elisabete M. de Gouveia Dal Pino

Versão Corrigida. O original encontra-se disponível na Unidade.

São Paulo

2022

This thesis is dedicated to my friends and family in Pakistan and Brazil.

Acknowledgements

Writing down the work of my PhD is comparatively easier than putting down in everyday words my gratitude to whom accompanied me in the process. These words are my unsatisfactory attempt.

To Prof. Elisabete M. de Gouveia Dal Pino, my advisor, who always guided me with a lot of patience, optimism, and wisdom. For always caring about my career (and that of all her students) in spite of her other obligations; your unlimited commitment is a great help for me. I am deeply indebted with all her help, and motivation. Thanks for all the knowledge and enthusiasm you transmitted me!

To Rafael Alves Batista, who always instructed me with a lot of patience and prudence. He is always concerned about my professional development and consistency in the work. He actually play a key role in the accomplishment of this thesis, without his help it would be very difficult to complete.

To the professors of the Astronomy Department, in special the ones who participated directly of my scientific formation through their courses and advises: Elisabete de Gouveia Dal Pino, Eduardo Cypriano, Claudia Mendes de Oliveira, Reinaldo Santos de Lima, Antonio Mario Magalhaes, Zulema Abraham, Silvia Rossi.

To the staff of the Astronomy Department for all their support, in particular: Regina Iacovelli, Ulisses Manzo, who were always so attentive and nice with me. To the staff of the IAG, in special the very efficient secretaries of the Graduation Office: Ana Carolina, Lilian and Marcel Yoshio.

I acknowledge support from the Brazilian funding agency CNPq. I am very tankful to Klaus Dolag for sharing his cosmological MHD simulations which were used in this thesis. The numerical simulations used in this thesis were performed in the cluster of the

Group of Plasmas and High-Energy Astrophysics (GAPAE), acquired with support from FAPESP (grant $2013/10559-5$). This work also made use of the computing facilities of the Laboratory of Astroinformatics (IAG/USP, NAT/Unicsul), whose purchase was also made possible by FAPESP too (grant $2009/54006-4$).

To all the members of the group (GAPAE) for discussing my work, sharing their knowledge, their incentive and friendship: Reinaldo Santos-Lima, Luis Kadowaki, Chandra Singh, Maria Victoria, Juan Carlos Rodriguez Ramirez, Lucas Barreto Mota dos Santos, Stelinha Adduci, Svetlana Kocheleva, Tania Medina Torrejon, William Eduardo Clavijo Bohorquez, Luciana Andrade Dourado, Camila Naomi Koshikumo, Francisco Junqueira, Gabriel Sampaio Neder, Giovani Heinzen Vicentin, Anderson da Costa Ferreira, Luana Passos Reis, and Maita Carvalho Micol

Thanks to my Pakistani friends in Brazil Irfan, Aamir, and Usama, specially the last two I spent more time together.

I acknowledge my parents Muhammad Hussain and Kaniz Fatima, for their encouragement, invaluable support, and wisdom, especially helping me to understand the original meaning of achievements in life. To my grandparents, because their love and the memories of my childhood have definitely shaped my nature.

I acknowledge my family, for their love and support: my brothers Asif and Sohaib, my sisters Verdha, Sobia, Iqra, Tehreem, and Mateen, my brothers in law Mehmood, Faisal, and Anjum.

This thesis/dissertation was written in LaTeX with the IAGTESE class, for IAG theses and dissertations.

"*And He it is who has made the stars for you that you may follow the right direction with their help amid the deep darkness of the land and the sea. We have explained the signs in details for a people who possesses knowledge.* "

"Holy Quran, An'am-98"

Abstract

The origin of ultra-high-energy cosmic-rays (UHECRs), diffuse neutrino, and gamma-ray background is among the major mysteries in astrophysics. The diffuse gamma-ray background (DGRB) corresponds to the one that remains after subtracting all individual sources from observed gamma-ray sky. The DGRB provides a non-thermal perspective of the universe that is also explored through the extragalactic UHECRs and neutrinos. The observed energy fluxes of these three components are all comparable suggesting that they may have a common origin. Several types of astrophysical sources have been predicted as the contributors to high-energy multi-messengers. They possibly have contributions from different source populations such as star-forming galaxies (SFGs), pulsars, active galactic nuclei (AGNs), gamma-ray bursts (GRBs), and from galaxy clusters.

In particular, clusters of galaxies can potentially produce cosmic rays (CRs) up to very-high energies via large-scale shocks and turbulent acceleration. Due to their unique magnetic-field configuration and large size, CRs with energy $\leq 10^{17}$ eV can be trapped within these structures over cosmological time scales, and generate secondary particles, including neutrinos and gamma rays, through interactions with the background gas and photon fields. In this Thesis, we combined three-dimensional (3D) cosmological MHD simulations of clusters of galaxies with the propagation of CRs using Monte Carlo simulations, considering redshifts $z \lesssim 5$, and computed the contribution of clusters to the diffuse background of neutrinos and gamma-rays. We used the distribution of clusters within this cosmological volume to extract their properties, including mass, magnetic field, temperature, and density. We propagated CRs in this environment considering all relevant photohadronic, photonuclear, and hadronuclear interaction processes. We have found that for CRs injected with a fraction $\sim (0.5 - 3)\%$ of the clusters luminosity, spec-

tral power law indices $\alpha = 1.5 - 2.7$ and cutoff energy $E_{\rm max} = (10^{16} - 5 \times 10^{17})$ eV, the clusters contribute to a sizeable fraction of the diffuse flux of neutrinos observed by the IceCube, but most of the contribution comes from clusters with $M \gtrsim 10^{14}\ M_\odot$ and redshift $z \lesssim 0.3$. This contribution is even higher when we include the cosmological evolution of the CR sources, namely, AGNs and star-forming regions. Similarly, for the integrated diffuse gamma-ray flux, we have found that the clusters can contribute to up to 100% of the diffuse gamma-ray flux observed by the Fermi-LAT above 100 GeV, for CR injection power corresponding to $\sim 1\%$ of the clusters luminosity, spectral indices $\alpha = 1.5 - 2.5$ and energy cutoff $E_{\rm max} = (10^{16} - 10^{17})$ eV. The flux is dominated by clusters with mass $10^{13} < M/M_\odot < 10^{15}$ in the redshift range $z \lesssim 0.3$. Our results also predict the potential observation of high-energy gamma rays from clusters by experiments like HAWC, LHAASO and even the upcoming CTA.

We believe that this work has provided important new results in the area of gamma-ray and multi-messenger astrophysics. Firstly, they are a step forward computationally, as they comprise the most detailed calculations to date of this type of process, employing techniques that are rarely used together (3D simulations of particle propagation with cosmological MHD simulations). Secondly, our results provide an estimate of a flux of gamma rays and neutrinos from galaxy clusters that should be taken into account when interpreting the diffuse gamma-ray and neutrino background. This has immediate implications for all studies that depend on accurate estimates of this background, ranging from models of individual extragalactic high-energy gamma-ray and neutrino sources to dark-matter searches. Moreover, our results established a clear connection between the fluxes of these two messengers, which, combined, enables us to indirectly study CRs in clusters even if they are not directly observable.

Resumo

A origem dos raios cósmicos de ultra-alta energia (UHECRs), e da emissão difusa de neutrinos e de raios gama está entre os principais mistérios da astrofísica. O fundo difuso de raios gama (DGRB) corresponde àquele que permanece após subtraírem-se todas as fontes individuais do céu de raios gama observadas. O DGRB fornece uma perspectiva não térmica do universo que também é explorada através dos UHECRs e neutrinos extragalácticos. Os fluxos de energia observados desses três componentes são todos comparáveis, sugerindo que eles podem ter uma origem comum. Vários tipos de fontes astrofísicas foram sugeridas como contribuintes para esses multi-mensageiros de alta energia. Eles possivelmente têm contribuições de diferentes populações, como galáxias com formação de estrelas (SFGs), pulsares, núcleos galácticos ativos (AGNs), surtos de raios gama (GRBs), e de aglomerados de galáxias.

Em particular, aglomerados de galáxias podem potencialmente produzir raios cósmicos (CRs) até energias muito altas por meio de choques de grande escala e aceleração turbulenta. Devido à sua configuração única de campo magnético e grande extensão, os CRs com energia $\leq 10^{17}$ eV podem ficar presos dentro dessas estruturas em escalas de tempo cosmológicas e gerar partículas secundárias, incluindo neutrinos e raios gama, por meio de interações com o gás de fundo e os campos de radiação. Nesta Tese, combinamos simulações MHD cosmológicas tridimensionais (3D) de aglomerados de galáxias com a propagação de CRs usando simulações de Monte Carlo, considerando redshifts $z \lesssim 5$, e computamos a contribuição dos aglomerados para o fundo difuso de neutrinos e raios gama. Usamos a distribuição de aglomerados dentro do volume cosmológico para extrair suas propriedades, incluindo massa, campo magnético, temperatura e densidade. Propagamos os CRs neste ambiente considerando todos os processos relevantes de interação

fotohadrônica, fotonuclear e hadronuclear. Verificamos que para CRs injetados com uma fração $\sim (0,5-3)\%$ da luminosidade dos aglomerados, índices do espectro de lei de potência com índices $\alpha = 1,5-2,7$ e energia de corte $E_{\rm max} = (10^{16} - 5\times10^{17})$ eV, os aglomerados contribuem para uma fração considerável do fluxo difuso de neutrinos observado pelo IceCube, mas a maior parte da contribuição vem de aglomerados com $M \gtrsim 10^{14}\ M_{\odot}$ e redshift $z \lesssim 0.3$. Esta contribuição é ainda maior quando incluímos a evolução cosmológica das fontes de CRs, isto é, AGNs e regiões de formação estelar. Da mesma forma, para o fluxo de raios gama difuso integrado, verificamos que os clusters podem contribuir com até 100% do fluxo de raios gama difuso acima de 100 GeV, observado pelo Fermi-LAT, para potência de injeção de CRs correspondente a $\sim 1\%$ da luminosidade dos clusters, índices espectrais $\alpha = 1,5-2,5$ e energia de corte $E_{\rm max} = (10^{16} - 10^{17})$ eV. O fluxo é dominado por clusters com massa $10^{13} < M/M_{\odot} < 10^{15}$ na faixa de redshift $z \lesssim 0,3$. Nossos resultados também preveem a observação potencial de raios gama de alta energia ($> 10^{12}$ eV) de aglomerados por experimentos como HAWC, LHAASO e até mesmo o próximo CTA.

Acreditamos que este trabalho tenha fornecido novos resultados importantes para a área da astrofísica de raios gama e multi-mensageiros. Em primeiro lugar, eles são um avanço computacional, pois compreendem os cálculos mais detalhados até hoje desse tipo de processo, empregando técnicas raramente usadas em conjunto (simulações 3D de propagação de partículas com simulações MHD cosmológicas). Em segundo lugar, nossos resultados fornecem uma estimativa de um fluxo de raios gama e de neutrinos de aglomerados de galáxias que devem ser levados em consideração ao se interpretar o fundo difuso dessas emissões. Isso tem implicações imediatas para todos os estudos que dependem de estimativas precisas desse fundo, desde modelos de fontes extragalácticas individuais de raios gama e neutrinos de alta energia até pesquisas de matéria escura. Além disso, nossos resultados estabelecem uma conexão clara entre os fluxos desses dois mensageiros, neutrinos e raios gama que, combinados, permitem-nos estudar indiretamente CRs em aglomerados, mesmo que não sejam diretamente observáveis.

Contents

List of Figures

Chapter 1

Introduction

1.1 Cosmic-rays, Gamma-rays and Neutrinos

1.1.1 Cosmic-rays

Cosmic-rays (CRs) are relativistic particles arriving on earth from all directions. Specially, the most energetic ones, the ultra-high-energy cosmic rays (UHECRs) have energy $E > 10^{18}$ eV which is $\sim 10^6$ times greater the energy of the particles produced in the most powerful accelerator the large hadron collider (LHC) on earth (Zatsepin and Kuz'min, 1966; Aab et al., 2017; Das et al., 2021). There are many experiments, like e.g. Volcano Ranch array in New Mexico (Linsley and Scarsi, 1962; Abbasi et al., 2005; Norman et al., 1995), and more recently, Pierre Auger Observatory (Auger-Collaboration, 2015) which observed CRs in a very wide energy range $E = (10^9 - 10^{21})$ eV. Linsley and Scarsi (1962) discovered the first CR with an energy of about $E \simeq 10^{20}$ eV in the Volcano Ranch array, USA. In 1991, Fly's Eye (Abbasi et al., 2005) detected CRs with energy 3×10^{20} eV and in 1994, AGASA (Yoshida et al., 1994) detect CR with energy 2×10^{20} eV.

In Fig. 1.1, we show the all particle CR spectrum from different air shower experiments. In general, the flux of low energy CRs ($E < 10^{15}$ eV) and intermediate energy CRs ($10^{15} \leq E/\text{eV} < 10^{18}$) are comparatively higher than that of UHECRs $E > 10^{18}$ eV flux as shown in Fig. 1.1. There are many features in the spectrum of CRs measured by the Pierre Auger Observatory. These features (the change in the slop of the spectrum) may be an indication of change in the CR composition at different energies as well as the change in the potential sources (Schröder, 2019).

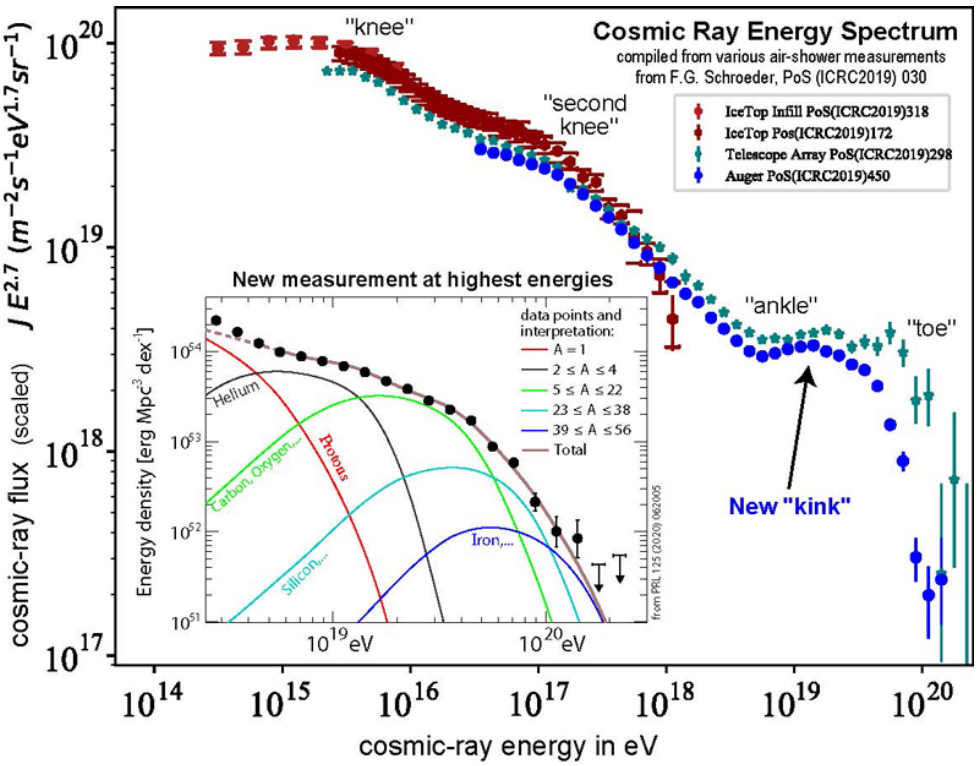

Figure 1.1: All particle CR spectrum from different air shower experiments. There are many features that can be seen such as the "knee," ($\sim 5\times10^{15}$ eV) the "second knee" ($\sim 5\times10^{17}$ eV) the "ankle" ($\sim 6\times10^{18}$ eV), the "new kink" ($\sim 10^{19}$ eV), and the "toe" ($\sim 10^{20}$ eV). The new measurement details is shown by the inset figure. This figure is taken from Schröder (2019).

1.1.2 CR composition

Generally, CRs are a mixture of charged particles of different compositions that are produced at the acceleration sites in astrophysical sources. Also the interactions of primary CRs during their propagation medium lead to the production of secondary particles, enriching the composition, for instance, in light elements (e.g., p, He, Li) and electrons. The composition of CRs in terms of nuclear species is largely uncertain above PeV energy (Tjus and Merten, 2020; Aab et al., 2015; Sokolsky and Thomson, 2020). For lower energy CRs (of galactic origin) the chemical composition is better defined. At energies around few GeV, proton is the most abundant element in the CR composition (see Tjus and Merten, 2020, and reference therein) and at TeV energy the most abundant species are proton and helium Ahn et al. (2009); Yoon et al. (2011). Around PeV energy the KASCADE data Apel et al. (2014); Arteaga-Velázquez et al. (2015, 2017) reported that the CR composition is dominated by heavy nuclei than the light elements. In the supernova paradigm (where the CRs can be accelerated up to energy 10^{17} eV), the chemical composition is dominated

by the iron nuclei (Apel et al., 2011; Sveshnikova et al., 2013; Aloisio et al., 2014). In the energy range $(10^{17} - 10^{18})$ eV, the light composition is dominant as observed by Pierre Auger Observatory (Aab et al., 2014) and indirectly by LOFAR (Buitink et al., 2016). Generally, below energy 10^{18} eV, the CRs flux composition consists mainly of protons and helium, with little percentage of iron nuclei as well, predicted by different air-shower experiments (Abbasi et al., 2010; Apel et al., 2013; Aab et al., 2014; Unger et al., 2015; Thoudam et al., 2016; Buitink et al., 2016; Dembinski, 2019; Tjus and Merten, 2020).

For UHECRs ($> 10^{18}$ eV), there are observations suggestive of the dominance of heavier nuclei (Aab et al., 2016, 2017, 2018). The HiRes data (Sokolsky and Thomson, 2007; Aloisio et al., 2011; Tjus and Merten, 2020) suggested a proton distribution mostly, but the Auger data indicates substantial composition of heavier nuclei (Aab et al., 2016, 2017, 2020; Sokolsky and Thomson, 2020).

1.1.3 Sources of CRs

Observational evidences endorse the view that CRs with energy lower than $E \lesssim 10^{18}$ eV come mostly from the Milky-Way and the local group of galaxies (Tjus and Merten, 2020). The sudden steepening of the CR energy spectrum (the knee, see Fig. 1.1) is observed at an energy of about $\sim 10^{16}$ eV and the second knee occurs at $\sim 5 \times 10^{17}$ eV. CRs acceleration up to the first 'knee' has long been associated with supernovae remnant (SNR). This standard model of galactic CRs origin is discussed in detail in several works (e.g., Baade and Zwicky, 1934; Aharonian, 2004; Blandford et al., 2014; Tibolla and Drury, 2014; Katou and Amano, 2019). A theory which proposes a natural way to accelerate the CRs in the shock fronts of SNR shells is diffusive shock acceleration (DSA) in which the first order Fermi process operates (e.g., Tibolla and Drury, 2014; Katou and Amano, 2019, for review). This acceleration picture of galactic CRs was further strengthened by the detection of TeV gamma rays emission from SNRs by Imaging Atmospheric Cherenkov Telescopes (IACTs) (Aharonian et al., 2006; Inoue et al., 2005; Murase et al., 2015; Cerruti et al., 2017; Paliya et al., 2015). Further support also comes from Fermi-LAT and Chandra satellites at lower energies when they observed the prominent SNR Tycho (Slane et al., 2014; Caprioli and Spitkovsky, 2014) indicating that the particle acceleration is linked mostly with protons on account of $\sim (10 - 20)\%$ of the explosion energy.

The origin of UHECRs is even less understood. Many evidences endorse the extra-

galactic origin of CRs with energies around 10^{18} eV or higher, but it is still not clear at which energy there is a transition between galactic and extragalactic CRs (see e.g., Aloisio et al., 2012; Parizot, 2014; Giacinti et al., 2015; Thoudam et al., 2016; Kachelriess, 2019; Alves Batista et al., 2017; Castelvecchi, 2017; Alves Batista et al., 2019; Aab et al., 2020). Berezinsky (2006); Globus et al. (2015); Giacinti et al. (2015); Beresnyak (2017) discussed different models of transition from galactic to extragalactic CRs with different composition of injected particles. They found that the transition energy is different for different composition (with changing mass composition from galactic iron to extragalactic mixed composition of different nuclei) and for different models of CRs propagation.

Greisen (1966) and Zatsepin and Kuz'min (1966) first pointed out that UHECRs would interact with the microwave background radiation and loose up to 20% of their energy. These losses constrain the distance of the sources which produce the observed UHECRs, to the local Universe (within $\sim$ 100 Mpc) (e.g., Medina Tanco et al., 1997; de Gouveia Dal Pino and Lazarian, 2000; Ahlers et al., 2018; Anchordoqui and Soriano, 2019; di Matteo et al., 2021). Recently, in Aab et al. (2018) they found evidence of increasing contribution from nearby sources due to the increased attenuation suffered by the CR from distant sources. Several types of astrophysical sources have been predicted as the sources of high-energy CRs such as active galactic nuclei (AGNs), star-forming galaxies (SFGs), starburst galaxies (SBGs), gamma-ray bursts (GRBs), and clusters of galaxies (e.g., Kotera et al., 2009; Aab et al., 2016, 2018, 2020; Waxman, 2017; Zhang et al., 2018; Sokolsky and Thomson, 2020). Pierre Auger observations associate the origin of UHECRs with nearby active galaxies (e.g., Auger-Collaboration, 2015) and SFGs (e.g., Liu et al., 2014; Anchordoqui and Soriano, 2019; Alves Batista et al., 2019). Radio galaxies and blazars are in particular (see e.g., Tjus and Merten, 2020, and reference therein), the most powerful candidates which seem to be able to accelerate CRs to ultra-high-energies either in the nuclear region or along the jet, both by shock acceleration or by magnetic reconnection (e.g., Ptitsyna and Troitsky, 2010; Kadowaki et al., 2015; Rodríguez-Ramírez et al., 2019; Alves Batista et al., 2019; Anchordoqui and Soriano, 2019; Aab et al., 2020; Medina-Torrejon et al., 2021). The acceleration of heavy nuclei (e.g. N, Fe, etc) is possible in more abundant lower power Seyfert galaxies (e.g., Anjos and Coimbra-Araújo, 2017; Mbarek and Caprioli, 2019) and also by tidal disruption events by the supermassive and intermediate mass black holes (Farrar and Gruzinov, 2009; Alves Batista and Silk, 2017).

There are many other restrictions posed by radiative losses and interactions of CRs with the background environment on the CR acceleration models and sources (Aharonian et al., 2002; Protheroe, 2004; Aloisio et al., 2014; Feng et al., 2016). The interactions of the CRs as well as their radiative losses depend on the configuration of the background density, photon and magnetic fields, as well as of the energy of the CRs. A comprehensive review on extragalactic magnetic fields distribution is presented in Alves Batista et al. (2017); Vazza et al. (2017); Hackstein et al. (2018), reporting a large uncertainty and many differences across models.

The interaction of CRs with magnetic fields is of primary importance for the acceleration, evolution and dynamics of these particles (Blasi et al., 2007; Bonafede et al., 2012). CRs can be trapped and accelerated via the scattering with magnetic field fluctuations in shocks and/or turbulent driven outflows (Brunetti and Lazarian, 2007; Brunetti et al., 2009; Blasi, 2013; Vazza et al., 2017; Brunetti and Vazza, 2020). Most probably, the AGN jets and the accretion disks are the most prominent sites to accelerate CRs to very high energy by first order Fermi-acceleration due to the presence of highly turbulent magnetic field in these environments (e.g., Winchen and Buitink, 2018; Tibolla and Blandford, 2018; Katou and Amano, 2019). The outskirts of AGNs and galaxy clusters might be most promising sites for second order Fermi-acceleration. Other potential sources of high-energy CRs are starburst galaxies (e.g., Anchordoqui, 2018; Peretti et al., 2019, 2020, 2021; Ambrosone et al., 2021; Kornecki et al., 2022) due to high gas density and the presence of supernova explosions associated to high star-formation rate. Starburst galaxies in special can accelerate heavy nuclei because photo-disintegration can be avoided in these sources if particles escape from the nuclear region and are reaccelerated by the shocks in the starburst wind. Due to the complexity of the astrophysical environments the different acceleration mechanisms mentioned above are still under debate.

There are many studies which describe clusters of galaxies (e.g., the nearby Virgo cluster) as potential sources of UHECRs (e.g., Murase et al., 2008; Dolag et al., 2009; Murase and Beacom, 2013; Fang and Olinto, 2016; Fang and Murase, 2018). The Radio galaxy Virgo-A (M87) in the center of Virgo cluster can be the most appropriate source of UHECRs (e.g., Medina-Tanco and Enßlin, 2001; Kobzar et al., 2019). Galaxy Clusters host several potential accelerators of CRs, from ordinary to active galaxies (Völk et al., 1996; Liu et al., 2014), shock waves driven in the ICM during the phenomenon of cluster

formation (Zhang et al., 2021) and cluster merging (see Brunetti and Jones, 2014, for a review). The lifetime of CRs against energy losses in the ICM is long and their likely slow diffusive propagation through the ICM magnetic field, together with the large size of the galaxy clusters, make them prominent hosts of CRs produced within their volume (Vazza et al., 2016).

1.1.4 Diffuse neutrino and gamma-rays background

Neutrinos are produced whenever CR ions interact with matter or photons near their accelerations sites. They are ideal messengers to carry out information about the environment of astrophysical sources where they are produced because magnetic field and intervening matter cannot deflect them. The IceCube neutrino observatory reported evidence of an isotropic distribution of high-energy neutrinos with $\sim$ PeV energies (Aartsen et al., 2017, 2020). Their origin is not known yet, but the isotropy of the distribution suggests that they are predominantly of extragalactic origin. They might come from various types of sources, such as starbursts galaxies, galaxy mergers, AGNs (Murase et al., 2013; Kashiyama and Mészáros, 2014; Anchordoqui et al., 2014; Fang and Murase, 2018), SNR (Chakraborty and Izaguirre, 2015; Senno et al., 2015), gamma-ray bursts (Hümmer et al., 2012; Liu and Wang, 2013) and cluster of galaxies (Murase et al., 2008; Blasi, 2013; Murase and Beacom, 2013; Fang and Olinto, 2016; Fang and Murase, 2018; Hussain et al., 2019). Since neutrinos can reach the Earth without being deflected by magnetic fields or attenuated due to any sort of interaction, they can help to unveil the sources of UHECRs that produce them. In this context, the most probable high-energy neutrino source detected by IceCube is TXS $0506+056$ (IceCube-Collaboration et al., 2018).

Another by product of high-energy and UHECRs is gamma-ray radiation. This is also produced when CRs interact with gas and photon fields in the astrophysical environments. In particular, the diffuse gamma-ray background (DGRB) is the measured radiation that remains after subtracting all known sources from the observed gamma-ray sky. The DGRB gives a non-thermal perspective of the Universe, at high-energy ($10^{15} \leq E/\mathrm{eV} \leq 10^{18}$). The DGRB was measured by EGRET (e.g., Sreekumar et al., 1998; Strong et al., 2004) and the Fermi-LAT (e.g., Ackermann et al., 2012, 2015; Fermi-LAT et al., 2015; Ackermann et al., 2019). It is most probably due to the summed contributions of different unresolved sources, such SFGs, (e.g., Tamborra et al., 2014; Roth et al., 2021), pulsars, AGNs,

(e.g., Di Mauro et al., 2013; Ajello et al., 2015), GRB (e. g., Stecker and Venters, 2011; Ackermann et al., 2012; Fornasa et al., 2013; Di Mauro and Donato, 2015; Albert et al., 2021) and cluster of galaxies (e.g., Zandanel et al., 2015; Alves Batista et al., 2019), or in other words, the same class of sources that are believed to produce high-energy CRs and neutrinos. Recent studies indicate that individual class of sources such as SFGs and AGNs can contribute to a fairly large fraction to the DGRB for energies below TeV (e.g., Fornasa and Sanchez-Conde, 2015; Ackermann et al., 2015; Roth et al., 2021), but the uncertainties towards larger energies remain.

The origin of UHECRs, high-energy neutrinos and the diffuse gamma-ray emission are among the major mysteries in astroparticle physics. The fact that the observed energy fluxes of HECRs and UHECRs, high-energy neutrinos, and diffuse gamma rays are all comparable suggests that these messengers may have some connection with each other (Ahlers and Halzen, 2018; Alves Batista et al., 2019; Ackermann et al., 2019). The flux of these high-energy multi-messengers is shown in Fig. 1.2. The three fluxes could, in principle, be explained by a single class of sources, like starburst galaxies or active galaxies, or even their summed contribution in clusters of galaxies (e.g., Fang and Murase, 2018; Ahlers and Halzen, 2018), but this is not clear yet. The study of these high-energy connected phenomena in the framework of the largest scale structures of the Universe, namely, the clusters of galaxies, may help to elucidate their origin. This is the main goal of this Thesis (see more in Section 1.3 below).

1.2 Clusters of galaxies and production of high-energy multi-messengers

Clusters of galaxies are the largest gravitational bound structures that exist in the Universe. They are believed to be the result of very violent processes such as accretion and merging of smaller structures into larger ones. These processes can release large amounts of energy ($\sim 10^{60} - 10^{64}$ erg), part of which can accelerate CRs to very-high energies (Voit, 2005; Brunetti and Jones, 2014; Bonafede et al., 2021; Nishiwaki et al., 2021). The formation and evolution of clusters depends on both baryonic and dark matter. In fact, clusters of galaxies (e.g., Bullet cluster) are the most prominent sources of dark matter in the Universe (Robertson et al., 2016). Their typical size is of the order of $\sim$ Mpc and magnetic field strength is $\sim (10^{-8} - 10^{-5})$ G. Galaxy clusters emit X-rays radiation

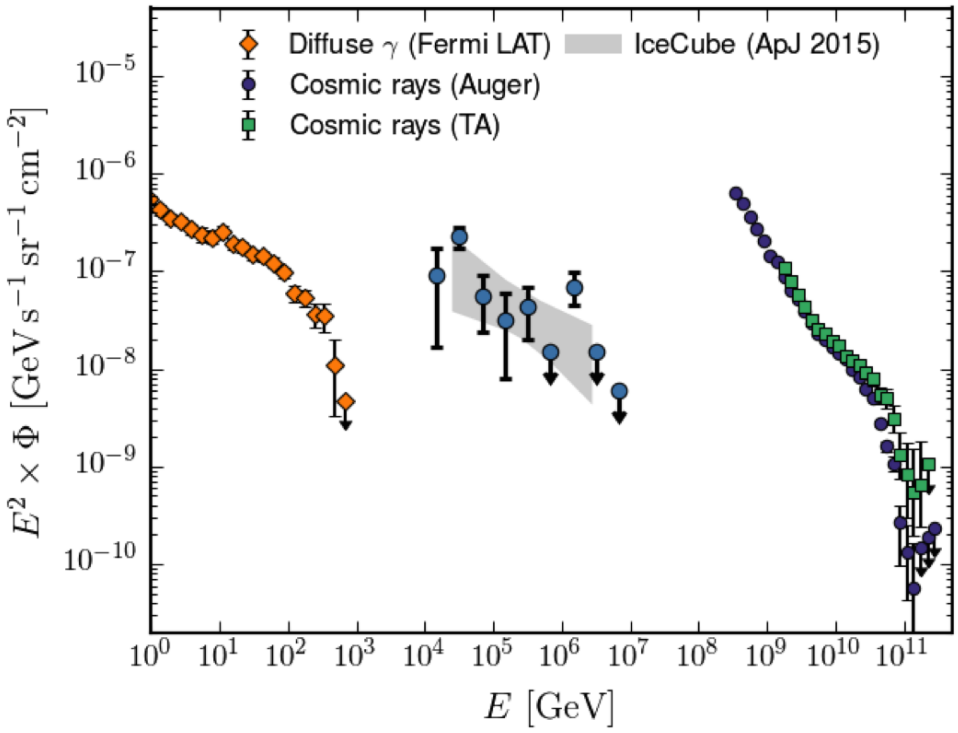

Figure 1.2: Flux of high-energy multi-messengers: CRs, neutrinos and gamma-rays from different experiments (Gaisser 2017). It can be seen that these three fluxes are all comparable.

produced by thermal Bremsstrahlung in the hot ($\sim 10^7 - 10^8$ K) gas bound by their potential well (e.g., Montes and Trujillo, 2019).

CRs are accelerated by shock waves and turbulence through the intracluster medium (ICM). These can be also re-accelerated by similar processes in more diffuse regions of the ICM, including relics, halos, filaments, and cluster mergers (e.g., Brunetti and Jones, 2014; Brunetti and Vazza, 2020; Bonafede et al., 2021; Nishiwaki et al., 2021, for reviews). Furthermore, clusters of galaxies are attractive candidates for UHECR production due to their extended sizes ($\simeq$ Mpc) and magnetic field strength (e.g., Fang and Murase, 2018; Kim et al., 2019). Clusters also naturally can introduce a spectral softening due to the fast escape of HECRs from the magnetized environment which might explain the second knee that appears around $\sim 10^{17}$ eV, in the CR spectrum (Apel et al., 2013) (Fig. 1.1). As described in Section 1.1, CRs with energies $E > 7 \times 10^{18}$ eV have most likely an extragalactic origin (e.g., Aab et al., 2018; Alves Batista et al., 2019), and those with $E \lesssim 10^{17}$ eV are believed to have Galactic origin (see e.g., Blasi, 2013; Amato and Blasi, 2018). CRs with $E \lesssim 10^{17}$ eV can be confined within clusters for a time comparable to the age of the Universe due to the large size of these structures ($\sim$ Mpc)

and their magnetic-field strength up to $B \sim \mu$G (Dolag et al., 2005; Brunetti and Jones, 2014). Therefore, clusters are important reservoirs of CRs that can produce high-energy photons and neutrinos through collisions with the gas in intracluster medium (ICM), or through processes involving energetic electron−positron pairs produced as secondaries of hadronic and/or leptonic interactions. (e.g., Berezinsky et al., 1997; Rordorf et al., 2004; Kotera et al., 2009; Fang and Olinto, 2016; Fang and Murase, 2018; Brunetti and Vazza, 2020; Nishiwaki et al., 2021). Electron-positron pairs produce Synchrotron and Inverse Compton (IC) emission in radio to gamma-ray wavelengths (Jeltema and Profumo, 2011; Gu et al., 2019; Yuan et al., 2019; Sobacchi and Lyubarsky, 2020) and thus, non-thermal radio to gamma-ray and neutrino observations can constrain the properties of CRs in clusters (Berezinsky et al., 1997; Wolfe and Melia, 2008; Yoast-Hull et al., 2013; Zandanel et al., 2015). Conversely, the diffuse flux of gamma rays and neutrinos depend on the energy budget of CR protons in the ICM. Moreover, it seems that the turbulence in the ICM alone cannot reaccelerate electrons to TeV energies (Brunetti et al., 2017). Thus, the HE gamma-ray emission in the ICM can in principle be only powered by the process of continuous injection of secondary particles coming from CR hadronic interactions (pion-decay and IC from TeV secondary electrons). Also, the CR interactions with the cosmic microwave background (CMB) and the extragalactic background light (EBL) [1] are promising channels to produce HE gamma-rays especially for CRs with energies $\gtrsim 10^{18}$ eV (e.g., Blasi et al., 2007; Murase and Beacom, 2013; Prokhorov and Churazov, 2014; Brunetti and Jones, 2014; Murase and Waxman, 2016; Brunetti et al., 2017; Nishiwaki et al., 2021).

To calculate the fluxes of CRs and secondary particles from clusters, there has been many analytical and semi-analytical works (Berezinsky et al., 1997; Wolfe and Melia, 2008; Murase et al., 2013; Fang and Olinto, 2016; Fang and Murase, 2018; Hussain et al., 2019; Brunetti and Vazza, 2020; Nishiwaki et al., 2021), but in most of the approaches, the ICM model is overly simplified by assuming, for instance, uniform magnetic field and gas distribution. There has been more realistic numerical approaches in Rordorf et al. (2004) and Kotera et al. (2009) who explored the three-dimensional (3D) magnetic field effects in clusters. They predicated that the diffusive neutrino flux around PeV energy produced

[1] The EBL corresponds to the sum of the starlight emitted by the first stars formed before galaxies and by galaxies through the history of the Universe (Stecker et al., 2006, 2016; Aharonian et al., 2006; Finke et al., 2010; Dominguez et al., 2011; Gilmore et al., 2012).

in clusters of galaxies via hadronic interactions may have a chance to be detected by the IceCub, but the observation of gamma-rays produced in this process will be even more difficult.

In the case of neutrinos, more recenlty, Fang and Olinto (2016) and Fang and Murase (2018) estimated the flux from clusters assuming an one-dimensional model for the background fields, isothermal gas distribution, a radial profile for the total matter (baryonic and dark) density, and a turbulent magnetic field with coherence length ~ 100 kpc. They obtained a flux which is comparable to IceCube measurements.

Likewise, in the case of the gamma-ray emission, several studies have estimated the diffuse gamma-ray (DGRB) flux from clusters of galaxies (e.g., Kotera et al., 2009; Zandanel et al., 2015; Fang and Murase, 2018; Nishiwaki et al., 2021) also considering an oversimplified ICM. Besides, these studies have not accounted for the contributions from less massive clusters $< 10^{14}\ M_{\odot}$. These studies concluded that the clusters of galaxies cannot contribute significantly to the DGRB. In Murase et al. (2013), they estimated the gamma-ray flux from clusters using a purely hadronuclear scenario (pp-interaction) claiming that these sources would contribute to a large fraction to the DGRB.

In this Thesis, we revisit and extend these previous analyses of the production of diffuse gamma-rays and neutrinos by clusters of galxies, employing a more rigorous numerical approach. We take into account the non-uniformity of the gas density and magnetic field distributions in clusters as well as their time evolution, as obtained from 3D-MHD cosmological simulations. Numerical three-dimensional (3D) MHD simulations of self gravitating fluids have become routinely used to study the non-linear clustering of dark matter, the formation of galaxy clusters, the merging of galaxies, and the evolution of the intergalactic gas (e.g., Dolag et al., 1999, 2002, 2005; Vazza et al., 2017; Barai and de Gouveia Dal Pino, 2019; Hopkins et al., 2020, 2021). We inject CRs into this cosmological environment and follow their propagation and cascading due to interactions with this background which leads to the production of neutrinos and gamma-rays. We consider different locations of CR sources within the clusters, and the mass dependence of the physical properties of the clusters. This last consideration is important because massive clusters ($\gtrsim 10^{15}\ M_{\odot}$) are much less common than lower-mass ones ($\lesssim 10^{13}\ M_{\odot}$), (Rosati et al., 2002; Jenkins et al., 2001). Consequently, more massive clusters, which can confine CRs of energy above PeV for longer time, are probably more relevant for production of high-energy neutrinos.

We also investigate the propagation effects outside the clusters, in order to compute the fluxes of diffuse gamma-rays and neutrinos up to the Earth. To this end, we follow the propagation and cascading of CRs and their by-products in cosmological background simulations as performed by Dolag et al. (2005) and use a Monte Carlo code, CRPropa 3 (Alves Batista et al., 2016), that accounts for all relevant photohadronic, photonuclear, interaction processes in the turbulent ICM and IGM.

Below in Fig. 1.3, we present a schematic diagram that illustrates the potential production of gamma-rays and neutrinos by a cluster of galaxies.

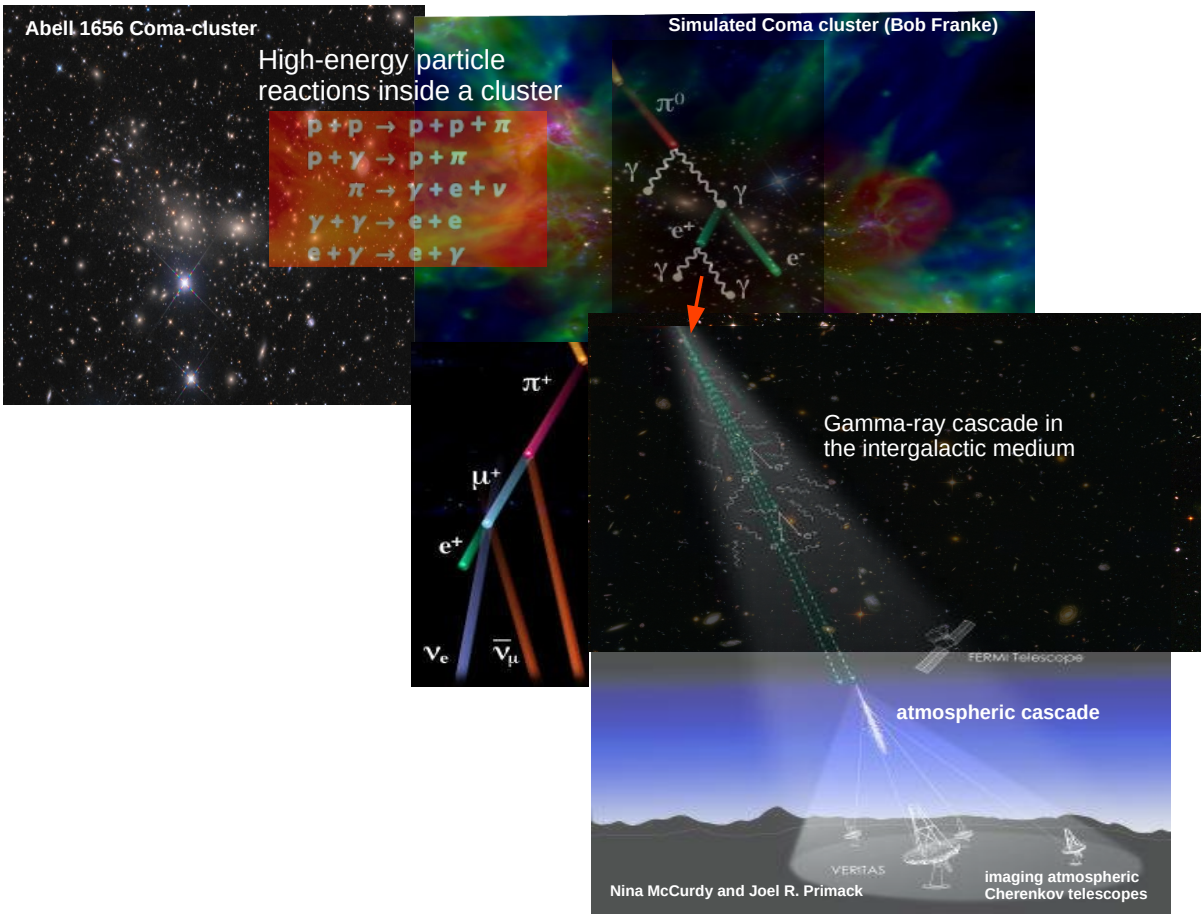

Figure 1.3: Schematic diagram illustrating CR, neutrinos, and gamma-rays potential production and observations. Neutrinos can be detected by the IceCube and the gamma-rays can be observed by Cherenkov radiation detectors and telescopes such as VERITAS, HAWC, LHAASO, and CTA.

1.3 Objectives and Plan of this Thesis

The detailed goals of this Thesis are the following:

- derive the properties and evolution of clusters of galaxies and the ICM and IGM by means of 3D MHD cosmological simulations at different redshifts from $z = 5$ to $z = 0$. For that, we will use the simulations performed by Dolag et al. (2005).

- To derive the CR interactions that are important in the magnetized turbulent environment of the ICM and IGM to produce secondary particles, like electron-positron pairs, gamma-rays and neutrinos.

- To inject test particles (CRs), employing the CRPropa 3 code (Alves Batista et al., 2016), in the turbulent environments built out of the MHD simulations and follow their trajectories and deflections in the background magnetic field, as well as to evaluate their energy losses due to interactions with the background radiation and density fields.

- Finally, to derive the resulting CR spectrum after propagation and re-acceleration in the ICM and IGM, and compute the flux of neutrinos and gamma-rays, comparing our results with the observed spectrum of IceCube and Fermi-LAT, respectively, as well as, with forthcoming observatories like the CTA and LAAHSO, providing new constraints for the clusters emission.

The plan of the next Chapters is as follows: in Chapter 2, we will describe the 3D-MHD simulations of the galaxy clusters and IGM as well as the properties of the clusters derived from the simulations. In Chapter 3, we derive the interaction rates and mean free path of all relevant CR interactions in the ICM and IGM. We also discuss the CR propagation in individual clusters. The main results of this thesis are presented in Chapters 4 and 5. In Chapter 4, we compute the contribution of the clusters to the diffuse neutrinos background and in Chapter 5, we derive the diffuse gamma-ray emission. Finally, in Chapter 6 we present our conclusions and future perspectives.

Chapter 2

Three Dimensional MagnetoHydroDynamical Cosmological Simulations of Clusters of Galaxies

Magnetohydrodynamics (MHD) is an adequate theoretical framework to probe a wide variety of astrophysical environments as predicted by many studies (e.g., Hawley et al., 1995; Giacomazzo et al., 2006; Priest, 2012, and reference therein). This Chapter is dedicated to describe the MHD background cosmological simulations which we used to describe the evolution of the large scale structures of the universe. It is organised as follows: In Section 2.1, we discuss the setup of these simulations (Dolag et al., 2005). In Section 2.2, we present the properties of the clusters of galaxies, obtained from the simulations for different redshifts, namely, the magnetic field, density, temperature, gas mass, and dark matter distributions. In Section 2.3, we discuss the compatibility of the results of our MHD simulations with the observations.

2.1 Setup conditions of the 3D-MHD Cosmological Numerical Simulations

We are interested in studying the propagation of CRs in the ICM and IGM over cosmological times. In order to describe appropriately the background multidimensional properties and evolution of the large scales structures, we employ the 3D MHD cosmological simulations performed by Dolag et al. (2005) with the GADGET (GAlaxies with Dark matter and Gas intEracT) code (Springel et al., 2001; Springel, 2005). GADGET is a Lagrangian code that employs smoothed particle hydrodynamics (SPH) to integrate numerically the MHD equations. Appendix A provides a brief technical description of this code (see also Springel et al., 2001; Springel, 2005).

The MHD simulations presented here are performed by GADGET-2 code (Springel, 2005) and the magnetic field in them is treated in the framework of ideal MHD (e.g., Dolag et al., 1999). We provided a brief detail of the ideal MHD equations and the SPH method in the Appendix A (see also Dolag et al., 1999; Springel et al., 2001, for details). In these simulations (Dolag et al., 2005), along with the induction equation for magnetic field they also consider the back-reaction of the field based on Maxwell tensor. As the initial conditions of the simulations Dolag et al. (2005) assumed a homogeneous seed magnetic field exists at high redshift, following Dolag et al. (2002). They performed two simulation for two seed magnetic field (10^{-11} and 2×10^{-12} G) and found a good match with the observations in both cases (Dolag et al., 2002, 2005).

These simulations used similar initial density fluctuations as those of Mathis et al. (2002); Hoffman and Ribak (1991), which were constructed from the IRAS 1.2−Jy galaxy survey. These initial conditions provide a good match to the large-scale structures observed in the local Universe (Mathis et al., 2002). In the simulations, they set the gravitational force resolution is $\sim$ 10 kpc. Radiative cooling was not accounted for either and the magnetic field pressure remains below the thermal pressure. The simulations also neglected the injection or amplification of magnetic fields due to galactic winds or AGNs during the cluster formation. In fact, no AGN or star formation feedback were included in these cosmological simulations. We will include these effects in the calculations of the fluxes of CRs, neutrinos and gamma-rays through the introduction of correction functions (see Chapters 4 and 5). The background cosmological parameters assumed are $h \equiv H_0/(100 \text{ km s}^{-1} \text{ Mpc}^{-1}) = 0.7$, $\Omega_m = 0.3$, $\Omega_\Lambda = 0.7$, and the baryonic fraction $\Omega_b/\Omega_m = 14\%$. An adiabatic equation of state for the gas with adiabatic index $\gamma = 5/3$ was considered. The simulated domain is a 3D box with a volume (240Mpc^3) and covers a redshift range $0 < z \lesssim 5.0$. The boundary conditions of the simulations were periodic.

2.2 *Properties of the Galaxy Cluters derived from the Simulations*

The 3D MHD simulations provide the general properties of the background, including the magnetic field, gas density, and temperature. In this work, we consider seven snapshots of these simulations with redshifts $z = 0.01;\ 0.05;\ 0.2;\ 0.5;\ 0.9;\ 1.5;\ 5.0$, each having the same volume $(240 \text{ Mpc})^3$. Fig. 2.1 shows the density distribution of the entire volume

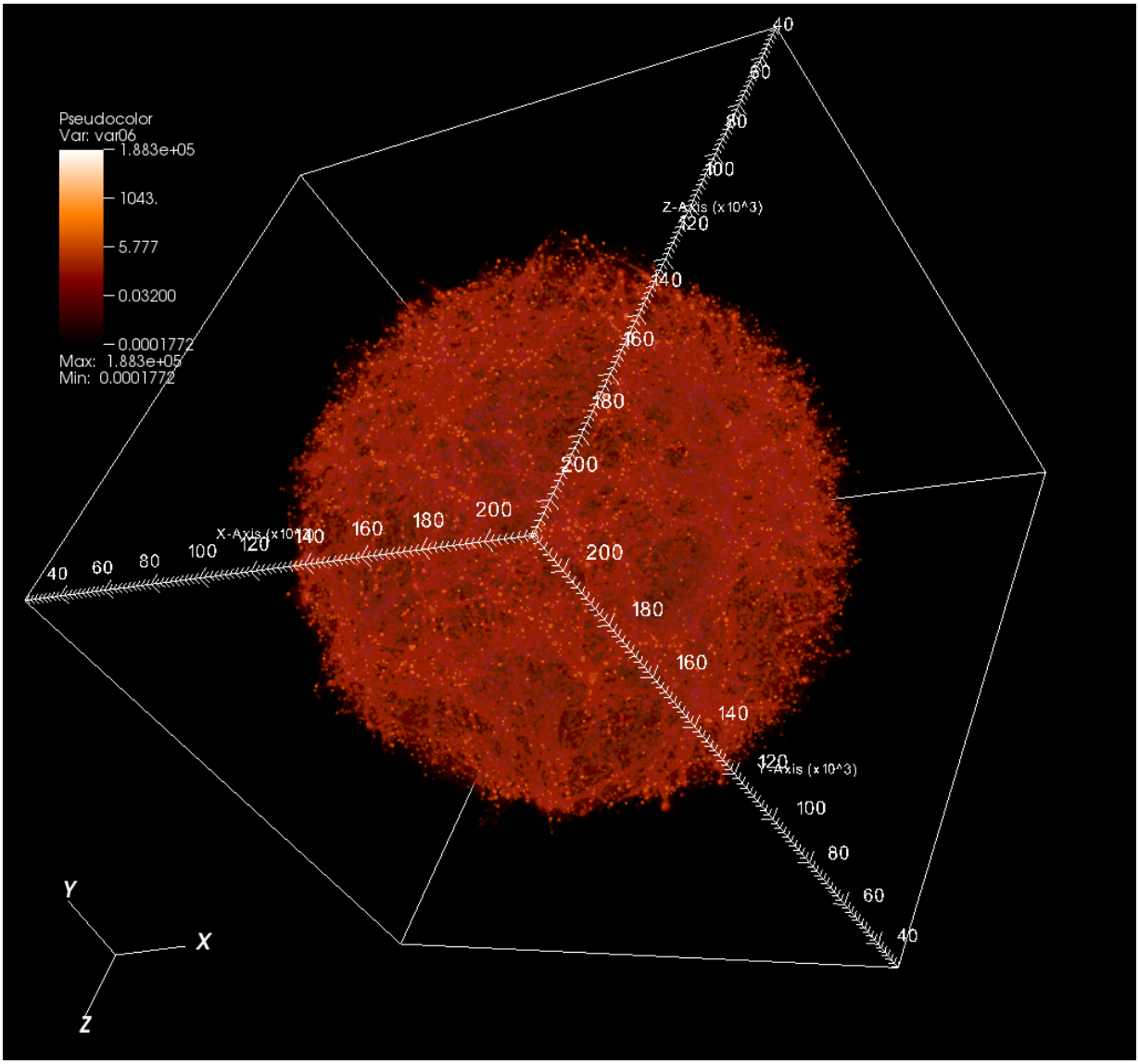

Figure 2.1: Large scale distribution of filaments with clusters of galaxies along them, in a domain of 240 Mpc^3 (see also Dolag et al., 2005).

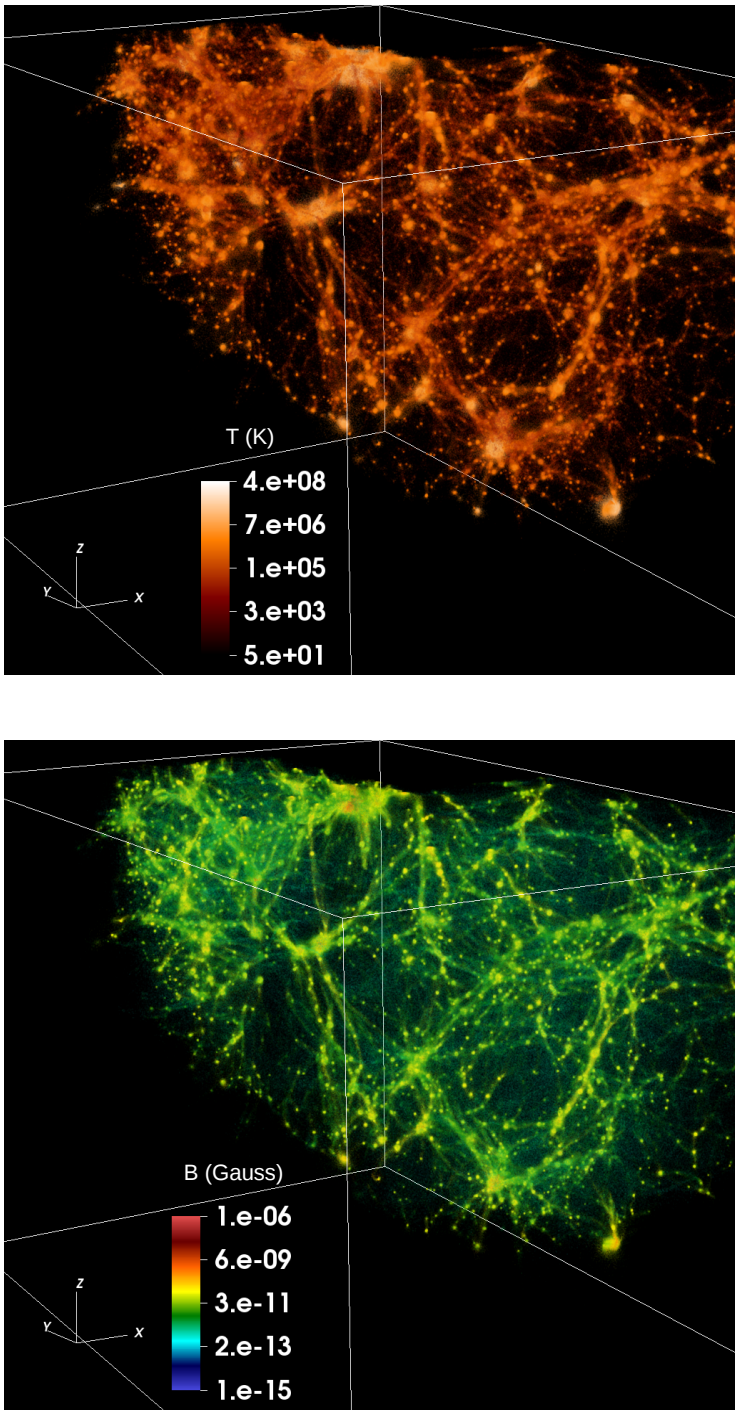

Figure 2.2: This figure shows the temperature (upper panel) and magnetic field (lower panel) for one of the eight regions of our background 3D-MHD cosmological simulation at redshift $z \sim 0$, with dimension 240 Mpc^3 (Hussain et al., 2021).

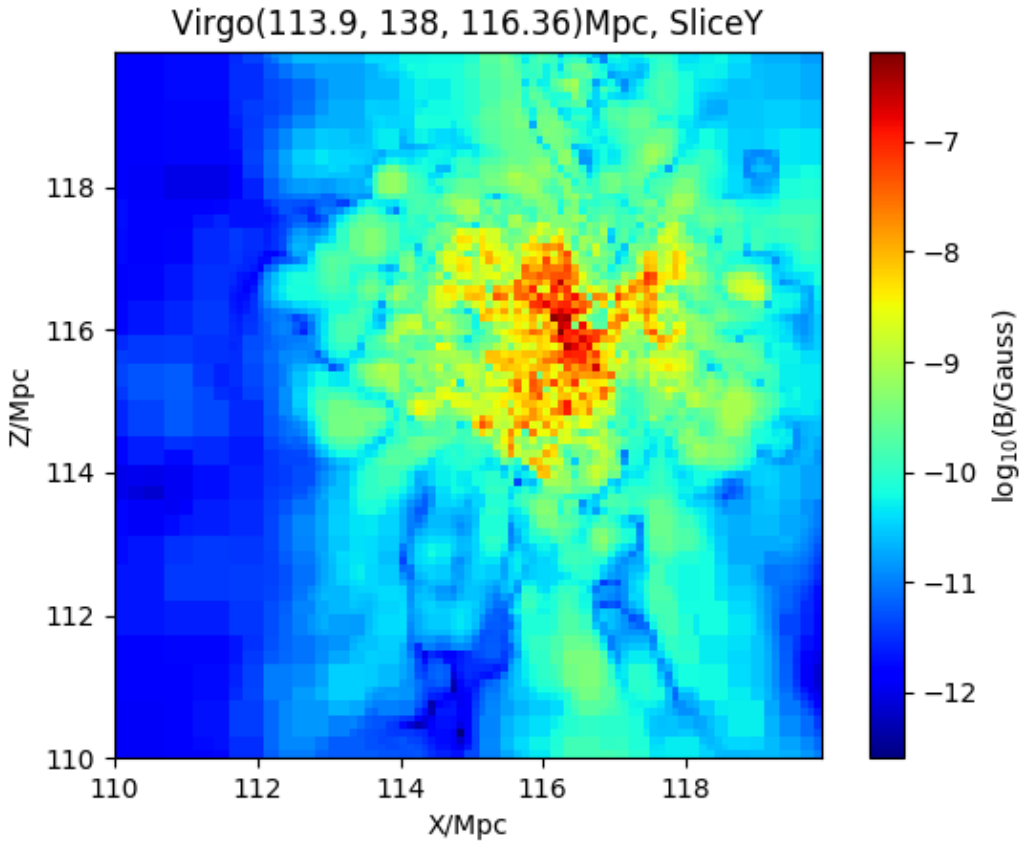

Figure 2.3: This plot is a 2D slice in the $(Z,\ X)$ plan of the magnetic field of the simulated domain corresponding to the region of the Virgo cluster centered at at (113.9, 138, 116.36) Mpc in Fig. 2.1 (see also Dolag et al., 2005).

of the simulation at the local universe, at redshift $z \sim 0$. We have divided the domain of each snapshot into eight regions. Fig. 2.2 shows the temperature and magnetic-field distributions for one of these regions, also at redshift $z \sim 0$. The filaments in Figs. 2.1 and 2.2 are populated with galaxy clusters and have dimensions ~ 50 Mpc^3. The voids have dimensions of the same order, which are compatible with observations (e.g., Govoni et al., 2019; Gouin et al., 2020, for review).

In Fig. 2.3 we show a two dimensional map of the magnetic field distribution for the region of the simulated domain corresponding to Virgo cluster. This was extracted from a region near the center of our simulation at $z \sim 0$ which corresponds to Virgo cluster, in Fig. 2.1. The magnetic field we obtained from this region is quite compatible with observation of Virgo cluster. For more detailed description about the temperature and density see Dolag et al. (2005).

We have identified clusters in the densest regions of the isocontour maps of the whole

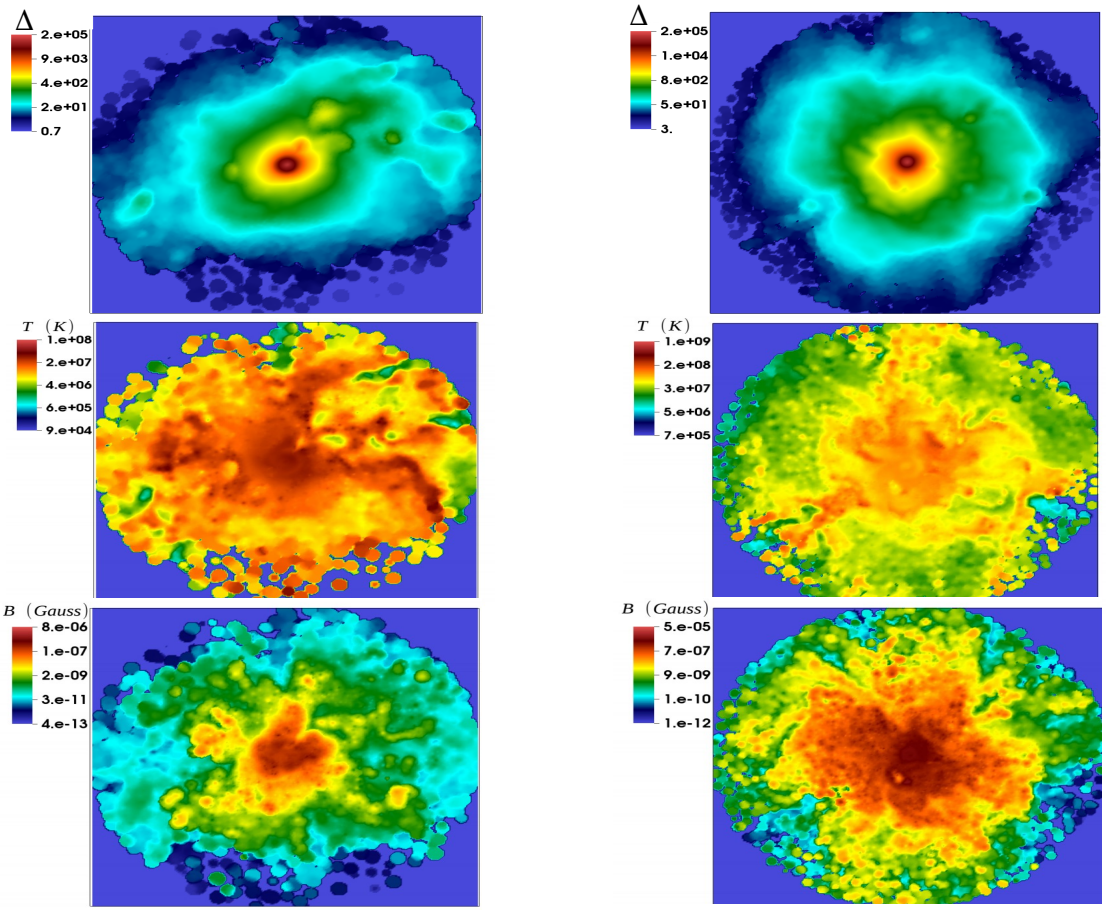

Figure 2.4: Maps of gas density (upper row), temperature (middle row), and magnetic field (bottom row) of two clusters of masses $\sim 10^{14}\ M_{\odot}$ (left panels) and $\sim 10^{15}\ M_{\odot}$ (right panels), at redshift $z \sim 0$ (Hussain et al., 2021).

volume, in each redshift (e.g., Fig. 2.2). We then selected several (around 50) clusters with distinct masses ranging from 10^{12} to $10^{16}\ M_{\odot}$, which we assumed to be representative of all the clusters in each corresponding snapshot (redshift). The mass range we considered is compatible with previous studies and observations as well (see Jenkins et al., 2001; Rosati et al., 2002; Schneider, 2014; Fang and Olinto, 2016; Bocquet et al., 2016). As an example, Fig. 2.4 illustrates relevant properties for two of these clusters with masses $\sim 10^{14}\ M_{\odot}$ (left panel) and $\sim 10^{15}\ M_{\odot}$ (right panel) at redshift $z \sim 0$. To estimate the total mass of a cluster from the simulations, we integrated the baryonic and dark matter densities within a radius of ~ 2 Mpc, assuming an approximate spherical volume. We note that this specific evaluation is not much affected by the deviations from spherical symmetry that we detect in Fig. 2.4.

To illustrate general average properties of the simulated clusters, we converted the Cartesian into spherical coordinates and divided the cluster in 10 concentric spherical shells

of different radii ($R_{\rm shell}$). Starting from the center of the cluster, the shells were first divided in intervals of 100 kpc, then between 300 kpc and 1500 kpc, they were divided in intervals of 200 kpc, and the last shell in the outskirts was taken between 1500 kpc $< r <$ 2000 kpc.

Fig. 2.5 depicts volume-averaged profiles of different quantities as a function of the radial distance for a cluster of mass $\sim 10^{15}\ M_{\odot}$ at four different redshifts. The overdensity in Fig. 2.5 (bottom-right panel) is defined as $\Delta = \rho(r)/\rho_{\rm bary}$, where $\rho(r)$ is the total density at a given position r and $\rho_{\rm bary}$ is the mean baryonic density, $\rho_{\rm bary} = \Omega_{\rm bary} \times \rho_{\rm crit}$, $\rho_{\rm crit} = 3H^2/8\pi{\rm G} \sim 10^{-29}$ gcm^{-3}. The over-density is obviously dimensionless as shown in Fig. 2.4 and 2.5. We see that, in general, these radial profiles are very similar across the cosmological time, except for the temperature that varies non-linearly with time by about four orders of magnitude in the inner regions of the cluster. Fig. 2.5 shows profiles for the temperature, gas density, magnetic field and overdensity for a cluster of mass $\sim 10^{15}\ M_{\odot}$, as a function of the azimuthal (ϕ) angle for different latitudes (θ), within a radial distance of $R = 300$ kpc, at a redshift $z \sim 0$. We see that there are substantial variations in the angular distributions of all the quantities. These variations characterize a deviation from spherical symmetry that may affect the emission pattern of the CRs and consequently secondary gamma rays and neutrinos (see Chapter 4 and 5).

We also find that the magnetic field strength of a cluster depends on its mass: the heavier the cluster, the stronger the average magnetic field is, due to the larger extension of denser regions (see middle column of Fig. 2.4 and Fig. 2.6). Inside all clusters, magnetic fields vary in the range $10^{-12} < B/{\rm G} < 10^{-5}$ and have volume-averages between 10^{-8} G and 10^{-6} G (see also Dolag et al., 2005; Ferrari et al., 2008; Xu et al., 2009; Brunetti and Jones, 2014; Brunetti et al., 2017; Brunetti and Vazza, 2020).

We can compare our background simulation with the so called β model (Schneider, 2014) for the density profile of galaxy clusters which is defined as:

$$n_{\rm ICM}(r) = n_{\rm ICM,0}\left[1 + \left(\frac{r}{r_c}\right)^2\right]^{-3\beta/2} \tag{2.1}$$

Where $\beta = 0.8$, $r_c = 0.1\ r_{\rm vir}$ is the core radius of the cluster (where the $r_{\rm vir}$ is defined as the radius within which the average density of the structure is ~ 200 times the background density). The β-model is based on the assumption of isothermal distribution of the total (dark and luminous) matter, and the temperature of the gas does not depend on the radius.

In the upper panel of Fig. 2.7, we compare the radial density profile of our simulated

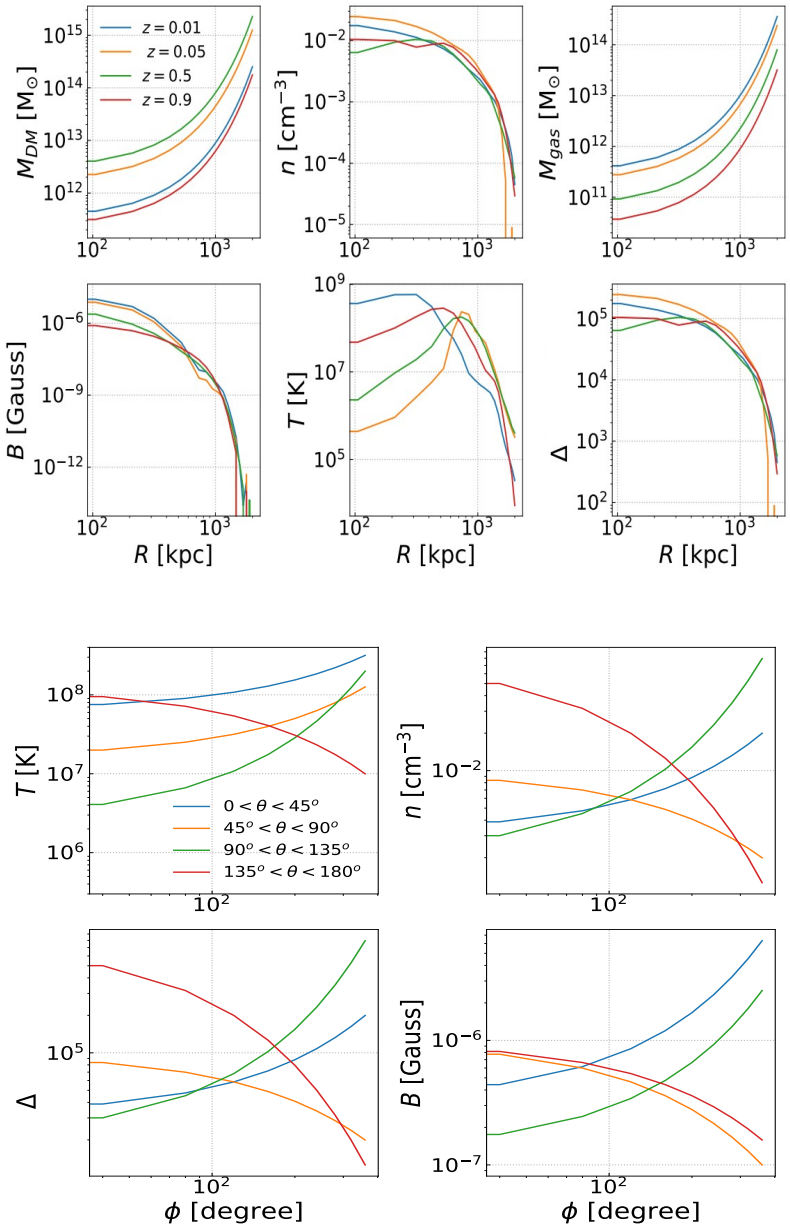

Figure 2.5: Upper panel: Volume-averaged profiles as a function of the radial distance from the center for a cluster of mass $M \sim 10^{15}\ M_\odot$, at four different redshifts. The quantities shown are: dark-matter mass (top left); gas number density (top center); gas mass (top right); magnetic field (bottom left); temperature (bottom-center) and overdensity (bottom right). Lower panel: Volume-averaged profiles as a function of the azimuthal (ϕ) angle for different latitudes (θ), within a radial distance $R = 300$ kpc from the center, for a cluster of mass $M \sim 10^{15}\ M_\odot$. From top left to bottom right clockwise, temperature, gas number density, overdensity, and magnetic field (Hussain et al., 2021).

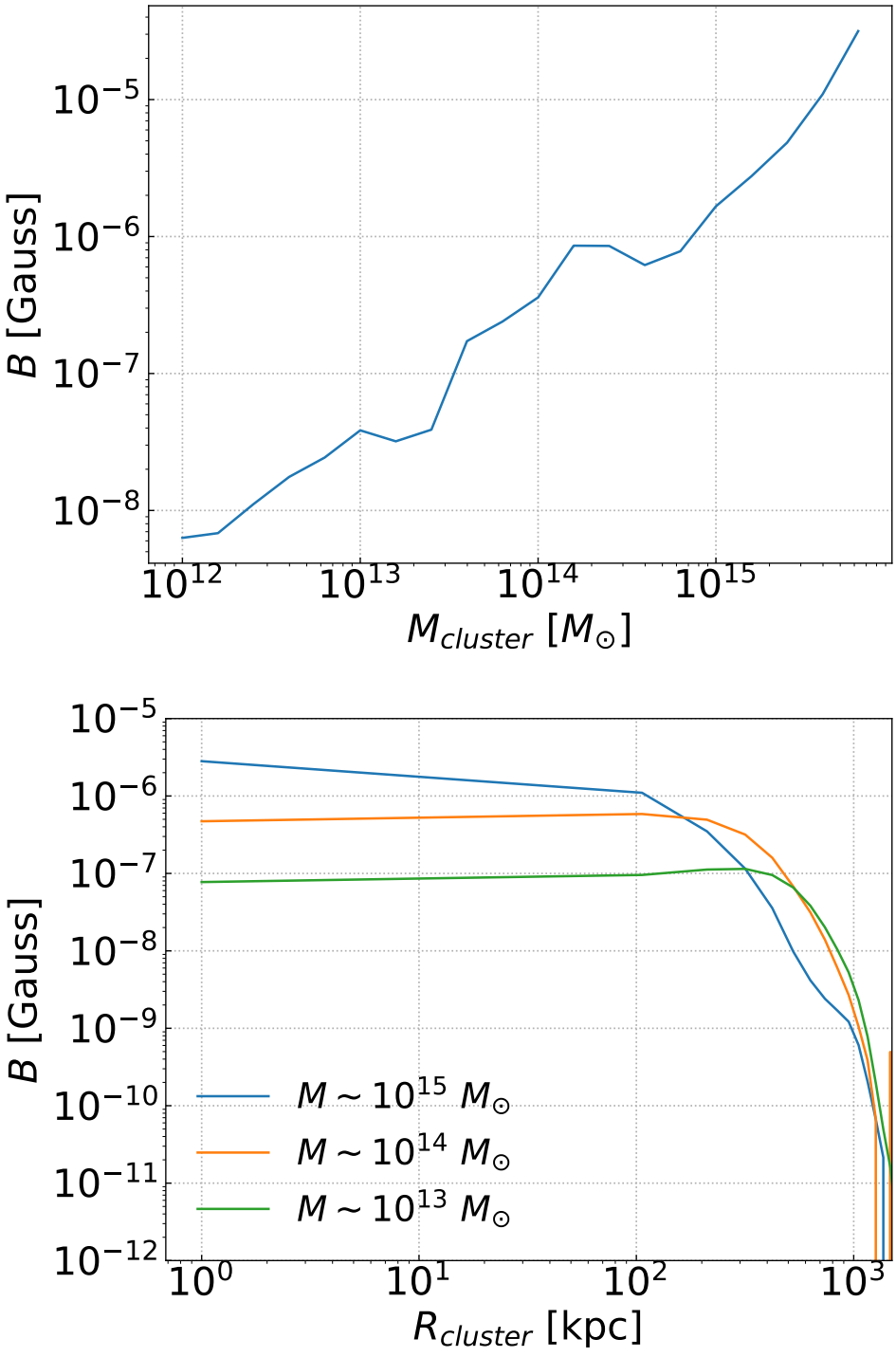

Figure 2.6: Upper panel shows the whole volume-averaged value of the magnetic field as a function of the cluster mass. Lower panel compares the volume-averaged magnetic field as a function of the radial distance for clusters of different masses (Hussain et al., 2021).

cluster of mass 10^{15} $M_{\odot}$ with the β-model using $n_{\rm ICM,0} \sim 10^{-2}$ cm^{-3} and $r_{\rm vir} \sim 2$ Mpc. We see that both profiles look similar up to $\sim 10^3$ kpc (see, Schneider, 2014, for review). Above this scale, the density distribution of our simulated clusters decays much faster than the that of the β-model. We note that the latter was the model employed by Fang and Olinto (2016) in their semi-analytic study of CR propagation and neutrino production in galaxy clusters. In Chapter 5, we will compare our results with theirs and we will see that this difference in the density profiles is important to explain the resulting differences in our study with regard to their model.

Clusters have typical masses in the range $10^{12} \lesssim M/M_{\odot} \lesssim 5 \times 10^{15}$. To estimate the total flux of CRs, neutrinos, and gamma-rays we will we need to evaluate the total number of clusters in our background simulations as a function of their mass, at different redshifts. From the entire simulated volume, (240 Mpc)^3, we selected 20 sub-samples of (20 Mpc)^3 from different regions, as representative of the whole background. We then calculated the average number of clusters per mass interval in each of these sub-samples ($dN_{\rm clusters,\ avg}/dM$), between 10^{12} $M_{\odot}$ and 5×10^{15} $M_{\odot}$. To obtain the total number of clusters per mas interval we multiplied this quantity by the number of intervals $N = (240\ {\rm Mpc})^3/(20\ {\rm Mpc})^3$ in which the whole volume was divided. So, the total number of clusters per mass interval was calculated as $(dN_{\rm clusters,\ \ avg}/dM) \times N$. Since we have seven redshifts in our cosmological background simulations, $z = 0.01,\ 0.05,\ 0.2,\ 0.5,\ 0.9,\ 1.5,\ 5.0$, we then have repeated the calculation above for each snapshot to obtain the number of clusters per mass interval at different redshifts. We note that the number of clusters per mass interval we obtained from our MHD cosmological simulation at different redshifts is comparable with results from other large-scale cosmological simulations (Jenkins et al., 2001; Rosati et al., 2002; Bocquet et al., 2016) (see lower panel of Fig. 2.7) and also with predictions from observations (Giovannini et al., 1999; Tinker et al., 2008).

2.3 *Compatiblity of our MHD Simulations with Observations*

The 3D MHD cosmological simulations of large scale structures employed here (from Dolag et al., 2005), though performed more than a decade ago, are still very updated and more than appropriate for the computation of the CR, neutrino and gamma-ray fluxes we have carried out in this Thesis, as we are going to describe in the next Chapters, in spite of

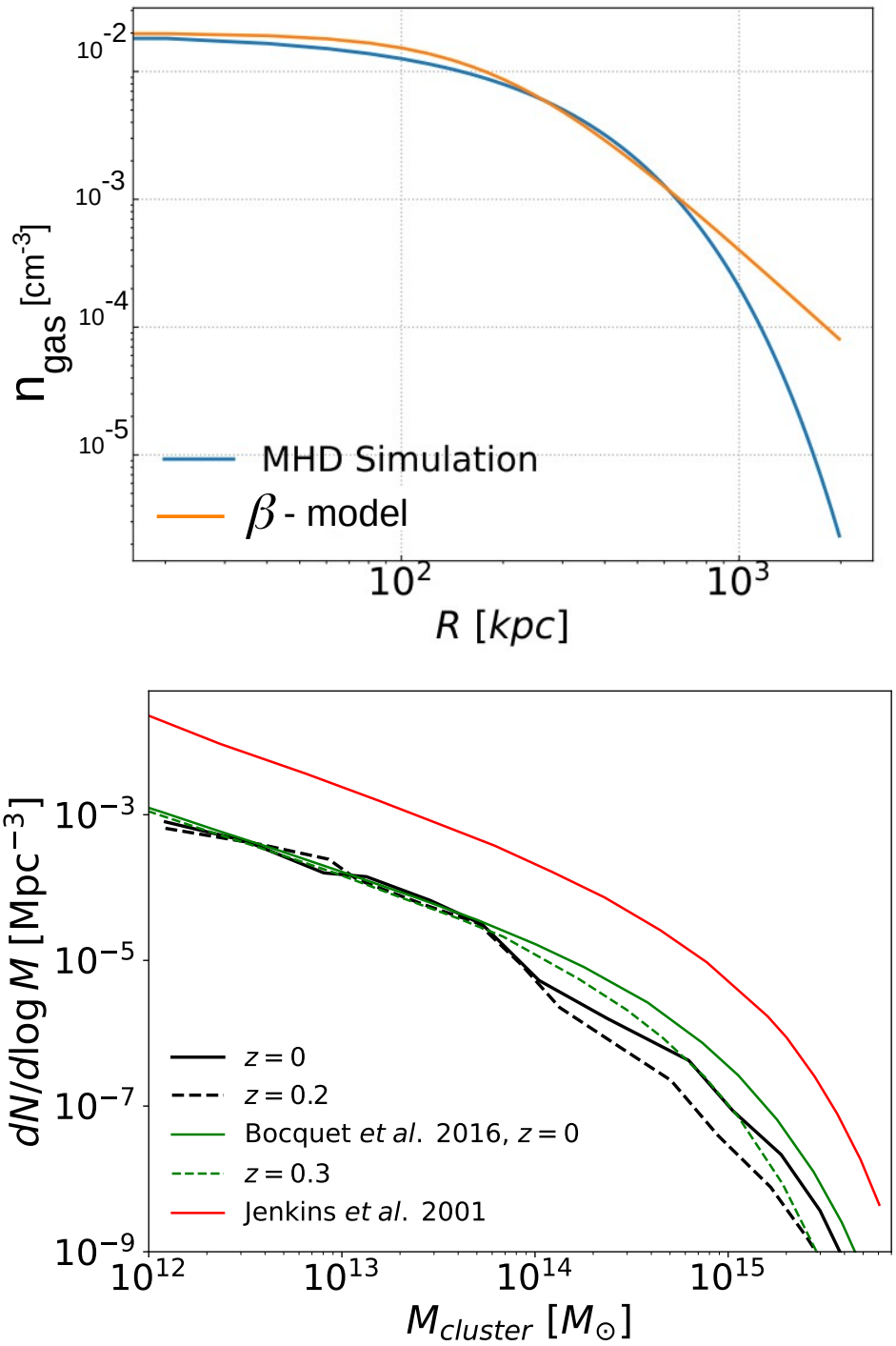

Figure 2.7: Comparison of the density profile of a cluster of mass 10^{15} $M_\odot$, from our simulation with the β-model (Schneider, 2014) used by Fang and Olinto (2016), given in the upper panel. The lower panel shows the number of clusters per mass interval in our cosmological simulation for different redshifts (black lines). It is compared with other large scale cosmological simulations in green lines (Bocquet et al., 2016) and in red line (Jenkins et al., 2001). We note that in Jenkins et al. (2001) (red line) it is presented the total count of clusters as a function of mass starting at redshift $z = 14$ up to $z = 0$. This explains the difference with regard to the other curves.

their minor limitations (see Chapters 4 and 5). In particular, these simulations have been extensively compared with the observations. The correlation of Faraday rotation measurements with x-ray surface brightness for different galaxy clusters was directly obtained from the simulations (see Fig. 5 of Dolag et al., 2005) and compared with the observations of the two massive clusters A 119 (Feretti et al., 1995) and Coma (Feretti et al., 1999). The magnetic field strength as a function of the baryonic overdensity Δ was also derived (see Fig. 7 and 8 of Dolag et al., 2005), they evaluated the projected gas density for a region centred in a large structure around Centaurus, Pavo and A3627. In summary, the results of these simulations on the density, magnetic field and temperatures of clusters of galaxies are comparable with observations of clusters of galaxies.

2.4 Summary of this Chapter

In this Chapter, we presented the properties of the clusters of galaxies derived from the 3D-MHD cosmological simulations performed by Dolag et al. (2005). This is a simulation of large-scale structure formation to study the build-up of density structures and magnetic fields in the intergalactic medium. The basic assumption of this simulation is that cosmological magnetic fields grow as a result of MHD turbulent processes driven by structure formation. The predicted structure of the the magnetic field, density and temperatures in the galaxy clusters, filaments, and voids from these simulations are in good agreement with the observations (e.g., Edge and Stewart, 1991; Ferrari et al., 2008; Feretti et al., 1995, 1999; Dolag et al., 2005; Sanders et al., 2016; Simionescu et al., 2019).

In the next Chapters we are going to use this MHD background to probe the ICM and study the propagation of CRs and production of their by-products, specially gamma-rays and neutrinos.

Chapter 3

Propagation of Cosmic-Rays and their Interaction Processes

The CRs interact with the density and electromagnetic fields as well as with the background relevant photon fields that include Bremsstrahlung, CMB and EBL during their propagation in the intracluster (ICM) and intergalactic medium (IGM). Due to these interactions, CRs produce secondary particles e.g., gamma-rays and neutrinos. To understand the microphysics of CRs and their losses, one has to explore the different propagation mechanisms and interaction processes. In the first half of this Chapter, we discuss the propagation of CRs. In the second half, we focus on different types of interaction processes and their importance in the ICM and IGM.

This Chapter is designed as follows. In Section 3.1, we present a description of the acceleration and propagation model of CRs using Monte Carlo simulations, based on the publicly available code CRPropa 3 (Alves Batista et al., 2016; Merten et al., 2017). The derivation of the photon fields CMB, EBL, and Bremsstrahlung is presented in Section 3.2. In Section 3.3, we describe the CR interaction mechanisms. In Section 3.4, we present the calculation of CR interactions in clusters of galaxies. In Sections 3.5 and 3.6 we describe the diffusion regimes and propagation of CRs in clusters of galaxies.

3.1 Overview of CRPropa 3 code

There are many Monte Carlo codes to study the propagation of high-energy CRs (e.g., Aloisio et al., 2012, 2017; De Domenico et al., 2013), but CRPropa 3 is the most suitable for our research purposes as summarized below. For a more detailed description we refer to Alves Batista et al. (2016); Heiter et al. (2018).

CRPropa 3 is a publicly available Monte Carlo code developed to study propagation of high-energy cosmic rays (HECRs), up to iron nuclei, and their secondaries including gamma-rays and neutrinos through galactic and extragalactic environments (Alves Batista et al., 2013, 2016, 2017). It takes into account all the relevant interactions of CRs: pion production, photodisintegration and energy losses by pair production of all relevant nuclei in the low-energy photon fields (e.g. CMB and EBL). It also considers the nuclear decay process. Furthermore, it computes the deflection of CRs in galactic and extra-galactic magnetic fields.

We can model the production of neutrinos and gamma-rays and the propagation of electromagnetic cascades for different source distributions and magnetic environments using CRPropa 3. It has been used to predict the spectra of CRs with different composition for a very wide energy range, $10^{12} - 10^{22}$ eV, and different arrival direction (Di Sciascio and Iuppa, 2014; Aab et al., 2015; Di Sciascio et al., 2016; Yue et al., 2020; Verzi et al., 2017). The code is very flexible with shared-memory parallelization (using OpenMP) and python interface. One of the builders of CRPropa, Rafael Alves-Batista is a former postdoc in our group and has collaborated with us in this project. A more detailed technical description of the code and its several sub-routines (or modules) is presented in next sub-sections.

A flow chart for the functioning of CRPropa 3 code together with the background MHD simulations of the galaxy clusters performed in this thesis is given in Fig. 3.1.

3.1.1 Propagation of Cosmic Rays

The propagation of CRs can be investigated based on the solution of the Lorentz force equation (single particle approach) or the transport equation (stochastic differential equation -SDE - many particle approach). In the CRPropa code (Alves Batista et al., 2016) the propagation of CRs is studied using both approaches. The main advantage of using the Lorentz equation approach that no assumptions have to be made on the diffusion tensor and arbitrary magnetic field configurations can be used. This makes the simulation more realistic and precise. In addition to that, we can trace the trajectory of distinct particles. However, this method becomes computationally too expensive and time consuming when propagating particles have energies below PeV (e.g., transport of CRs in the galaxies and clusters of galaxies (Kotera et al., 2009; Fang and Olinto, 2016; Merten et al., 2017). On the other hand, the propagation of CR using the SDE enables a good

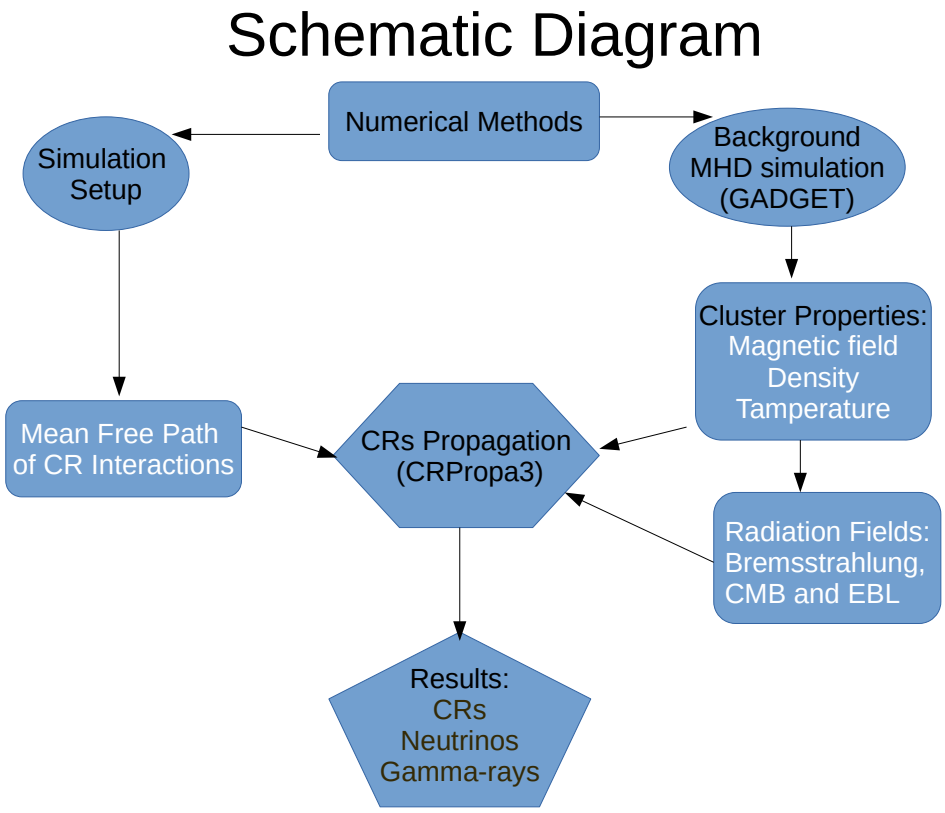

Figure 3.1: Schematic diagram of the combination of the CRPropa 3 code with the background MHD simulations of the clusters that we employ in this Thesis in order to produce the propagation and fluxes of CRs, neutrinos and gamma-rays.

approximate description in different astrophysical environments. The main approximation in this method is to model the transport of the particles via a diffusion tensor (see e.g., Strong and Moskalenko, 1998; Wiener et al., 2013; Merten et al., 2017; Evoli et al., 2017; Lazarian and Xu, 2021; Xu and Lazarian, 2020; Peretti et al., 2019, 2020, 2021, for detail). Therefore, in this Thesis, we will use the SDE approach to investigate the propagation of CRs in the ICM. In the following paragraphs we describe briefly both approaches.

3.1.1.1 Lorentz Equation of Motion

The equation of motion for the propagation of CRs in the magnetic field (B) is given by its momentum change under the effect of the Lorenz force,

$$\dot{\mathbf{P}} = q(\dot{\mathbf{r}} \times \mathbf{B}). \tag{3.1}$$

Where P, q, and r are the particle momentum, charge and position, respectively. This equation is solved in time using a 5th-order Runge-Kutta (R-K) method [1] (Cash and Karp, 1990). This method is adequate for variable step size algorithms, as is the case.

3.1.1.2 Stochastic Differential Equation approach

CRs can be deflected by magnetic fields. Their transport in turbulent media is very complex and requires a detailed modeling to describe the stochastic variations of the pitch angle of the particles in the magnetic fields. For the energies and magnetic field strengths relevant for this study, the propagation of CRs is diffusive or semi-diffusive (see Section 3.5), which leads to scatterings that can be interpreted by means of diffusion coefficients.

To investigate the flux of different particle species and the change of their energy spectrum by processes like advection, diffusion in space and adiabatic cooling, transport equations must be used (Strauss and Effenberger, 2017). The Fokker-Plank equation (FPE, (Risken, 1996)) which is a parabolic partial differential equation describes particle evolution accounting for these processes:

$$\frac{\partial n(\mathbf{x},t;\mathbf{y},t')}{\partial t} = -\sum_i \frac{\partial}{\partial x_i}[A_i(\mathbf{x},t)n(\mathbf{x},t;\mathbf{y},t')] + \frac{1}{2}\sum_{i,j}\frac{\partial^2}{\partial x_i \partial x_j}[B_{ij}(\mathbf{x},t)n(\mathbf{x},t;\mathbf{y},t')] \tag{3.2}$$

[1] R-K methods are the classes of formulas for the numerical integration of the initial value problems. R-K performs several evaluations of a given function around a point and then compute the value for the next point using a weighted average of those values. It can also incorporate the change in step size of integration as often required (Cash and Karp, 1990).

Here, $A_i(\mathbf{x}, t)$ is a drift vector, $B_{ij}(\mathbf{x}, t)$ is the diffusion tensor, $n(\mathbf{x}, t; \mathbf{y}, t')$ is the particle number density at position $\mathbf{x}$ and time t depending on the time t' at position $\mathbf{y}$. $\mathbf{y}$ and $\mathbf{x}$ are the phase space vectors.

Here we use the Parker transport equation (which is modified from of the Fokker-Plank equation) which gives a good description for the particle transport problem in diffusion regimes (Strong and Moskalenko, 1998):

$$\frac{\partial n}{\partial t} + \vec{u}.\nabla n = \nabla.(\hat{\kappa}\nabla n) + \frac{1}{p^2}\frac{\partial}{\partial p}\left(p^2\kappa_{pp}\frac{\partial n}{\partial p}\right) + \frac{1}{3}(\nabla.\vec{u})\frac{\partial n}{\partial \ln p} + S(\vec{x}, p, t). \tag{3.3}$$

where $\vec{u}$ is the advection speed, $\hat{\kappa}$ is the spatial diffusion tensor, p is the absolute momentum, κ_{pp} is the diffusion coefficient of momentum used to describe the particle re-acceleration, n is the particle density and $S(\vec{x}, p, t)$ is the source of CRs (distribution of CRs at the source). CRPropa 3 (Alves Batista et al., 2016) employs the module presented in Merten et al. (2017) to solve the transport stochastic diffusion equation (SDE). To solve the SDE, an adaptive algorithm is applied so that we can vary the integration time step depending on the local magnetic field. Because the phase-space elements (pseudo particles) are independent of each other this makes it easier to parallelise the SDE integration.

For most galactic applications, spatial and momentum operators in Equation 3.3 can be separated, so that we have

$$\begin{aligned} d\vec{r} &= \vec{A}dt + D_r d\vec{\omega}_r \\ dp &= A_p dt + D_{pp} d\omega_p \end{aligned} \tag{3.4}$$

where dt is the time increment, $\vec{A}$ and A_p is the transport vector in spatial and momentum coordinates, D_r and D_{pp} is the spatial and momentum diffusion tensor, respectively, and $d\omega^\mu = \sqrt{dt}\eta^\mu$ is the 4-dimensional Wiener process [2]. We can solve tensors D_r and D_{pp} using the spatial diffusion tensor $\hat{\kappa}$ and momentum diffusion tensor κ_{pp}. We are solving the equations in the local frame of the magnetic field, and we can neglect the drift term. Hence, the diffusion tensor is always diagonal and gives the following relations (for detail see Kopp et al., 2012):

$$D_{ij} = \delta_{ij}\sqrt{2\kappa_{ij}}, \qquad D_{pp} = \sqrt{a\kappa_{pp}}, \tag{3.5}$$

where $D_{ij} \equiv D_r$. This SDE method is compatible with the single particle tracking approach, but it requires the knowledge of the diffusion tensor at the start of simulation. This

[2] Wiener process is the solution of the diffusion equation with zero drift and a constant diffusion coefficient that is equal to 1 (Markov process see e.g., Zhang, 1999; Wang et al., 2019).

is somehow opposite to full orbit simulations where the elements of the diffusion tensor are obtained from the particle trajectories determined from the direct solution of their equation of motion.

In the Euler-Mayurama code scheme (Zahri, 2009; Mao, 2016) [3], at each time step all three vectors of the the trihedron should be calculated (Mao, 2016). which can be used to integrate the SDE when the local orthonormal basis is known, the tangential vector of the magnetic field line $\vec{e}_t$ is calculated via the Cash-Karp (CK) algorithm, an adaptive 5th order R-K algorithm (Cash and Karp, 1990). The methods we are using here also have variable step size and we also use the R-K method. With this algorithm we are able to adapt the time integration step to minimize the number of steps. The local truncation error for the field line integration can be set by the user. In this way the overall computation time is reduced without any losses in accuracy (Alves Batista et al., 2016; Merten et al., 2017).

3.1.1.3 Sources and Spectrum

In CRPropa 3, there are many classes of sources which can emit particles in a specific direction or isotropically, such as uniform distributions within a volume or in one-dimension (1D) direction; a uniform distribution on the surface of a sphere; a grid containing the density of sources in each cell; a list of individual sources. These sources can emit particles in a specific direction, or isotropically. They are implemented within the source class module of CRPropa 3.

CRs can be injected with a monochromatic or a power law spectrum, and a single or many particle types can be defined. In this work we considered sources with a power law spectrum

[3] EM scheme can be derived using Equations (3.4): $\vec{x}_{n+1} = \vec{x}_n + D_r\Delta\vec{\omega}_r$ here $D_r\Delta\vec{\omega}_r = \left(\sqrt{2\kappa_\parallel}\eta_\parallel\vec{e}_t + \sqrt{2\kappa_{\perp,1}}\eta_{\perp,1}\vec{e}_n + \sqrt{2\kappa_{\perp,2}}\eta_{\perp,2}\vec{e}_b\right)\sqrt{h}$, $h = t_{i+1} - t_i$ the integration time step. The orthonormal basis is the local trihedron of the magnetic field line $\vec{B}(\vec{x}_n)$, if it is interpreted as in 3D space curve. It is defined using the Frenet-Serret-equation (Marris and Passman, 1969) as $\vec{e}_t = \vec{B}_{coh}/B_{coh}$, $\vec{B}_{coh}$ is the coherent background field vector, $\vec{e}_t.\Delta\vec{e}_t/k$, $k = |d^2\mathbf{r}/ds^2|$ is the curvature of parametric field line $\mathbf{r}(s)$ and $\vec{e}_b = \vec{e}_t \times \vec{e}_n$, where $\vec{e}_n$ is the vector normal to the magnetic line.

$$\frac{dN}{dE} \propto \begin{cases} E^{-\alpha} & \text{if } E_{\max} > E, \\ E^{-\alpha} exp\left(1 - \frac{E}{E_{\max}}\right) & \text{if } E_{\max} \leq E, \end{cases}$$

where α is the spectral index for injected iron and proton distributions, respectively, and $E_{\max}$ is the maximum energy.

3.1.1.4 Observer

Size and position of the observer can also be fixed in CRPropa 3 code. There are observers designed for detection in the one-dimensional (1D) mode, and in 3D. In 3D mode, the observer can be defined as a sphere of a given radius R_{obs}. The propagation of CRs ends if any of the following conditions are met:

- the particle reaches the observer;
- the energy of the particle becomes smaller than a given minimum energy;
- the trajectory length (user's choice) exceeds the maximum allowed propagation length.

While studying the CR propagation using the SDE we implemented a module that accounts for the time evolution of CR distribution at different time steps defined by the user (see Merten et al., 2017, for details).

3.1.1.5 Energy Loss Algorithm

To study different kinds of CR interactions and energy loss processes CRPropa 3 (Alves Batista et al., 2016) uses the Monte Carlo method which is the best approach to study the probability of different processes to occur during the propagation of CRs in astrophysical environments (see also Alves Batista et al., 2016, for detail). In CRPropa 3, photopion production and photo-disintegration processes are considered as stochastic, while the pair production and adiabatic losses are considered as continuous energy loss processes. All the interaction channels depend on their mean free paths that are discussed in the next sections.

3.2 Background Photon Fields

The cosmic microwave background (CMB) radiation is the leftover heat from the time when Universe began and is also known as relic radiation (e.g., Sunyaev, 1974). This radiation exists everywhere and is in the microwave part of the electromagnetic spectrum. The CMB is well-understood and measured. It has a blackbody spectrum with temperature $T \sim 2.7$ K, and therefore, can be described by the Planck distribution (Penzias and Wilson, 1965; Dicke et al., 1965). Thus, the energy density of CMB is given by

$$n(\epsilon) = \frac{\epsilon^2}{\pi^2 c^3 \hbar^3} \frac{1}{e^{\frac{\epsilon}{k_B T}} - 1}. \tag{3.6}$$

The extragalactic background light (EBL) is a diffuse photon field corresponding to the starlight emitted by galaxies through the history of the Universe. It also has an important contribution from the first stars which are formed before galaxies. It is visible mostly in the optical and infrared bands of the electromagnetic spectrum. Due to the lack of unique spectral signature the measurements of EBL are very difficult. There are several components of the Universe that can affect the EBL spectrum, the most prominent one is the obsorption by the dust. Many works (e.g., Stecker et al., 2006, 2016; Finke et al., 2010; Kneiske et al., 2004; Dominguez et al., 2011; Gilmore et al., 2012) have tried to model this background radiation. In our simulations of CR propagation we used the models by Stecker et al. (2006, 2016); Dominguez et al. (2011); Gilmore et al. (2012) (see Chapter 4). Both radiation fields (CMB and EBL) impact the propagation of HECRs in the energy range of interest of this work.

To perform the CR propagation in the ICM, we also need the distribution of photons within the clusters. The hot X-ray radiation produced in the ICM is the Bremsstrahlung radiation [4] (e.g., Brunetti and Jones, 2014). These thermal X-ray photons produced in the hot ICM ($T \sim 10^7 - 10^8$ K) may serve as the target fields for CRs interactions depending on their density in the central regions of clusters, in particular, this effect may be considerable.

Here we explain in detail the implementation of local Bremsstrahlung photon field of the ICM and also compare our background simulation with some results in the literature. The Bremsstrahlung photon density in different regions of the cluster is not constant. As

[4] Radiation due to the acceleration of a charge in the Coulomb field of another charge is called Bremsstrahlung or free-free emission.

stressed in Chapter 2, the Cartesian coordinates of the background simulation of a given cluster can be converted to spherical coordinates using the transformations given below

$$R = \sqrt{(C_x - X)^2 + (C_y - Y)^2 + (C_z - Z)^2}, \tag{3.7}$$

$$\phi = \tan^{-1}\left(\frac{C_y - Y}{C_x - X}\right), \quad \theta(0,\pi) = \tan^{-1}\left(\sqrt{\frac{(C_x - X)^2 + (C_y - Y)^2}{(C_z - Z)}}\right). \tag{3.8}$$

Using these transformations one can divide a cluster in shells of different radius. Starting from the center of the cluster, the shells were first divided in intervals of 100 kpc, then between 300 kpc and 1500 kpc, they were divided in intervals of 200 kpc, and the last shell in the outskirts was taken between 1500 kpc $< R_{\rm shell} <$ 2000 kpc. We use this configuration to calculate the photon density distribution due to Bremsstrahlung in each shell using a procedure given below. The specific intensity I_ν of Bremsstrahlung field is defined as

$$I_\nu = B_\nu\Big(1 - \exp(-\tau_\nu)\Big), \tag{3.9}$$

$$B_\nu(T) = \frac{2h\nu^3/c^2}{\exp(h\nu/k_BT) - 1} \quad \text{and} \quad J_\nu^{\rm ff} = \frac{\epsilon_\nu^{\rm ff}}{4\pi} \tag{3.10}$$

For an optically thin region where there is no absorption of photons, $\tau_\nu \approx R_{\rm shell}\frac{J_\nu^{\rm ff}}{B_\nu}$ and Equation (3.9) with first order expansion [5] becomes

$$I_\nu = B_\nu\big(1 - (1 - \tau_\nu)\big) = B_\nu\tau_\nu = R_{\rm shell}J_\nu^{\rm ff} = \frac{R_{\rm shell}}{4\pi} \times \epsilon_\nu^{\rm ff}. \tag{3.11}$$

The number of photons per unit energy is

$$\frac{dn_{\rm ph}}{d\epsilon} = \frac{4\pi I_\nu}{ch\epsilon} = \frac{4\pi}{ch\epsilon} \times R_{shell}J_\nu^{\rm ff} = \frac{1}{ch\epsilon} \times R_{\rm shell}\epsilon_\nu^{\rm ff}, \tag{3.12}$$

$\epsilon^{ff}(\nu, n, t)$ is given by:

$$\varepsilon^{\rm ff}(\nu, n, t) = \frac{dW}{d\nu dV dt} = 6.8 \times 10^{-38} Z^2 n_e n_i T^{-1/2} e^{-h\nu/k_BT} g_{\rm ff}, \tag{3.13}$$
$$g_{\rm ff} = \frac{\sqrt{3}}{\pi} \ln\left(\frac{9k_BT}{4h\nu}\right),$$

where $g_{\rm ff}$ is the Gaunt factor. The spectrum described by the Equation (3.13) is flat for $h\nu \ll k_BT$ and exponentially decreasing for $h\nu \geq k_BT$. The values of $g_{\rm ff}$ for $h\nu/k_BT$

[5] $e^{-x} = 1 - \frac{x}{1!} + \frac{x^2}{2!} + ...$

are not important because the spectrum cuts off at these values. Actually, $g_{\rm ff}$ is unity for $h\nu \approx k_B T$ and is in the range $1-5$ for $10^{-4} < h\nu/k_B T < 1$ (see Fig. 5.3 in Rybicki and Lightman, 1986).

Using Equations (3.9 - 3.13) we calculate the Bremsstrahlung photon field. The number of photons per unit energy is plotted in Fig. 3.2 as a function of the photon energy for two background gas temperatures (10^4 K and 8×10^7 K). One can see that the Bremsstrahlung photon field, for high temperature is not important, specially for low density gas. This is the case of the optically thin ICM, for which the maximum number density is $\sim 10^{-2}$ cm^{-3} and the temperature is above $T \gtrsim 5\times10^6$ K.

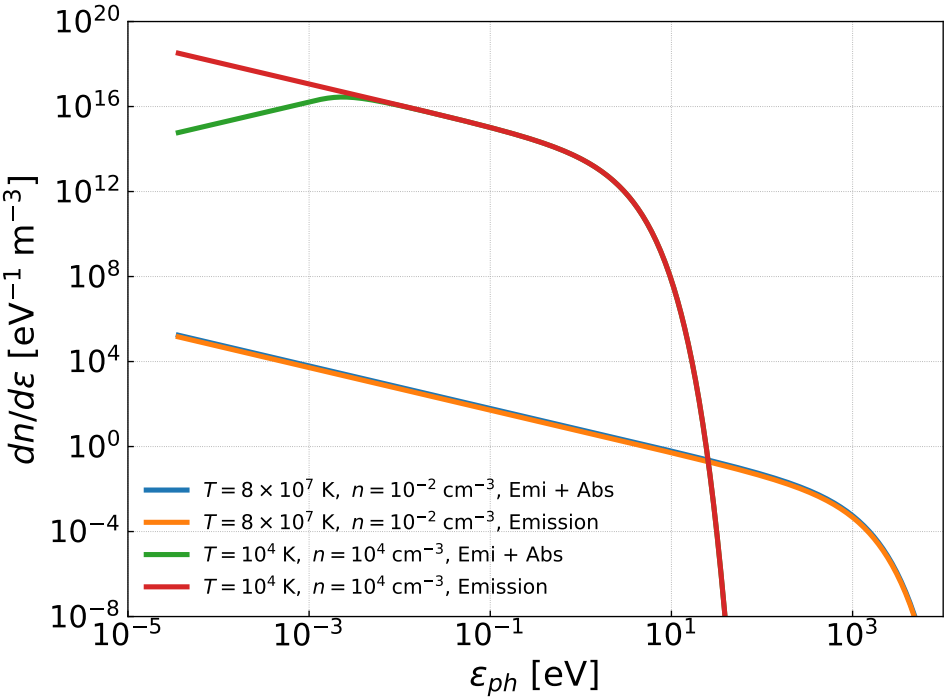

Figure 3.2: Bremsstrahlung photon field as a function of the background gas temperature for different gas densities. It is important only for low temperature and high density. Emission plus absorption (Equations 3.9, 3.11, and 3.12) is compared with emission only.

In Fig. 3.3 we compare the radiation fields for two EBL models (Dominguez et al., 2011; Gilmore et al., 2012) with the Bremsstrahlung photon fields of two clusters of masses 10^{15} $M_\odot$ (cluster 1) and 2×10^{14} $M_\odot$ (cluster 2). For both clusters, we calculated the internal photon field at the central region ($R < 100$ kpc) and in the outskirts. It can be seen that the Bremsstrahlung photon field is dominant at X-rays, but only near the center of the clusters, while the EBL dominates at infrared and optical wavelengths mainly.

The mean free path (MFP) of CRs interactions with the Bremsstrahlung photon fields

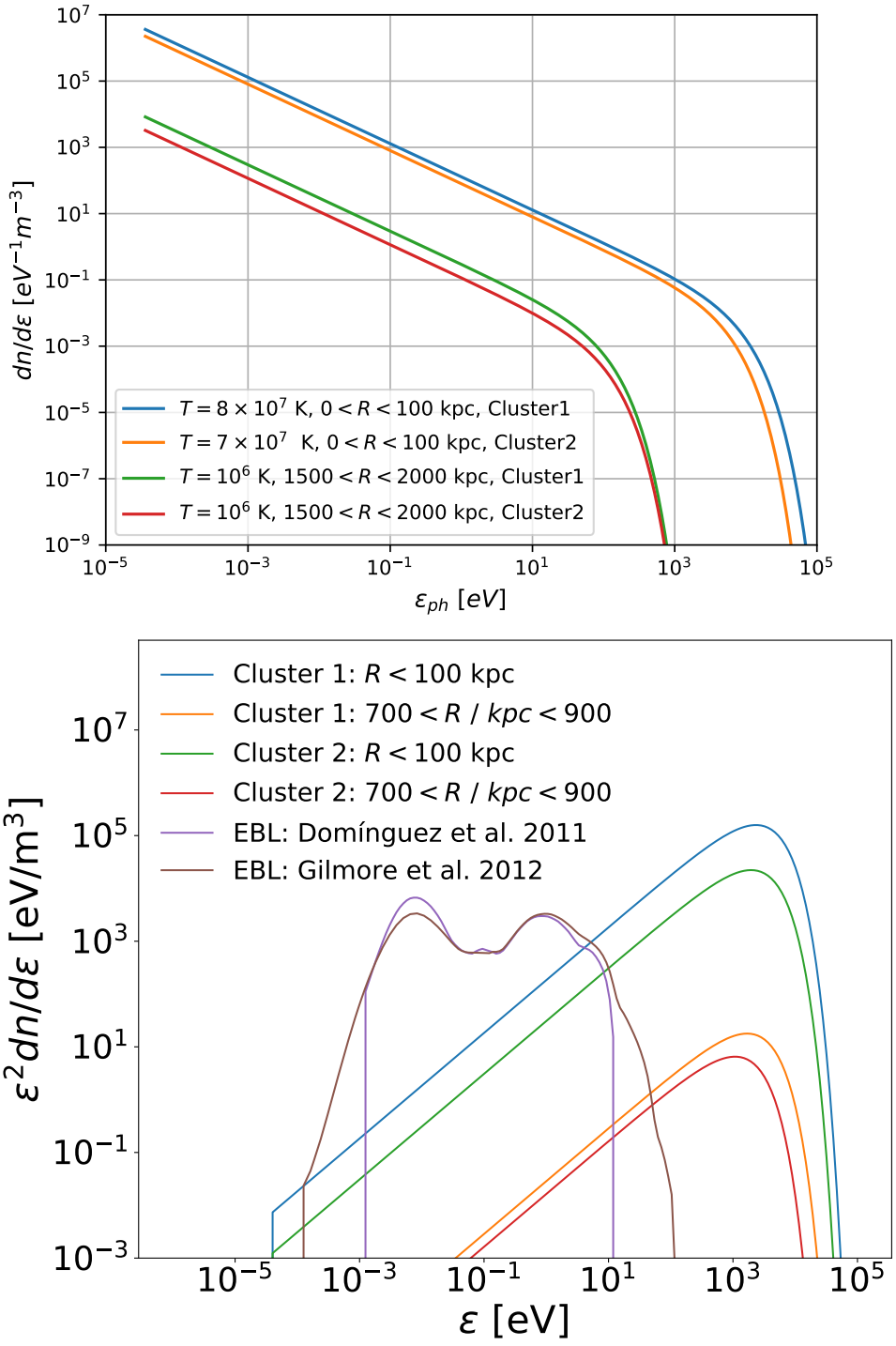

Figure 3.3: Panel (a) shows the Bremsstrahlung photon field of two clusters of distinct masses (10^{15} $M_\odot$ and 2×10^{14} $M_\odot$), cluster 1 and 2, respectively chosen from our background MHD simulation (Dolag et al., 2005). Panel (b) shows the comparison of two EBL models with the local photon field of the two clusters in the central region and in the outskirt.

in each shell were also calculated (see Fig. 3.6) and implemented in CRPropa 3. Our computation of these quantities in CRPropa 3 have revealed no significant contribution of the Bremsstrhalung photons to the production of neutrinos or gamma-rays. Indeed, the upper panel of Fig. 3.6 indicates that the MFP for these interactions is larger than the Hubble horizon. Thus, deviations from spherical symmetry for this photon field will not be relevant in this study.

3.3 *Interactions and Energy Losses of the Cosmic-Rays*

In this Section, we discuss all the interactions and radiative losses during the propagation of CRs. We include the CR interactions and their energy losses due to interactions with magnetic fields, and the background radiation fields (Bremsstrhalung, CMB and EBL).

Here we assume that CRs were produced (accelerated) [6] in astrophysical sources (CR accelerators) inside the clusters, like the surroundings of black holes in the nuclei of galaxies, relativistic jets, starburst galaxies, etc (see Chapter 1). These sources can produce relativistic particles (CRs) which include protons, ions, and electrons and positrons. The energy loss time of electrons/positrons is much faster than that for protons/ions. They lose most of their energy before they escape from the source, via curvature radiation in strong magnetic fields, synchrotron radiation, and inverse Compton radiation (e.g., Fang et al., 2012; Fang and Murase, 2018; Alves Batista et al., 2015, 2019; Rodríguez-Ramírez et al., 2019; Aab et al., 2020). On the other hand, the protons/ions are more stable and therefore, survive and can escape from the sources, being able to propagate over large distances in the cosmos until they reach the Earth, the larger their energy the better (e.g., Knežević, 2014; Buckman et al., 2020; Mollerach and Roulet, 2020; Sokolsky and Thomson, 2020). That is why we investigate the propagation of CRs considering protons/ ions. Now, a CR when propagating in the turbulent magnetized intergalactic medium (IGM), will be deflected in the magnetic field, will collide with other lower energy nuclei of the background, and also interact with the background photons (CMB and EBL). CRPropa 3 is able to consider all these interactions. These interactions produce gamma-rays; the interactions of these gamma-rays with background photons lead to the production of electron-positron pairs;

[6] The investigation of the mechanisms of CR acceleration is out of the scope of this Thesis. Instead, we assume that the CRs are accelerated to their high-energies in known sources or accelerators inside the clusters and then we follow their propagation through the environment.

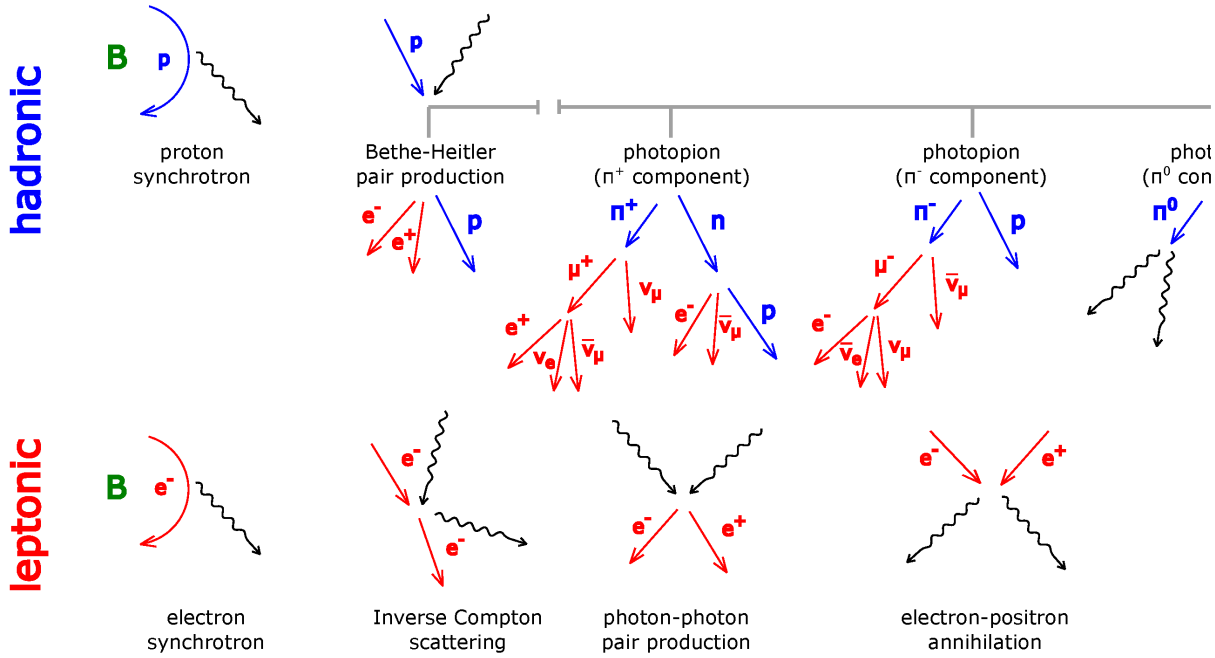

Figure 3.4: Schematic diagram of CRs and gamma-rays air shower (Mastichiadis, 2016)

these pairs in turn will interact with CMB and produce secondary gamma-rays.

We note that the chemical composition of the CRs that we consider in this work is of only protons because they are more abundant at energies below 10^{18} eV (Apel et al., 2013; Buitink et al., 2016; Thoudam et al., 2016; Dembinski, 2019; Tjus and Merten, 2020), see however Appendix D for a comparison of CR spectra of different compositions.

In Fig. 3.4, we show the schematic diagram of CR interactions with the background fields (Mastichiadis, 2016). We describe these processes below.

3.3.1 *PhotoPion Production*

Photopion production occurs when a CR scatters off a background photon. This interction process for a protons can be written as

$$p + \gamma \longrightarrow \begin{cases} p + \pi^0, \\ p + \pi^+ \end{cases}$$

The pions produced in this process decay and then produce gamma-rays and neutrinos (see Fig. 3.4 and 3.5.) The threshold energy for a pion production can be written as

$$E_{\rm thr} = \frac{m_\pi c^4 (m_p + 0.5 m_\pi)}{2\epsilon} \tag{3.14}$$

where m_p and m_π are the masses of proton and pion. For a background photon of energy $\epsilon \sim 10^{-3}$ eV the threshold energy (E_{thr}) for this process is $\sim 6 \times 10^{19}$ (Heiter et al., 2018).

Protons lose $\sim 20\%$ of their energy in photo-meson processes. The effective cutoff in this process takes place at energy 6×10^{19} eV, the GZK limit (Greisen, 1966; Zatsepin and Kuz'min, 1966)). For detailed calculations of the photopion production loss mechanisms see e.g., Mücke et al. (2000) and Harari et al. (2006).

For a nucleus of mass number (A) and atomic number (Z), the mean free path (λ) for photopion production can be written as (Alves Batista, 2015)

$$\lambda \approx 1.18/\mathrm{Mpc}\left(\frac{Z^a}{\lambda_p(E/A)} - \frac{(A-Z)^a}{\lambda_n(E/A)}\right)^{-1}, \tag{3.15}$$

where λ_n and λ_p are the mean free path of neutron and proton, respectively, $a = 2/3$ if $A \leq 8$, otherwise $a = 1$. The above Equation 3.15 is an approximation (see Kampert et al., 2013, for detail). In CRPropa 3 photopion production is handled by the SOPHIA code (Mucke et al., 1999; Mücke et al., 2000). We will further discuss the mean free path of this process in the next Section.

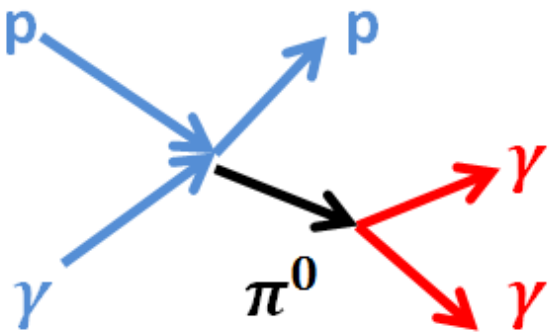

Figure 3.5: Schematic diagram of photopion production that leads to γ-rays.

3.3.2 Bethe-Heitler Pair Production

The production of e^+e^- pairs on a nucleus with energy E, mass number A and atomic number Z is:

$$\gamma + A \rightarrow e^+e^- + A. \tag{3.16}$$

The cross-section for the interaction of a proton of energy $E = \gamma_p m_p c^2$ with a photon of energy $x = \epsilon/m_e c^2$ is given by

$$\langle \sigma_{BH}(\gamma_p,\ x) \rangle = \frac{1}{2} \int_{-1}^{\cos\theta_{min}(\gamma_p,\ x)} (1 - \beta_p \cos\theta) \sigma(s) d\cos\theta, \tag{3.17}$$

where θ is the angle between photon and proton momenta, $\theta_{min}(\gamma,\ x)$ is the minimum value of the angle, $s = m_p^2 c^4 + 2\epsilon E(1 - \beta_p \cos\theta)$ is the square of center of mass energy, $\beta_p = v/c$, and σ_{BH} is the Bethe-Heitler cross-section. For head-on collision the Equation 3.17 can be written as (Motz et al., 1969; Maximon, 1977):

$$\langle \sigma_{BH}(\gamma_p,\ x) \rangle = \frac{1}{\beta_p E^2 \epsilon^2} \int_{s_{\rm min}}^{s_{\rm max}(\gamma_p,\ x)} \sigma(s)(s - m_p^2 c^4) d\cos\theta ds, \tag{3.18}$$

where

$$s_{\rm min} = (m_p c^2 + 2 m_e c^2)^2 \approx 0.88\ {\rm GeV}^2, \tag{3.19}$$

and

$$s_{\rm max}(\gamma,\ x) = m_p^2 c^4 + 2\gamma_p m_p c^2\ x m_e c^2 (1 + \beta_p). \tag{3.20}$$

In this process the proton looses a small amount of energy usually defined by $\Delta\gamma_p = m_e/m_p$.

The energy loss rate for a nucleus of atomic number Z can be written as (Schlickeiser, 2013)

$$-\frac{dE}{dt} = \frac{3c\alpha\ \sigma_T\ Z^2\ m_e^2 c^4}{8\pi} \int_2^\infty d\xi n \left(\frac{\xi m_e c^2}{2\gamma}\right) \frac{\phi(\xi)}{\xi^2}, \tag{3.21}$$

where σ_T is the Thomson cross-section, $\phi(\xi)$ is given by Blumenthal (1970). The threshold energy in this process can be defined as (Alves Batista, 2015; Heiter et al., 2018) $m_e c^4 (m_A + m_e)/\epsilon$, where m_A is the mass of the nucleus. For a background photon of energy $\epsilon \sim 10^{-3}$ eV the threshold energy for pair production is $\sim 5 \times 10^{17}$ eV (Alves Batista, 2015; Heiter et al., 2018) which is roughly two orders of magnitude less than photopion production. The high-energy electrons produced in this process can produce gamma-rays of energy $\lesssim 10^{15}$ eV through inverse Compton scattering. This process is considered as a continuous energy loss in CRPropa 3 due to the very small inelasticity of the order of $\sim 10^{-3}$. To implement this process in CRPropa 3, a parametrization is followed from Chodorowski et al. (1992) and the energy distribution of pairs produced follows from Kelner and Aharonian (2008).

3.3.3 Photo Disintegration

The photo-disintegration process is described as the splitting of heavy nuclei into light nuclei due to their interaction with the background photons. In this process the nucleus often emits particles like neutron, proton and/or alpha.

The cross-section of photo-disintegration is the combination of two processes, the giant dipole resonance (GDR) and quasi-deuteron (QD):

$$\sigma(\epsilon) = \sigma_{\rm GDR}(\epsilon) + \sigma_{\rm QD}(\epsilon), \tag{3.22}$$

where $\sigma_{\rm GDR}$ and $\sigma_{\rm QD}$ are given by Koning and Delaroche (2003); Koning et al. (2005, 2013). The TALYS 1.8 code (Koning et al., 2005; Khan et al., 2005) is used in CRPropa 3 for the photo nuclear cross-section and also to predict the photo-disintegration products of different nuclei and their isotopes.

3.3.4 Nuclear Decay (electrons, photons, neutrinos)

Nuclear decay is the process in which an unstable heavy nucleus converts to a light nucleus by emitting beta or alpha, or both particles. Radiation like gamma-rays can also be produced in this process. These unstable nuclei can be produced by the photopion production or photo-disintegration. For a nucleus of mass number A and atomic number Z, alpha and beta ($\pm$) decay can be written as:

$$^{A}_{Z}X \rightarrow {}^{A-4}_{Z-2}X' + {}^{4}_{2}He, \tag{3.23}$$

$$^{A}_{Z}X \rightarrow {}^{A}_{Z+1}X' + e^{-} + \bar{\nu}_e, \tag{3.24}$$

$$^{A}_{Z}X \rightarrow {}^{A}_{Z-1}X' + e^{+} + \nu_e, \tag{3.25}$$

where X' represents the new nucleus after the decay. This process is implemented in CRPropa 3 based on NuDat 2.6 database (see Sonzogni, 2005, for details).

3.3.5 Electromagnetic Pair Production

This process is defined as the creation of electron-positron ($e^{\pm}$) pairs due to the collision of two photons, a gamma-ray photon and a lower energy background photon: $\gamma + \gamma \rightarrow e^{+} + e^{-}$. The flux of high-energy gamma-rays traversing large distances can be attenuated

due to pair production (Kneiske et al., 2004; Gilmore et al., 2009). It is possible only above the kinetic energy threshold given by (Aharonian and Atoyan, 1991; Pe'er and Waxman, 2004; Ioka et al., 2007):

$$E_\gamma \epsilon (1 - \cos\theta) \geq 2 m_e^2 c^4, \tag{3.26}$$

where E_γ and ϵ are the energies of the emitted gamma-ray and the background photons, respectively, and θ is the collision angle in the laboratory reference frame. The optical depth is defined as:

$$d\tau = (1 - \cos\theta)\, n_{\rm ph}\, \sigma_{\gamma\gamma}\, d\epsilon\, d\Omega\, dl, \tag{3.27}$$

where $d\Omega$ is the solid angle of the target photons, l is the path along the gamma-ray emission and $n_{\rm ph}$ is the photon density of the surrounding field. For a pair production, the $\gamma\gamma$ interaction cross-section $\sigma_{\gamma\gamma}$ is defined as (Lee, 1998)

$$\sigma_{\gamma\gamma}(\epsilon, E_\gamma) = \frac{3\sigma_T}{16}(1-\zeta^2)\left[2\zeta(\zeta^2-2) + (3-\zeta^4)\ln\left(\frac{1+\zeta}{1-\zeta}\right)\right], \tag{3.28}$$

$$\zeta = \left[1 - \frac{(2m_e c^2)^2}{s}\right]^{\frac{1}{2}}, \tag{3.29}$$

for more detail about the energy cascade in this process see Lee (1998) and Heiter et al. (2018). For double pair production in CRPropa 3, the parameterization is taken from Brown et al. (1973) and for triplet pair production it is followed from Lee (1998).

3.3.6 *Inverse Compton Scattering*

The Inverse Compton Scattering (ICS) can produce high energy X-rays and/or gamma-rays in many astrophysical environments. The ICS is described as the scattering of a low energy photon (ϵ) by a relativistic electron. The cross-section ($\sigma_{\rm ICS}$) of this process is given by Lee (1998)

$$\sigma_{\rm ICS} = \frac{3\ \sigma_T\ m_e^2 c^4}{8\ s}\frac{1}{H}\times \left[\frac{2}{H(1+H)}(2+2H-H^2-2H^3) - \frac{1}{H^2}(2-3H^2-H^3)\left(\frac{1+H}{1-H}\right)\right], \tag{3.30}$$

where $H = (s - m_e^2 c^4)/(s + m_e^2 c^4)$, s is the square of center of mass energy and we are in the Klein-Nishina regime if $s \gg m_e^2 c^4$ (Lee, 1998). For further detail and its implementation in CRPropa 3 see Alves Batista (2015); Heiter et al. (2018).

3.3.7 Synchrotron Radiation

The CRs, especially the electrons and positrons, may loose their energy via synchrotron radiation. Synchrotron emission is a type of non-thermal radiation generated by relativistic charged particles spiraling around magnetic field lines. Since the electrons are always changing direction, they are accelerating and emitting photons with frequencies determined by their speed. The synchrotron radiation power can be written as (Gliozzi et al., 1996)

$$P = \frac{4}{3}\sigma_T \beta^2 \gamma^2 \epsilon_B, \tag{3.31}$$

where $\sigma_{\rm T}$ is Thompson cross-section, $\epsilon_{\rm B}$ is the energy density of the magnetic field At fixed energy the synchrotron energy losses are more effective for an electron than a proton because, $\sigma_{\rm T} \propto m^{-2}$ and $\gamma = \frac{E}{mc^2}$, so that $P \propto m^{-4}$. In Astrophysical sources, the synchrotron emission is observed wherever relativistic electrons are present. This radiation is observed in sources such as pulsars, SNRs, AGNs, galaxy clusters, generally from radio to X-ray wavelengths (Aharonian et al., 2006; Brunetti et al., 2008; Ishibashi and Courvoisier, 2011; Shulevski et al., 2015; Holler et al., 2015; Nagai and Kawakatu, 2021).

Synchrotron losses are implemented following Jackson (1999). The energy loss per unit distance for a relativistic charged particle can be written as (Heiter et al., 2018)

$$-\frac{dE}{dx} = \frac{1}{6\pi\epsilon_0}\frac{e^2\gamma^4\beta^4}{r_o^2} \tag{3.32}$$

where $r_o = p/qB_\perp$ is the gyroradius, p, q, γ the momentum, charge and Lorentz factor of the partilce, respectively, here $\beta = v/c$, and ϵ_0 is the permittivity of free space. The typical energy range of this radiation is $\lesssim$ GeV. There are many galactic (e.g., Pshirkov et al., 2011; Jansson and Farrar, 2012; Kleimann et al., 2019) and extra-galactic magnetic field (e.g., Dolag et al., 2005; Alves Batista et al., 2017; Hackstein et al., 2018) models implemented in CRPropa 3.

3.3.8 Adiabatic Losses

The adiabatic expansion of the universe is also a source of energy loss, especially for CRs traveling from large distances. For a CR of energy E this energy loss can be written as (Berezinsky and Gazizov, 2006)

$$E = \frac{E_0}{1+z}, \tag{3.33}$$

where E_0 denote the initial energy. Adiabatic energy losses are not very prominent for UHECRs, but they are dominant if the the energy of CRs is < 1 EeV, specially from large redshift.

3.4 Mean Free Paths for Different CRs Interactions

As remarked, we employ the Monte Carlo method (CRPropa 3) to study particle propagation in clusters of galaxies. In order to calculate the different CR interactions we calculated their rates. We implemented the spatially-dependent interaction rates into the code, based on the gas and photon density distributions for the clusters of different masses obtained from the MHD simulations. Here we describe and compare the mean free paths (MFP), λ, for the different interactions of CRs.

The MFP for pair production $\lambda_{\gamma\gamma}$, for a gamma-ray of energy E_γ propagating through background photons with energy ϵ, $\lambda_{\gamma\gamma}$ is given by (Alves Batista, 2015)

$$\lambda_{\gamma\gamma}^{-1}(E_\gamma) = \frac{1}{8E_\gamma^2}\int_{s_{\min}}^{s_{\max}}\int_{\epsilon_{\min}}^{\infty}\frac{n_{ph}(\epsilon)}{\epsilon^2}s\sigma_{\gamma\gamma}(s)dsd\epsilon, \tag{3.34}$$

where s is the square of center of mass energy and can be written as $s = 2E_\gamma\epsilon(1-\cos\theta)$, θ is the same angle defined in Equation 3.26, $s_{\min} = 2m_e^2c^4$, and $s_{\max} = 4E_\gamma\epsilon_{max}$. For the EBL photon field $\epsilon_{\min}$ and $\epsilon_{\max}$ are $\sim 10^{-3}$ eV and ~ 10 eV, respectively.

The MFP of inverse Compton scattering (ICS) (where E is the energy of the incident photon, and ϵ is the energy of the background photon) can be written as

$$\lambda_{ICS}^{-1}(E) = \frac{1}{8\beta E^2}\int_0^{\infty}\int_{s_{min}}^{s_{max}}\frac{n_{ph}(\epsilon)}{\epsilon^2}\sigma_{ICS}(s)(s-m_e^2c^4)dsd\epsilon, \tag{3.35}$$

where $s = m_e^2c^4 + 2E\epsilon(1-\beta\cos\theta)$, $\beta = \sqrt{1-m_e^2c^4/E^2}$, $s_{\min} = m_e^2c^4$, and $s_{\max} = m_e^2c^4 + E\epsilon_{\max}(1+\beta)$ (see Kachelrieß et al., 2012, for detail). In Equations (3.34) and (3.35) $n_{\rm ph}$ is the background photon field, $\sigma_{\gamma\gamma}$ (Equation 3.28) and $\sigma_{\rm ICS}$ (Equation 3.30) are the cross-section for the electromagnetic pair production and ICS, respectively (see also Alves Batista, 2015, and reference therein).

The MFP for photopion production for a proton of mass m_p, energy E_p, and Lorentz factor $\gamma_P = E_p/m_pc^2 = (1-\beta_p^2)^{-1/2}$, traversing an isotropic photon field of energy ϵ can be written as (Mücke et al., 2000)

$$\lambda_{p\gamma}^{-1}(E_p) = \frac{1}{8E_p^2\beta_p}\int_{\epsilon_{\rm th}}^{\infty}\int_{s_{\rm th}}^{s_{\rm max}}\frac{n_{\rm ph}(\epsilon)}{\epsilon^2}(s-m_p^2c^4)\sigma_{p\gamma}(s)dsd\epsilon \tag{3.36}$$

where $\sigma_{p\gamma}$ is the photohadronic cross-section, $s = m_p^2c^4+2E_p\epsilon(1-\beta_p\cos\theta)$, θ is the collision angle between the momenta of proton ($\vec{P}_p$) and photon ($\vec{P}_\gamma$), $s_{\rm max} = m_p^2c^4 + 2E_p\epsilon(1+\beta_p)$, and $\epsilon_{\rm th} = (s_{\rm th}-m_p^2c^4)/2(E_p+P_pc)$. The threshold energy for the production of photo-meson is $s_{\rm th} = (m_pc^2 + m_{\pi^0}c^2)^2$.

The MFP of the interactions of CRs with the background photon fields is plotted in Fig. 3.6 for a cluster of mass 10^{15} $M_\odot$, as an example. The figure compares the MFP due to Bremsstrahlung with the EBL and CMB contributions. For modeling the EBL, we considered Gilmore et al. (2012) and Dominguez et al. (2011). For the clusters we only used the Bremsstrahlung photon field within a radius of 100 kpc from the center of the cluster i.e., the densest region, see Fig. 2.4 in Chapter 2. The MFP for single and double pair production is plotted in the lower panel of Fig. 3.6. Lower panel indicates that the pair-production in the CMB photon field is much more dominant than the contributions due to EBL and the Bremsstrahlung. Specially Bremsstrahlung contribution, it is very unlikely to occur because the MFP is greater than the size of the universe ($\geq 10^4$ Mpc) at energy $E \approx 10^{17}$ eV. For double pair production the MFP for EBL also is larger than $\geq 10^4$ Mpc.

For triplet pair production (upper panel of the Fig.3.6) the MFP for CMB is of the order 10 kpc, i.e., much smaller than the total trajectory length ($10^{-1} - 10^3$ Mpc) of the CRs inside the cluster, so that it is much more dominant than the EBL and Bremsstrahlung contributions. The EBL triplet pair-production is also important as its MFP is 10 Mpc, but for Bremsstrahlung it is again comparable to the size of the universe. In summary, high-energy CR interactions with CMB photons is a well established dominant phenomenon known as GZK process and it can be seen that the MFP of this interaction is much smaller than the EBL and the local Bremsstrahlung photon field contributions.

Upper panel of Fig. 3.6 also shows that the MFP of photopion production in the local Bremsstrahlung is greater than the size of the universe ($\geq 10^6$ Mpc) and for the EBL is of the order of $\sim 10^3$ Mpc. In the case of ICS (Fig. 3.6 upper panel) the CMB interaction with CRs is also more dominant at energy $\lesssim 10^{17}$ eV. The MFP for EBL (≈ 100 Mpc) is two orders of magnitude smaller than that of local Bremsstrahlung ($\geq 10^4$ Mpc) at energy $E \approx 10^{17}$ eV and also larger than the size of the universe.

Fig. 3.6 also shows that we can neglect the CRs interactions with the local Bremsstrahlung photon field for energy $E \geq 10^{16}$ eV.

We also implemented the hadronuclear interaction (CR interactions with the gas inside clusters) using a separate module. The parameterization of this process is followed from Kelner et al. (2006); Kafexhiu et al. (2014). For proton-proton (pp) interaction, the rate, defined as the inverse of MFP, is

$$\lambda_{\rm pp}^{-1}(E_p, r_i) = K_{\rm pp}\sigma_{\rm pp}(E_p)n_i(r_i) \tag{3.37}$$

Where $K_{\rm pp} = 0.5$ is the inelasticity factor, $n_i(r_i)$ is the gas number density and E_p is the energy of the protons. To obtain the number density we assume that the background gas consists of only protons and electrons, which is a reasonable assumption for the ICM. Therefore, the gas density is dominated by the proton mass, $\rho_{\rm gas} = m_{\rm proton}n_{\rm gas} \implies n_{\rm gas} = \rho_{\rm gas}/m_{\rm proton}(1/{\rm cm}^3)$. For $\sigma_{\rm pp} = 70$ milli-barn (mb) $\implies$ 1barn $= 10^{-29}$ m^2, we used (Kelner et al., 2006; Kafexhiu et al., 2014):

$$\sigma_{\rm pp} = \left[30.7 - 0.96\log\left(\frac{E_p}{E_p^{\rm th}}\right) + 0.18\log\left(\frac{E_p}{E_p^{\rm th}}\right)\right] \times \left[1 - \left(\frac{E_p^{\rm th}}{E_p}\right)^{1.9}\right]^3 \text{ mb}, \tag{3.38}$$

where E_p is the energy of the proton and $E_p^{\rm th}$ is the threshold kinetic energy $E_p^{\rm th} = 2m_\pi + m_\pi/m_p \approx 0.2797$ GeV. We used Equations 3.37 and 3.38 to calculate the MFP of pp interaction $\lambda_{\rm pp}$. This MFP and the one calculated in the Bremsstrahlung photon field, $\lambda_{p\gamma}$, as a function of the distance in the cluster, are plotted in Fig. 3.7. One can see that the MFP for photopion production is much larger than the size of the universe (as we have already seen in Fig. 3.6) and the MFP of pp interaction is comparable with the trajectory length of the CRs inside the cluster of galaxies. Thus, the proton-proton interaction is most likely to occur than photo-pion production due to Bremsstrahlung.

Fig. 3.8 shows the distribution of the trajectory lengths, for different energy bins of CRs. There is a substantial number of events with trajectory length greater than $D \gtrsim 10^3$ Mpc for each energy bin. Thus, the trajectory lengths of CRs are comparable to the MFP of pp-interactions (see upper panel of the Fig. 3.7) and photopion production in the CMB and EBL case (see upper panel of the Fig. 3.6), so that these interactions can produce secondary particles including gamma rays and neutrinos.

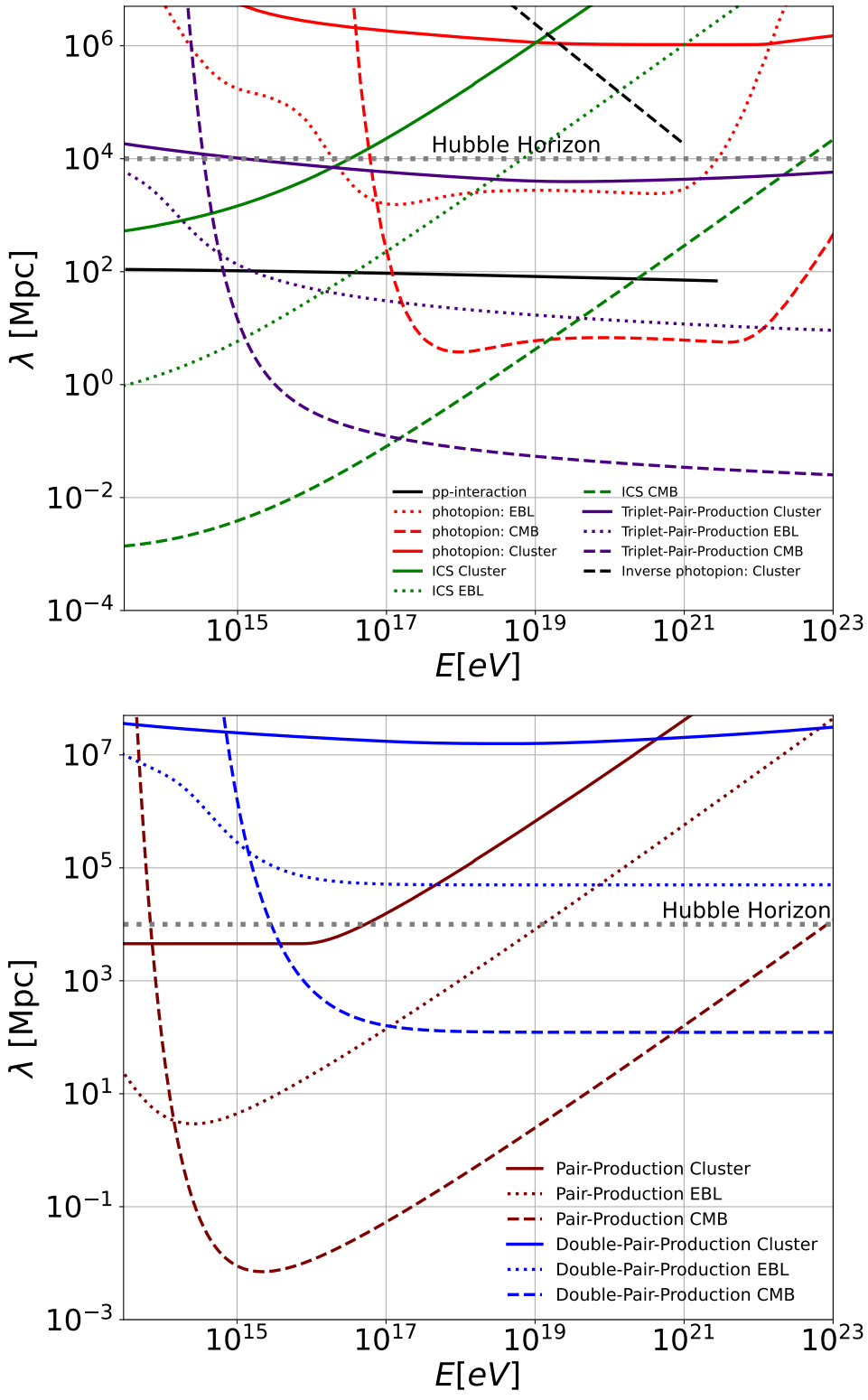

Figure 3.6: MFP of different interactions of CRs with the background photon fields, considering a cluster of mass $10^{15}\ M_{\odot}$. Panel (a) shows the MFP of ICS, photopion production and triplet pair production for CMB, an EBL model and the local Bremsstrahlung photon field. Panel (b) shows the MFP of single and double pair production for the same background photon fields.

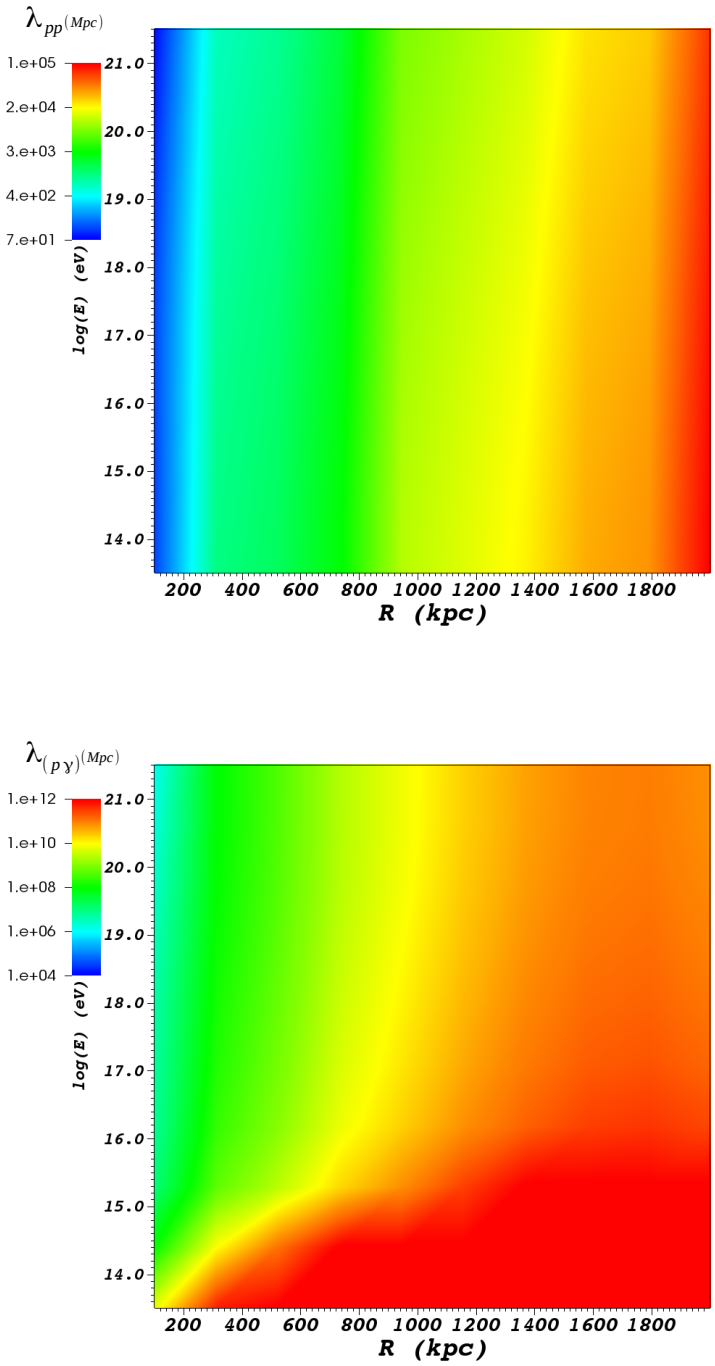

Figure 3.7: This diagram shows the MFP for proton-proton interactions in panel (a) and photo pion production in panel (b) for the Bremsstrahlung photon field inside a cluster of mass 10^{15} $M_{\odot}$. It can be seen from panel (b) that the CRs interactions with Bremsstrahlung radiation is very unlikely to occur because the MFP is larger than the size of the Universe.

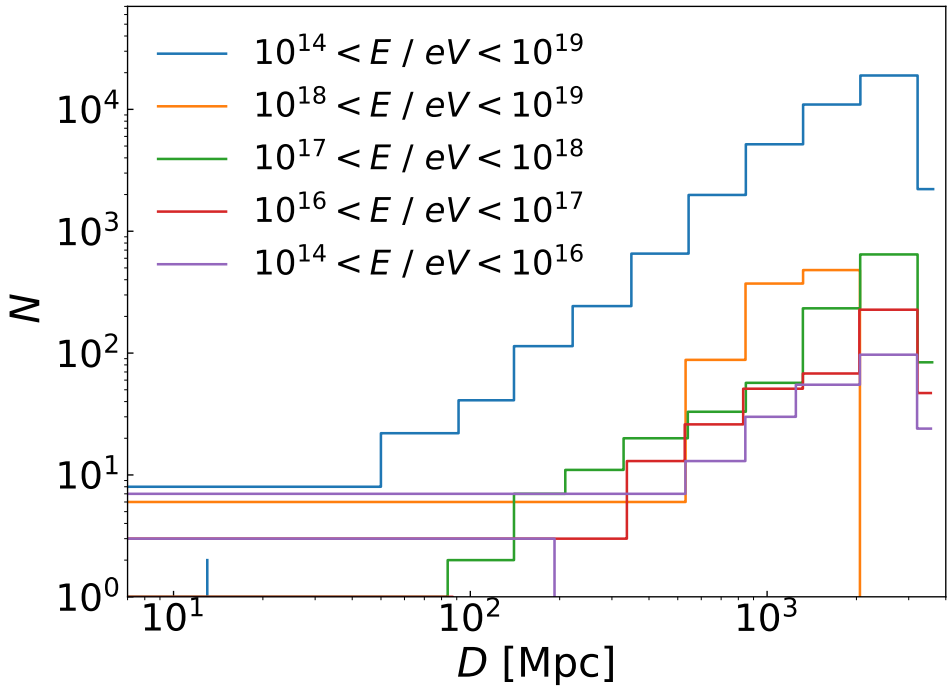

Figure 3.8: This figure shows the distribution of the total trajectory length of CRs inside a cluster of mass 10^{15} $M_\odot$ as a function of their energy bins. The length of trajectories of CRs inside clusters is comparable with the MFPs (Hussain et al., 2021).

3.5 CR Propagation Regimes in Clusters of Galaxies

Propagation of CRs in clusters of galaxies can be diffusive or semi-diffusive, depending on the Larmor radius ($r_{\rm L} = 1.08 E_{15}/ZB_{\mu\rm G}$ pc) (e.g., Hillas, 1984) of the particles and the magnetic field of the ICM, where Z is the atomic number. The diffusive regime corresponds to $r_{\rm L} \ll R_{\rm cluster}$, and the semi-diffusive is for $r_{\rm L} \gtrsim R_{\rm cluster}$, wherein $R_{\rm cluster}$ is the radius of the cluster, typically $\sim$ 1Mpc. Because $B \sim \mu$G, for the CR energy range of interest ($10^{14} - 10^{19}$ eV), $r_{\rm L} < R_{\rm cluster}$. So, for high-energy CRs ($> 10^{15}$ eV) we are in a diffusive or semi-diffusive regime. CRs in this energy range would be confined completely by the magnetic field of the clusters for a time comparable to the Hubble time (e.g. Wiener et al., 2013; Brunetti and Vazza, 2020; Nishiwaki et al., 2021). For instance, a CR with energy $\sim 10^{17}$ eV in a cluster of mass $\sim 10^{14}$ $M_\odot$ with central magnetic field strength $\sim \mu$G has $r_{\rm L} \sim 0.1$ kpc much smaller than the size of the cluster ($\sim$ 1 Mpc) and the trajectory length of this CRs inside the cluster is $\sim 10^3$ Mpc. The confinement time for this CR can be calculated as $t_{\rm con} \sim 1000$ Mpc$/c$ $\sim t_{\rm H}$ (e.g. Hussain et al., 2019). CRs with Larmor radius larger or comparable to the $R_{cluster}$, which is the case for CRs with $\gtrsim 10^{19}$ eV, will have a

ballistic propagation and will not be confined in a cluster. The flux of CRs that can escape a cluster depends on its mass and magnetic-field profile, with the latter directly correlated with the density distribution, being larger in denser regions.

3.6 Diffusion Parameter and CR Propagation in the ICM

We selected clusters of different masses from the 3D-MHD cosmological simulation (Figs. 2.4 and 2.5). Using CRPropa 3, we injected CRs at the center of these clusters with energy in the range $10^{15} - 10^{19}$ eV and propagated them through different distances 100 kpc, 500 kpc, 1 Mpc etc. Their cascading and energy losses due to interaction with the environment, were computed as described in the previous sections.

In Appendix B, for comparison and testing of the numerical methods here employed, we present a complementary study where we explored the propagation of CRs in a much simpler background configuration with uniform distribution of radiation and a turbulent magnetic field with a Kolmogorov spectrum (e.g., Kolmogorov, 1991; Boldyrev and Cattaneo, 2004; Bovino et al., 2013).

Fig. 3.9 illustrates the propagation of two particles with energy of 10 PeV (thick line), 500 PeV (thin line). One can see from the Fig. 3.9, that the trajectory of the low energy CR is diffusive and that of high-energy is more ballistic.

The spectrum of CRs from the center of the simulated Virgo cluster (see Fig. 2.3 of Chapter 2), collected at the edge of the cluster, is shown in Fig. 3.10. This simulation was primarily designed to test the influence of the diffusion parameter on the CR distribution. We use different values of this parameter $\epsilon = \kappa_\perp \ / \ \kappa_\parallel$, where $k_\parallel$ is the diffusion coefficient parallel and, $k_\perp$ is the diffusion perpendicular to the background magnetic field. The perpendicular diffusion coefficients is proportional to the parallel diffusion coefficient and rather uncertain (see e.g., Le Roux et al., 1999; Wiener et al., 2013; Peretti et al., 2019, 2020, 2021; Xu and Lazarian, 2020; Lazarian and Xu, 2021). Following Strong and Moskalenko (1998); Merten et al. (2017), the parallel diffusion coefficient can be written as:

$$\kappa_\parallel = A(\epsilon)\kappa_0 \Big(\frac{\rho}{4 \times 10^9 \text{ V}}\Big)^\alpha, \tag{3.39}$$

where ρ is the rigidity of the CR which is defined as $\rho = r_\text{L} Bc$ (unit is in Volt), B is the

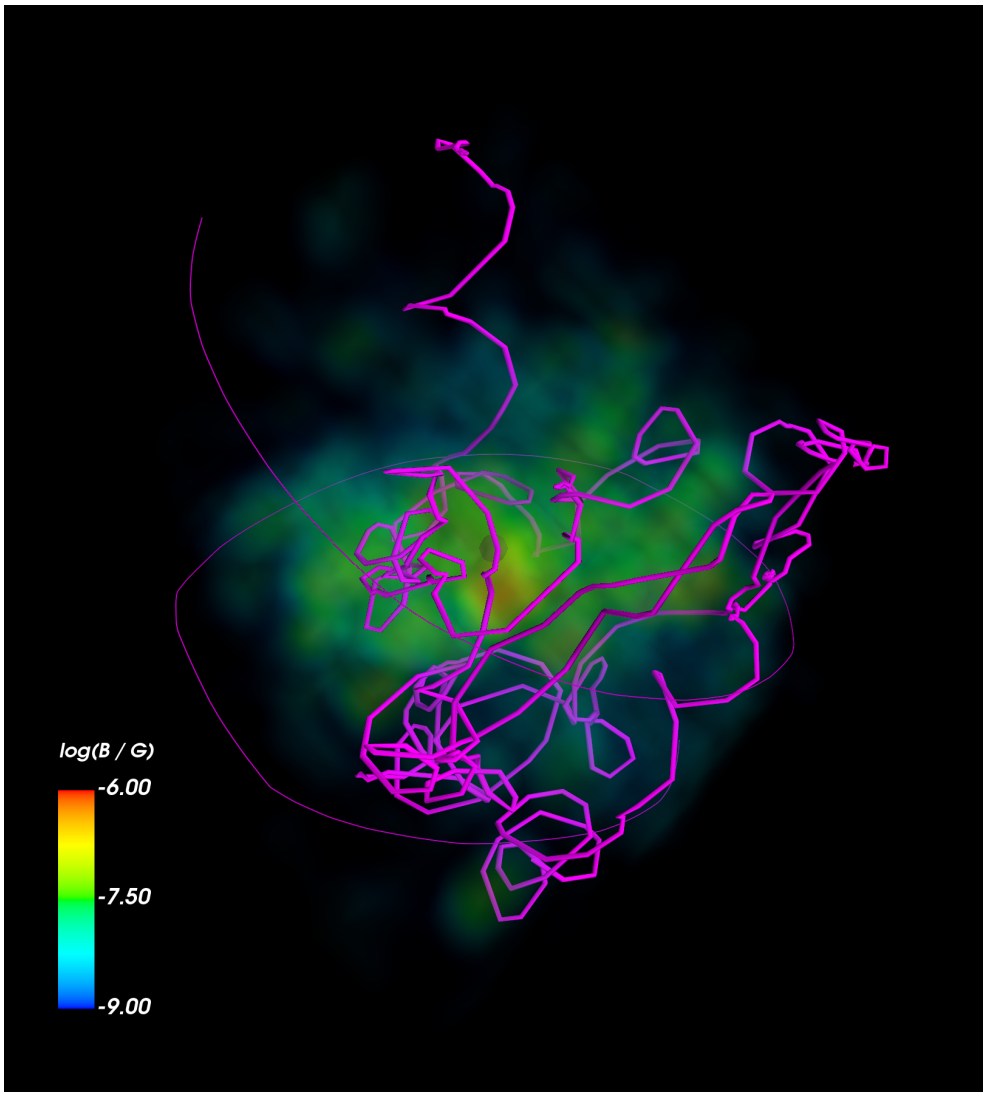

Figure 3.9: Trajectories of CRs through a cluster of mass $\sim 10^{15}$ $M_{\odot}$ selected from our background simulation. The thick line corresponds to a CR with energy of 10 PeV, and the thin line to a CR with energy 500 PeV (Hussain et al., 2022).

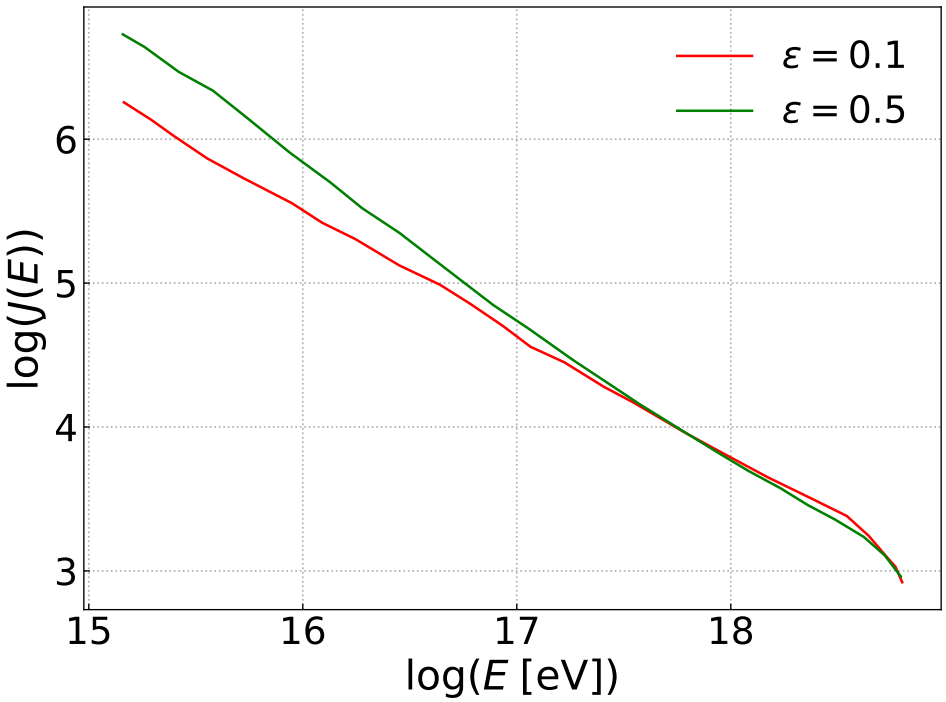

Figure 3.10: CR spectrum (in code units) observed at 2 Mpc away from the center of a simulated cluster that characterizes the Virgo cluster (Fig. 2.3 of Chapter 2). The spectrum is shown for two different values of the diffusion parameter $\epsilon = \kappa_\perp/\kappa_\parallel$.

magnetic field and c is the light speed, $\kappa_0 = 6.1 \times 10^{24}$ m^2/s and $\alpha = 0.3$ which is chosen to fit the observational data of CRs (Heinbach and Simon, 1995). $A(\epsilon) = 1.02/(1 + 2\epsilon)$ is a normalization constant which is derived in such a way that the trace of the diffusion tensor remains constant for different values of the diffusion parameter ϵ (Merten et al., 2017). The energy loss time scale is largly dependent on the trace of the diffusion tensor and thus of the parameter ϵ.

The difference in the diffusion parameter ϵ is clearly presented in Fig. 3.10. We injected the CRs at the center of the simulated Virgo cluster and collected them at the edge ($\sim$ 2 Mpc). We considered their interactions with the magnetic field and photon fields during their propagation inside the cluster. It is observed that a larger parallel diffusion coefficient $\kappa_\parallel > \kappa_\perp$ ($\epsilon \leq 0.1$) prevents a faster escape of smaller energy CRs from the cluster environment and vice versa.

For the derivation of the flux of neutrinos and gamma-rays that we will present in the next Chapters 4 and 5, we consider all the relevant losses. We used the SDE approach for the propagation of particles in the clusters and fixed the value of diffusion parameter

$\epsilon = 0.1$. This is essentially an approximation to make clear that the perpendicular diffusion coefficient is smaller than the parallel (with respect to the particle momentum), such that quasi-linear theory (QLT) [7] can be applied (Blandford and Eichler, 1987; Wiener et al., 2013). By fixing the diffusion parameter, we are assuming a preferred orientation for the magnetic field in each cell. However, by averaging over large number of particles, this preference is washed out especially at energy > 10 PeV, because at higher energies the resulting parallel diffusion coefficient has very weak dependence on the CR energy (Xu and Lazarian, 2020). In the limit of large statistics the results should converge, regardless of the diffusion parameter as one can see for energy > 10 PeV from Fig. 3.10. Note that we obtain the magnetic field configuration from the MHD simulation and implement its intensity and direction in each position in the CRPropa 3. Indeed, to study the propagation using the SDE approach (QLT) we have to specify the direction of the magnetic field.

We further notice that, According to the QLT, the Mach number M_A [8] of the turbulent plasma of the ICM is $\sim 1 - 5$ (Blandford and Eichler, 1987). In such a trans-Alfvenic or super-Alfvenic turbulent environment as the ICM ($M_A \gtrsim 1$), where the dynamical effect of the magnetic field is less dominant, the transport of the CR can be considered approximately isotropic $\kappa_{\parallel} \sim \kappa_{\perp}$ (Xu and Yan, 2013). Nevertheless, the relation between parallel and perpendicular diffusion coefficient in the ICM is yet rather uncertain and debatable. This is one of our future topics to explore further, i.e., the diffusion of CRs in the ICM.

3.7 Summary of this Chapter

In this Chapter, we described briefly the code and the methodology we employ in this work for calculation of CR propagation using the CRPropa 3 Monte Carlo code. The trajectory of CRs can be diffusive or ballistic depending on their energy and the source

[7] QLT is the simplest theory of cosmic ray propagation and diffusion in plasma turbulence and instability saturation. It is the most applied approach to determine spatial diffusion coefficients and other transport parameters in the turbulent plasma. It describes the slow evolution of the turbulent field and its relaxation that leads to the marginally stable states. The QLT is only applicable if the turbulence in the magnetic field is very small in comparison to the mean field strength (Schlickeiser and Miller, 1998; Schlickeiser, 2011). This approximation is comparable to a first-order perturbation theory (Schlickeiser, 2011)).

[8] where $M_A = V_L/V_A$, where V_L is the turbulent velocity of the plasma, and V_A is the Alfven velocity.

which emits them. As we are studying the ICM, therefore, the trajectories of CRs with energy $< 10^{19}$eV are mostly diffusive.

We have also described all the relevant CR energy loss processes including photopion production, photodisintegration, nuclear decay, proton-proton (pp) interactions, and adiabatic losses. To see the importance of these processes we compared their MFPs in the ICM. We have found that in the ICM high-energy photons and neutrinos can be produced either through inelastic proton-proton collisions and subsequent neutral-pion decay, or by processes involving energetic electron-positron pairs produced as secondaries of the hadronic interactions. Moreover, interactions of CRs with the Bremsstrahlung photon field are important only in the central region of the clusters of galaxies to produce secondary particles. The interactions with the CMB and EBL photon fields are more relevant, being those with the CMB dominant.

The effect of the diffusion parameter on the spectrum of CRs in the ICM was also studied. We found that a large parallel diffusion coefficient is more suitable to study the transport of CRs inside clusters as suggested by the previous studies (see e.g., Blandford and Eichler, 1987; Wiener et al., 2013, for review). This preliminary study of CR propagation in an individual cluster has provided important information and the basis for the more general study that followed it, where we considered CR propagation over the entire distribution of simulated clusters of galaxies, over cosmological times, in order to derive the integrated flux of neutrinos and gamma-rays. For the computation of these fluxes in Chapters 4 and 5, we will focus on the propagation of CRs with proton composition only, as this is the most abundant component in the ICM and IGM (e.g., Kotera et al., 2009; Aab et al., 2017, 2016; Fang and Olinto, 2016; Aaboud et al., 2016; Fang and Murase, 2018; Aab et al., 2020; Sokolsky and Thomson, 2007, 2020). Also, the Larmor radius of heavy nuclei is comparatively smaller than that of protons (Hillas, 1984), therefore, protons escape more easily from their host galaxies into the IGM. Thus, it is reasonable to assume that they also dominate the IGM compared to other species. At higher energies $\gtrsim 10^{18}$ eV, heavy nuclei might be dominant because the acceleration of CRs is rigidity-dependent (e.g., Unger et al., 2015; Sigl, 2017; Mollerach and Roulet, 2020; Tjus and Merten, 2020).

In next Chapters 4 and 5, we will study the transport of CRs in the ICM using the SDE approach by assuming a large parallel diffusion coefficient ($\epsilon = 0.1$). Furthermore, we will show the results of the implementation of the interaction processes (discussed above)

during the CRs propagation into the ICM and IGM, in order to compute the fluxes of gamma-rays and neutrinos with the CRPropa 3 code.

Chapter 4

Production of High Energy Neutrinos by Galaxy Clusters

In this Chapter, we study the production of high-energy $\gtrsim$ TeV neutrinos by clusters of galaxies. There are previous studies that have estimated the flux of neutrinos from clusters of galaxies (e.g., Zandanel et al., 2015; Fang and Olinto, 2016; Fang and Murase, 2018; Nishiwaki et al., 2021). However, in all of them the ICM and IGM are over simplified. In most cases it is considered spherical symmetric profiles of the density and magnetic field. Here we employ the most detailed simulations to date of three-dimensional particle transport in cosmological MHD environments in order to obtain the diffuse flux of neutrinos from clusters of galaxies (see also Chapter 5 for the derivation of the diffuse gamma-ray flux). The results of this Chapter have been published in Hussain et al. (2021).

4.1 Setup for the Calculations and Basic Assumptions

The background MHD simulations of the galaxy clusters presented in Chapter 2 (see Fig. 2.1 - 2.5), provide the magnetic and density field configuration for galaxy clusters with mass in the interval $10^{12} \lesssim M/M_{\odot} < 10^{16}$, in the redshift range $z \lesssim 5.0$. Using these background fields along with the Bremsstrahlung, CMB, and EBL photon fields described in Section 3.2, we computed the propagation and total flux of CRs with all relevant interactions during the propagation, namely, photopion production, Bethe-Heitler pair production, electromagnetic pair-production (single, double and triplet), nuclear decay, photo-disintegration, inverse-Compton, adiabatic and synchrotron losses (see Section 3.3 and 3.4). Regarding the interaction of CRs in the ICM with the background photon fields, we found that the EBL is dominant at infrared and optical, but at X-rays the

Bremsstrahlung field is more important (see Chapter 3, Fig. 3.6)

To study the propagation of CRs in the diffuse ICM, we used the transport Equation as implemented in CRPropa 3 (Section 3.1.1). The diffusion parameter considered in these simulations is $\epsilon = 0.1$, see Chapter 3 for discussion (see also Blandford and Eichler, 1987; Wiener et al., 2013). We inject CRs isotropically with a power-law energy distribution with spectral index α and exponential cut-off energy $E_{\rm max}$ which follows the relation $dN_{{\rm CR},E}/dE \propto E_i^{-\alpha} \exp(-E_i/E_{\rm max})$ (Section 3.1.1). We take different values for $\alpha \simeq 1.5-2.7$, and for $E_{\rm max} = (5\times10^{15} - 10^{18})$ eV which are compatible with e.g., Brunetti and Jones (2014); Fang and Olinto (2016); Brunetti et al. (2017); Hussain et al. (2019).

As stressed in Chapter 2, the lower and upper limits of the mass of the galaxy clusters are taken to be 10^{12} $M_\odot$ and 5×10^{15} $M_\odot$, respectively. This is because for $10^{14} \lesssim E/{\rm eV} \lesssim 10^{19}$, clusters with mass $M < 10^{12}$ $M_\odot$ barely contribute to the total flux of neutrinos, due to low gas density, while there are few clusters with $M \gtrsim 10^{15}$ $M_\odot$ at high redshifts ($z > 1.0$) (Komatsu et al., 2009; Ade et al., 2014).

The amount of power of the clusters that goes into CR production is left as a free parameter to be regulated by the observations. We here assume that about $(0.5-3)\%$ of the cluster luminosity, which is dominated by the X-ray luminosity, is available for particle acceleration (e.g. Gonzalez et al., 2013; Brunetti and Jones, 2014; Fang and Olinto, 2016; Brunetti and Vazza, 2020, for reviews).

We did not consider the feedback from active galactic nuclei (AGN) or star formation rate (SFR) in our background cosmological simulations (as performed e.g. in Barai and de Gouveia Dal Pino, 2019; Hopkins et al., 2021). AGN are believed to be the most promising CR accelerators inside clusters of galaxies and star-forming galaxies contain many supernova remnants that can also accelerate CRs up to very-high energies ($E \gtrsim$ 100 PeV) (He et al., 2013). AGN are more powerful and more numerous at higher redshifts (e.g., Hasinger et al., 2005; Khiali and de Gouveia Dal Pino, 2016; D'Amato et al., 2020), and their luminosity density evolves more strongly for $z \gtrsim 1$. Also, supernovae are more common at high redshifts (He et al., 2013; Moriya et al., 2019). Therefore, it is reasonable to expect that, if high energy cosmic ray (HECR) sources have a cosmological evolution similar to AGN or following the star-formation rate (SFR), then the flux of neutrinos may be higher at high redshifts due to the larger CR output from these objects.

For the evolution of AGN sources and SFR we consider the following parametrization

(Hopkins and Beacom, 2006; Heinze et al., 2016; Yüksel et al., 2008; Wang et al., 2011; Gelmini et al., 2012; Alves Batista et al., 2019):

$$\psi_{\rm SFR}(z) = \frac{1}{B}\begin{cases}(1+z)^{3.4} & \text{if } z<1,\\ (1+z)^{-0.3} & \text{if } 1<z<4,\\ (1+z)^{-3.5} & \text{if } z>4,\end{cases} \tag{4.1}$$

$$\psi_{\rm AGN}(z) = \frac{(1+z)^m}{A}\begin{cases}(1+z)^{3.44} & \text{if } z<0.97,\\ 10^{1.09}(1+z)^{-0.26} & \text{if } 0.97<z<4.48,\\ 10^{6.66}(1+z)^{-7.8} & \text{if } z>4.48,\end{cases} \tag{4.2}$$

where $A = 360.6$ and $B = 6.66$ are normalization constants in Equations (4.2) and (4.1), respectively. For AGN evolution $\psi_{AGN}(z) \propto (1+z)^5$, for low redshift $z < 1$ (Gelmini et al., 2012; Alves Batista et al., 2019) and also according to (Gelmini et al., 2012; Heinze et al., 2016), in Equation (4.2), $m > 1.5$ for AGN, so we consider $m = 1.7$. Typically, the luminosity of AGNs ranges from 10^{42} to 10^{47} erg/s and their evolution depends on their luminosities. The AGNs with luminosity $\sim 10^{44}-10^{46}$ erg/s are more important as they are more numerous and believed to be able to accelerate particles to ultra-high energies (e.g. Waxman, 2004; Khiali and de Gouveia Dal Pino, 2016). AGNs with luminosities greater than 10^{46} erg/s are less numerous (Hasinger et al., 2005) and their evolution function $\psi_{\rm AGN}(z)$ is different from Equation (4.2). For no source evolution we have $\psi(z) = 1$.

The total flux of CRs is estimated from the entire population of clusters. The number of clusters per mass interval dN/dM at redshift z is presented in Section 2.2, which was obtained from our cosmological simulations. It is related to the flux through:

$$E^2\Phi(E) = \int_{z_{\rm min}}^{z_{\rm max}} dz \int_{M_{\rm min}}^{M_{\rm max}} dM \frac{dN}{dM}\, E^2 \frac{d\dot{N}(E/(1+z), M, z)}{dE}\left(\frac{\psi_{\rm ev}(z)}{4\pi d_L^2(z)}\right) \tag{4.3}$$

where $\psi_{\rm ev}(z)$ stands for $\psi_{\rm SFR}(z)$ and $\psi_{\rm AGN}(z)$, $\dot{N}$ is the number of CRs per time interval dt with energies between E and $E + dE$ that reaches the observer. The quantity $E^2\, d\dot{N}/dE$ in Equation (4.3) is the power of CRs calculated from our propagation simulation and is several orders of magnitude smaller than the luminosity of observed clusters (e.g., Brunetti and Jones, 2014).

In order to convert the code units of the CR simulation to physical units, we have used a normalization factor (Norm). To calculate Norm, we first evaluate the X-ray luminosity

of the cluster using the empirical relation $L_{\rm X} \propto f_g^2\ M_{\rm vir}$ (e.g., Schneider, 2014), where $f_g = M_g/M_{\rm vir}$ denotes the gas mass (M_g) fraction with respect to the total mass of the cluster within the Virial radius ($M_{\rm vir}$) and then, since we are assuming that $(0.5-3)\%$ of this luminosity goes into CRs, this implies that Norm $\sim (0.5-3)\ \%\ L_{\rm X}/L_{\rm CRsim}$ and $L_{\rm CRsim}$ is the luminosity of the simulated CRs. Therefore, the CR power that reaches the observer (at the Earth) is $\sim E^2\ d\dot{N}/dE \times$ Norm. In Equation (4.3) d_L is the luminosity distance, given by:

$$d_L = (1+z)\frac{c}{H_0}\int_0^z \frac{dz'}{E(z')}, \tag{4.4}$$

with

$$E(z) = \sqrt{\Omega_m(1+z)^3+\Omega_\Lambda} = \frac{H(z)}{H_0}, \tag{4.5}$$

where the Hubble constant, as well as the matter (Ω_m) and dark-energy (Ω_Λ) densities which are described in Chapter 2, assuming a flat ΛCDM universe.

4.2 CR Flux from the Galaxy Clusters

We selected different injection points inside the clusters of different masses in order to study the spectral dependence with the position, which may correspond to different scenarios of acceleration of CRs. For instance, the larger concentration of galaxies near the center must favor more efficient acceleration, but compressed regions by shocks in the outskirts may also accelerate CRs. The schematic diagram of the simulation of CRs propagation is shown in Fig. 4.1. CRs are injected at three different positions within each selected cluster denoted by $R_{\rm Offset}$. The spectra of CRs have been collected by an observer in a sphere of 2 Mpc radius ($R_{\rm Obs}$), centred at the cluster, with a redshift window ($-0.1 \leq z \leq 0.1$) for all the injection points of CRs. All-flavour neutrino fluxes are also computed at the same observer (see Section 4.3 below).

The spectrum of CRs obtained from our simulations is shown in Figs. 4.2 and 4.3. Its dependence on the position where the CR source is located within the cluster for $z = 0.01$ is shown for three clusters of different masses in Fig. 4.2. Particles injected at 1 Mpc distance away from the clusters center can leave them in short time, with almost no interaction, as both the magnetic field and the gas number density are very low compared to the central regions. On the other hand, CRs injected at the center or at 300 kpc away from the cluster

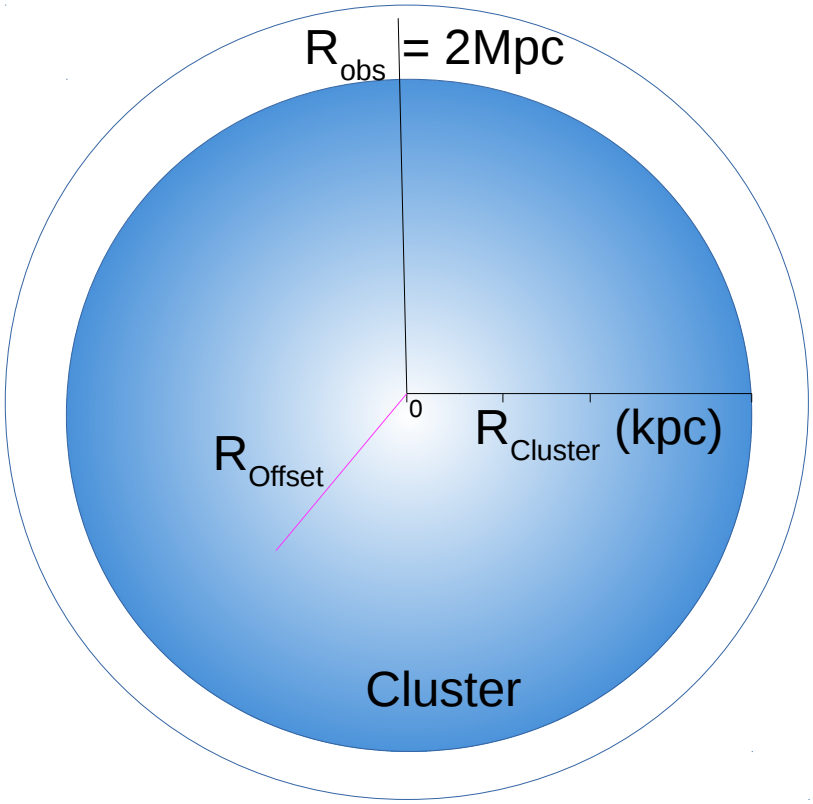

Figure 4.1: Scheme of the CR simulation geometry. They are injected at three different positions inside each cluster represented by $R_{\rm Offset}$, and $R_{\rm Obs}$ is the radius of the observer (Hussain et al., 2021).

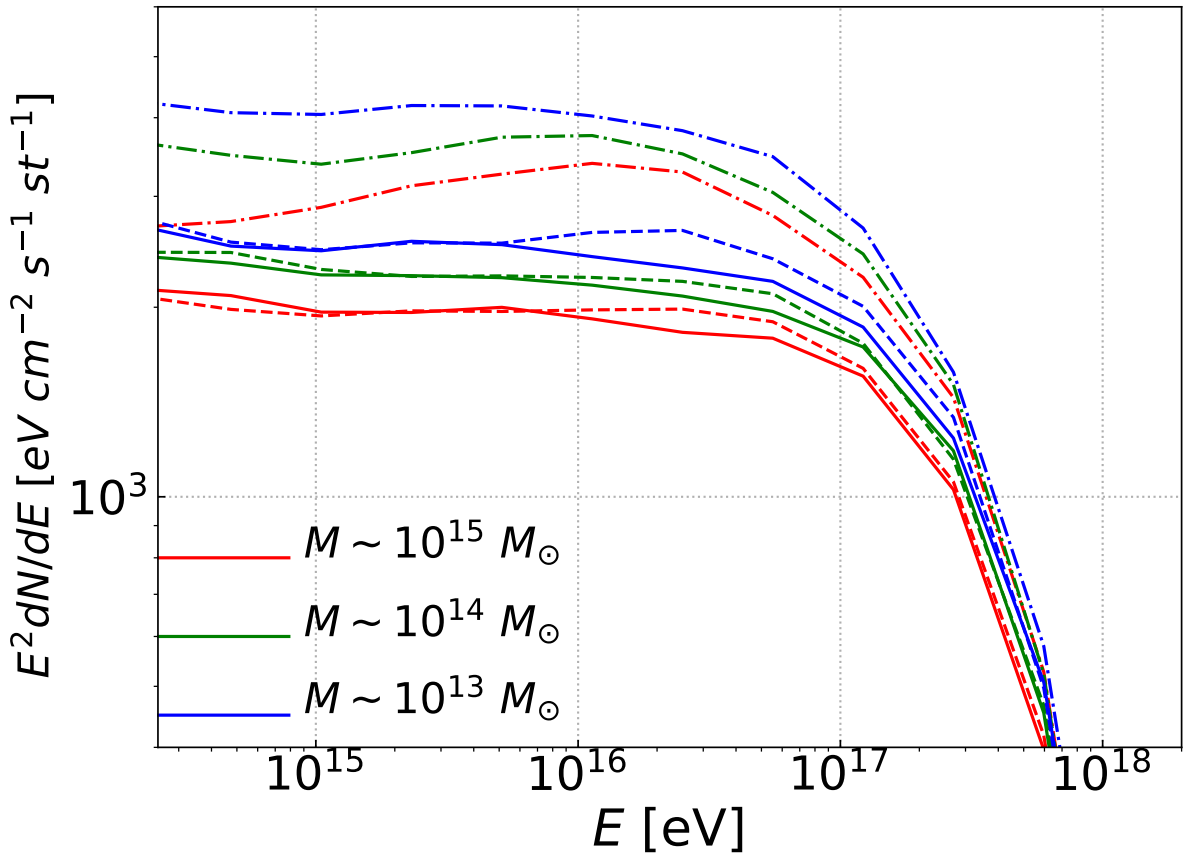

Figure 4.2: This figure shows the CR flux of individual clusters of distinct masses, $M \sim 10^{15}$ (red); 10^{14} (green); and $M \sim 10^{13}\ M_\odot$ (blue color) at redshift $z \sim 0$. The sources of CRs are located at the center of the cluster (solid), at 300 kpc (dashed), and at 1 Mpc (dash-dotted lines) away from the centre. The flux is computed at the edge of the clusters. The spectral parameters are $\alpha = 2$ and $E_{\rm max} = 5 \times 10^{17}$ eV, and it is assumed that 2% of the luminosity of the clusters is converted into CRs (Hussain et al., 2021).

center can be easily deflected by the magnetic field and trapped in dense regions. This explains the higher CR flux for the injection point at 1 Mpc in Fig. 4.2. Also, because the confinement of CRs in the central regions of the clusters is comparable to a Hubble time, and because of the value of the MFP for the relevant interactions (Section 3.4), the production of secondary particles including neutrinos and gamma rays in the clusters is substantial, as we will see in Section 4.3. Fig. 4.2 also shows that the CR flux is larger for smaller cluster mass (see justification for that in Section 4.4.)

In Fig. 4.3 we show the CR spectrum of all the clusters at different redshifts integrated up to the Earth. Although the spectra in this diagram have been integrated up to the Earth, we have not considered any interactions of the CRs with the background photon and magnetic fields during their propagation from the edge of the clusters to the Earth.

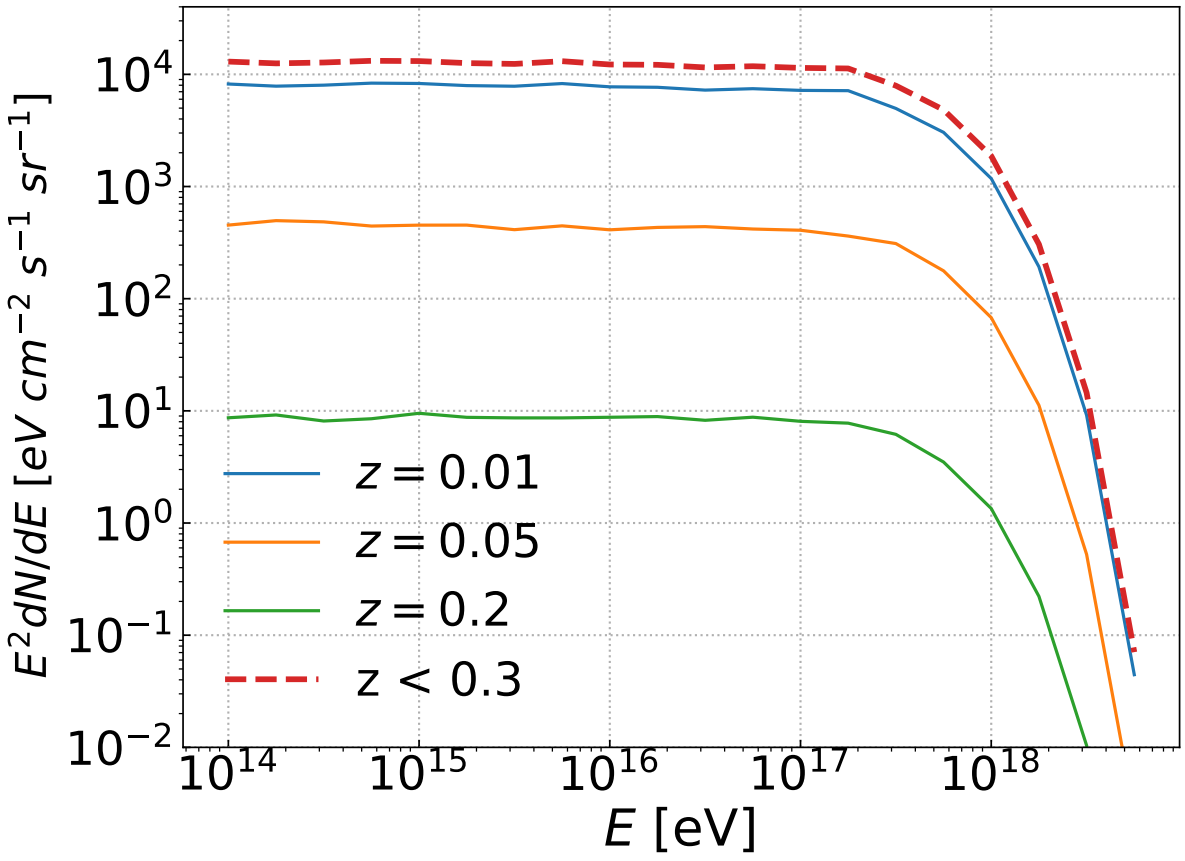

Figure 4.3: This figure shows the total CR flux (at the Earth distance) from all the clusters distributed in different redshifts: $z \sim 0$ (blue); $z = 0.05$ (orange); $z = 0.2$ (green). The total CRs flux for the redshift range $z \leq 0.3$ is given by the red dotted line (Hussain et al., 2021).

Though not quantitatively realistic, it provides important qualitative information. One obvious result is that most of the contribution in the CR flux comes from clusters at low redshifts. Moreover, there is a significant suppression in the flux of CRs at $\gtrsim 10^{17}$ eV, which indicates the trapping of lower-energy CRs within the clusters (Alves Batista et al., 2018; Hussain et al., 2019), as discussed in Chapter 3.

4.3 Flux of Neutrinos

To calculate the neutrino flux, we integrate a relation similar to Equation (4.3) for neutrino species, and the procedure is the same as described in Section 4.1. In order to calculate the flux of neutrinos corresponding to injected CRs with a given power-law spectrum with spectral index α, $dN_{\rm CR}/dE \propto E_i^{-\alpha} \exp\{-E_i/E_{\rm max}\}$, we can normalize the

spectrum as follows:

$$J(\alpha) = \frac{\ln(E_{\rm CR,\ max}/E_{\rm min})}{\int_{E_{\rm min}}^{E_{\rm CR,\ max}} E_i^{1-\alpha} \exp\left(-\frac{E_i}{E_{\rm max}}\right) dE} E_i^{1-\alpha} \exp\left(-\frac{E_i}{E_{\rm max}}\right) \tag{4.6}$$

Where, E_i is the injection energy of the simulated CRs, $E_{\rm max}$ is the exponential cut-off energy, and $E_{\rm CR,\ max}$ is the maximum injection energy of the CRs.

In general, neutrino production occurs mainly due to photopion production and pp-interactions. In Fig. 3.6 of Chapter 3, where the MFP for different interactions are depicted, we see that protons with energies $E < 10^{17}$ eV produce neutrinos principally due to pp-interactions, while for $E > 10^{17}$ eV, they produce neutrinos both, by pp-interactions and photopion process. We have seen also in Fig. 3.6 of Chapter 3 that the total trajectory length of CRs inside a cluster is comparable or larger than λ for these interactions and thus, neutrino production is inevitable.

In Fig. 4.4 we show the dependence of the neutrino flux with the position of the corresponding CR source within clusters of different masses. As in the case of the CR flux, it can be seen that there is less neutrino production for the injection position at 1 Mpc away from the center of the cluster. Furthermore, massive clusters produce more neutrinos than the light ones (see justification for this behaviour in Section 4.4). In Fig. 4.5 we present the redshift distribution of neutrinos as a function of their energy, observed at a distance of 2 Mpc away from the center of individual clusters with different masses. Most of the neutrinos are produced in the range $z \lesssim 0.3$.

In Figs. 4.6 and 4.7, we present the total flux of neutrinos from the whole population of clusters, as measured at Earth, integrated over the entire redshift range within the Hubble time (solid brown curve in the panels). In the upper panel of Fig. 4.6 and in Fig. 4.7, the injected CR spectrum is assumed to follow $E^{-1.5}$, with an exponential cut-off $E_{\rm max} = 5 \times 10^{16}$ eV. Also, we assumed in these cases that 0.5% of the kinetic energy of the clusters is converted to the CRs. Besides the total flux, this panel also shows the flux of neutrinos for several cluster mass intervals. The softening effect at higher energies is due to the shorter diffusion time of the CRs, and to the mass distribution of the clusters, as higher flux reflects lower population of massive clusters. In Fig. 4.7 we present the integrated flux in different redshift intervals and it can also be seen that the clusters at high redshift contribute less to the total flux of neutrinos. Those at $z > 1$ barely contribute to the flux

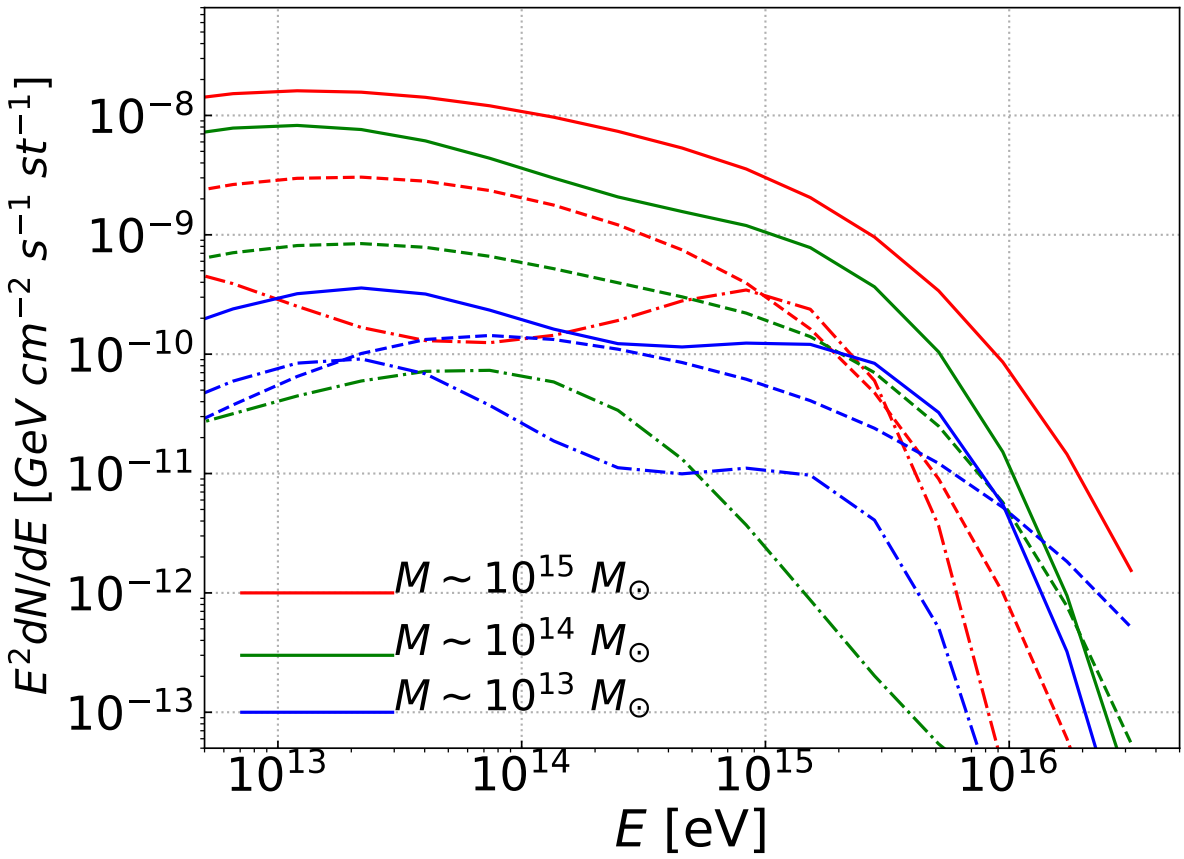

Figure 4.4: This figure shows the neutrino flux of individual clusters of distinct masses: $M \sim 10^{15}$ (red); 10^{14} (green) and 10^{13} $M_\odot$ (blue color). The CR sources are located at the center of the cluster (solid lines), at 300 kpc (dashed lines), and at 1 Mpc away from the center (dash-dotted lines). The flux is computed at the edge of clusters. The CR injection follows $dN/dE \propto E^{-2}$, $E_{\rm max} = 5 \times 10^{16}$ eV, and it is assumed that 2% of the luminosity of the clusters is converted to CRs (Hussain et al., 2021).

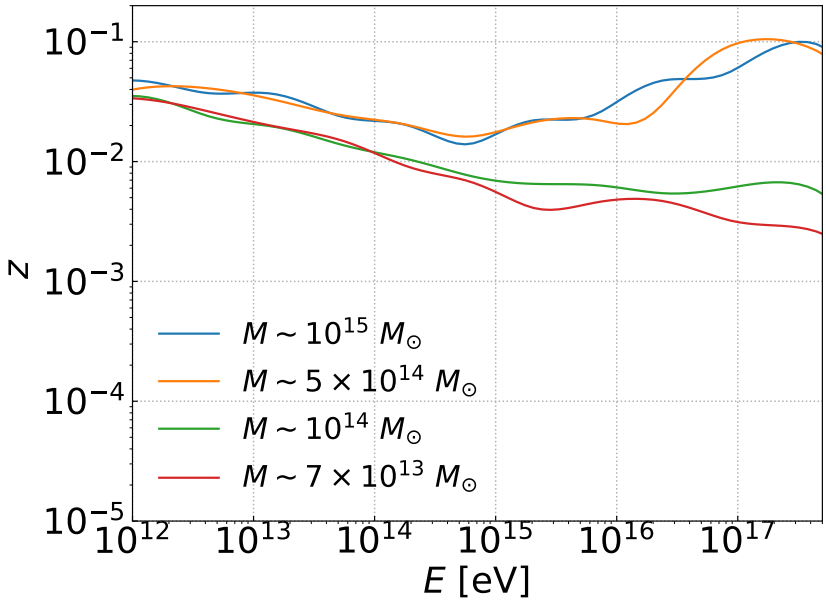

Figure 4.5: Redshift distribution of the neutrinos as a function of their energy, as observed at 2 Mpc away from the center of clusters with different masses (Hussain et al., 2021).

due to the low population of massive clusters and their large distances. Figs. 4.6 and 4.7 also compares our results with the IceCube observations. We see that for the assumed scenario for CRs injection in upper panel of Fig. 4.6 and in Fig. 4.7, they can reproduce the IceCube observations (Aartsen et al., 2015) for $E > 20$ TeV . In lower panel of Fig. 4.6, instead, we have assumed that 2% of the kinetic energy of the clusters is converted into CRs, with a CR energy power-law spectrum E^{-2}, with $E_{\rm max}$ following the dependence below with the cluster mass and magnetic field:

$$E_{\rm max} = 2.8 \times 10^{18} \left(\frac{M_{\rm cluster}}{10^{15} M_\odot}\right)^{2/3} \left(\frac{B_{\rm cluster}\ {\rm G}}{10^{-6}\ {\rm G}}\right)\ {\rm eV}, \tag{4.7}$$

which is similar to Fang and Olinto (2016). This condition is derived by Fang and Olinto (2016) comparing the time of acceleration of a CR to an energy $\sim 10^{18}$ eV in a magnetic field $\sim 10^{-6}$ G of a shock in the cluster, with the diffusive escape time from the acceleration region (see Inoue et al., 2007, for detail). In this scenario we find that the clusters contribution to the neutrino flux is smaller than IceCube measurements.

For all diagrams of Fig. 4.6 and 4.7, we also compare our results with those of Fang and Olinto (2016) (blue lines) who have performed the most detailed evaluation of the neutrino flux from galaxy clusters before our work (see more details about their model in Section 2.2). The total fluxes in both are similar, in general. Moreover, we see that

in both cases, the largest contribution to the flux of neutrinos comes from the cluster mass group $10^{14}\ M_{\odot} < M < 10^{15}\ M_{\odot}$. However, the contribution from the mass group $10^{12}\ M_{\odot} < M < 10^{14}\ M_{\odot}$ in our results is a factor twice larger than that of Fang and Olinto (2016), and smaller by the same factor for the mass group $M > 10^{15}\ M_{\odot}$, at energies $E > 0.01$ PeV (upper panel of Fig. 4.6).

A striking difference between the two results is that, according to Fang and Olinto (2016), the redshift range $0.3 \leq z \leq 1$ amounts for the largest contribution to neutrino production, but in our case the redshift range $0.01 \leq z \leq 0.3$ provides a more significant contribution (see Fig. 4.7). Besides, there is a difference of factor ~ 2 to ~ 3 between ours and their results at these redshift ranges. This difference may be due to the more simplified modeling of the background distribution of clusters in their case specially for the lower mass group ($10^{12}\ M_{\odot} < M < 10^{14}\ M_{\odot}$) at high redshifts ($z > 1$).

In Fig. 4.8, we present the total neutrino spectra calculated for different spectral indices of the injected CRs, while in Fig. 4.9 we show the total neutrino spectra calculated for several cut-off energies. In order to try to fit the observed IceCube data, we have considered a 3% conversion of the kinetic energy of the cluster into CRs in Figs. 4.8 - 4.11.

So far, we have computed the CR and neutrino fluxes from the clusters, considering no evolution function with redshift for both CR sources, AGN and SFR, i.e. we assumed $\psi_{\rm ev}(z) = 1$ in Equation (4.3). In Fig. 4.10, we have included these contributions and plotted the flux of neutrinos for the redshift ranges: $z < 0.3$, $0.3 < z < 1.0$, and $1.0 < z < 5.0$. The flux is obtained for spectral index $\alpha = 2$ and cutoff energy $E_{\rm max} = 5 \times 10^{17}$ eV.

Clusters can directly accelerate CRs through shocks, but any type of astrophysical object that can produce HECRs can also contribute to the diffuse neutrino flux. In the former case, the sources evolve only according to the background MHD simulations, dubbed here "no evolution", whereas in the latter some assumptions have to be made regarding the CR sources. In Fig. 4.10, we illustrate the impact of the source evolution. We consider, in addition to the case wherein sources do not evolve, SFR and AGN-like evolutions (see Equations 4.2 and 4.1 and accompanying discussion). Our results suggest that, while the neutrino fluxes for the AGN and the SFR evolutions are relatively close to each other, the case without evolution contributes slightly less to the total flux. We find that an AGN-type evolution enhances the diffuse neutrino flux at high redshifts ($z \gtrsim 1.5$) compared to scenarios wherein the sources evolve as the SFR (or without any evolution), while they

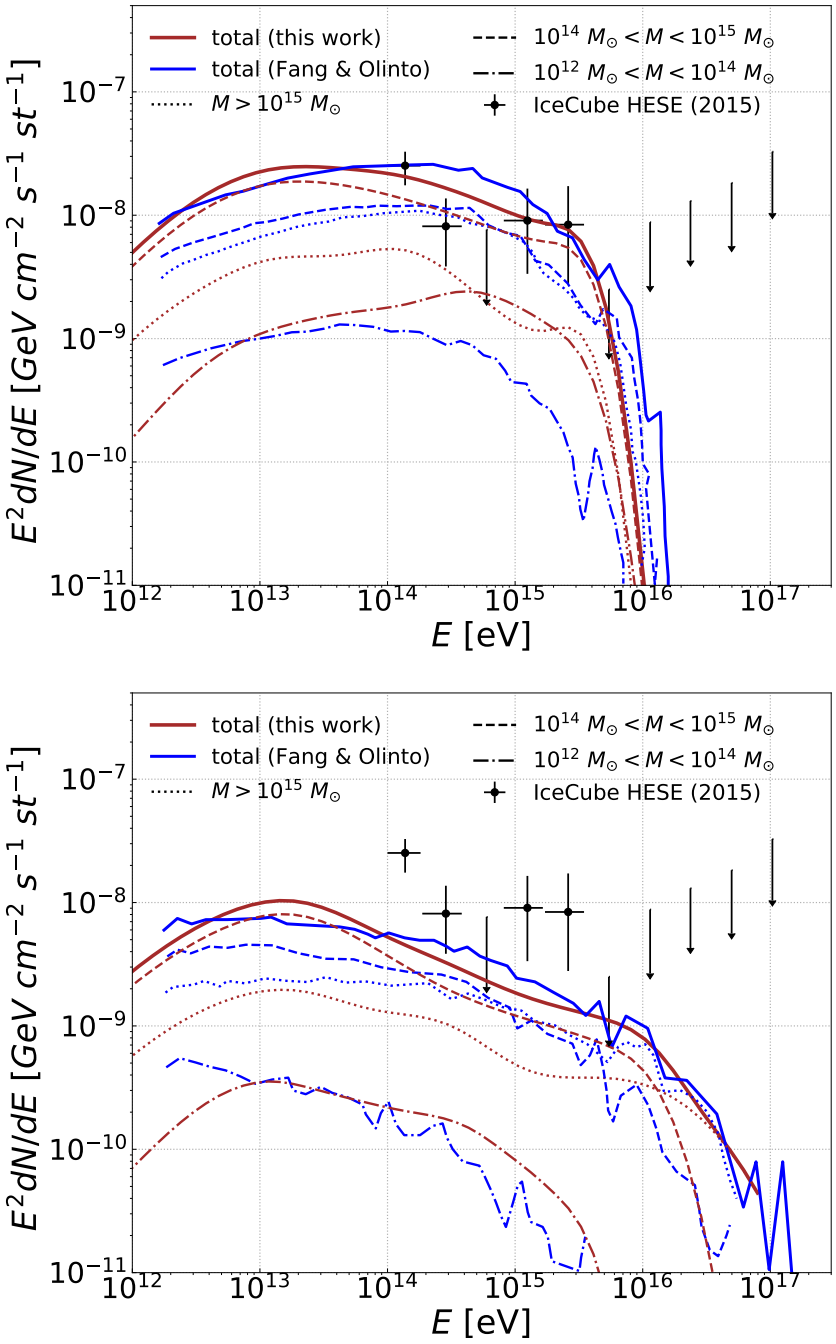

Figure 4.6: Neutrino spectrum at Earth obtained using our simulations (brown lines), compared with the IceCube data (markers) (Aartsen et al., 2015), and Fang and Olinto (2016) results (blue lines). The panels show the total flux integrated over all clusters and redshifts between $0.01 \leq z \leq 5$ (solid thick lines). The upper panel shows the neutrino spectra (thin blue and brown lines) for cluster mass ranges of: $10^{12}\ M_\odot < M < 10^{14}\ M_\odot$ (dash-dotted), $10^{14}\ M_\odot < M < 10^{15}\ M_\odot$ (dashed), and $M > 10^{15}\ M_\odot$ (dotted lines). The upper panel corresponds to the case with $\alpha = 1.5$ and $E_{\rm max} = 5 \times 10^{16}$ eV, whereas in the lower panel $\alpha = 2$ and $E_{\rm max}$ follows Equation 4.7. These diagrams do not include the redshift evolution of the CR sources, $\psi_{ev} = 1$ in Equation 4.3. It is assumed that 0.5% and 2% of the luminosity of the clusters is converted into CRs in the upper and lower panel, respectively (Hussain et al., 2021).

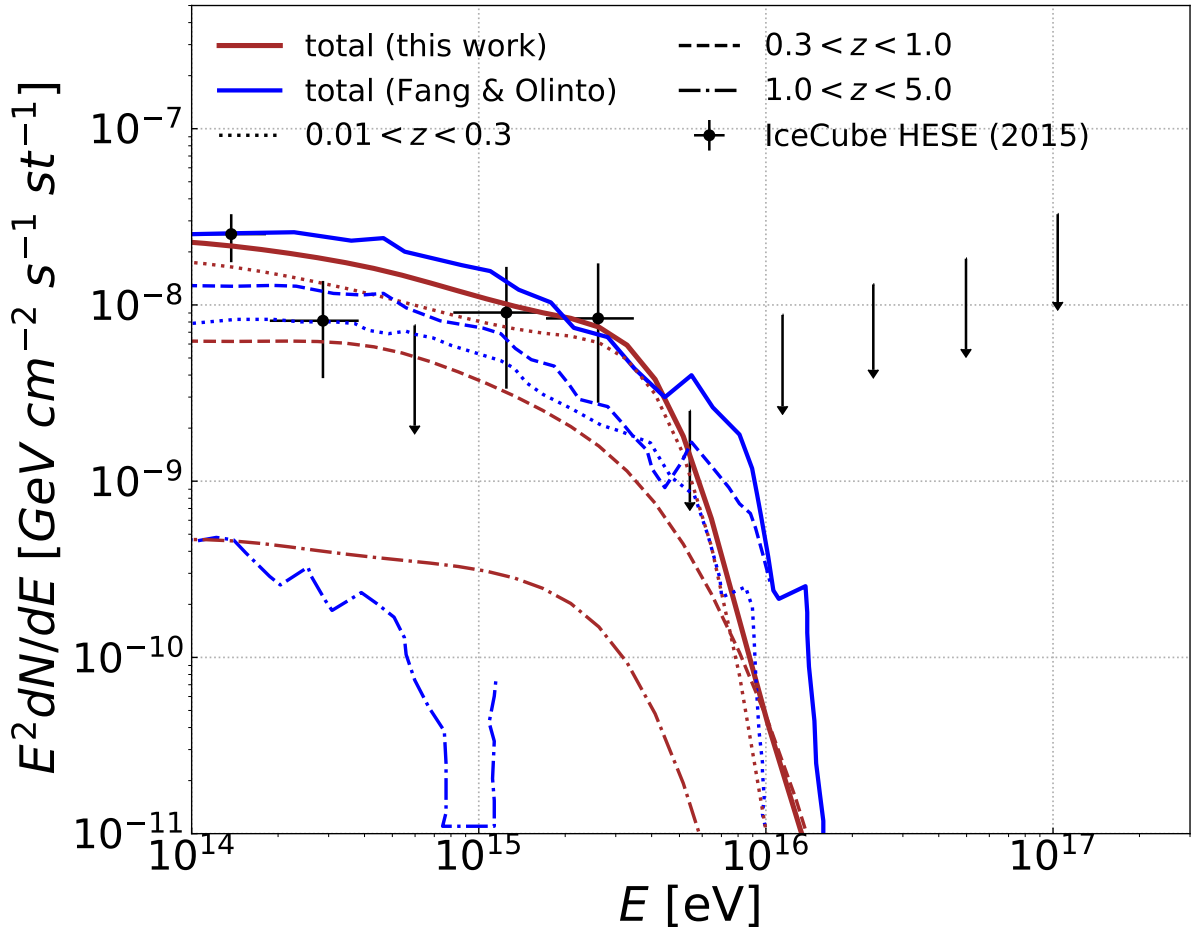

Figure 4.7: This figure shows the neutrino spectrum for different redshift ranges: $z < 0.3$ (dotted lines), $0.3 < z < 1.0$ (dashed), and $1.0 < z < 5.0$ (dash-dotted lines). The solid blue and brown lines correspond to the total spectrum in Fang and Olinto (2016), and in this work, respectively. The CR injection in this figure follows $dN/dE \propto E^{-1.5}$, and $E_{\rm max} = 5 \times 10^{16}$ eV. This figure does not include the redshift evolution of the CR sources, $\psi_{ev} = 1$ in Equation 4.3. It is assumed that 0.5% luminosity of the clusters is converted into CRs (Hussain et al., 2021).

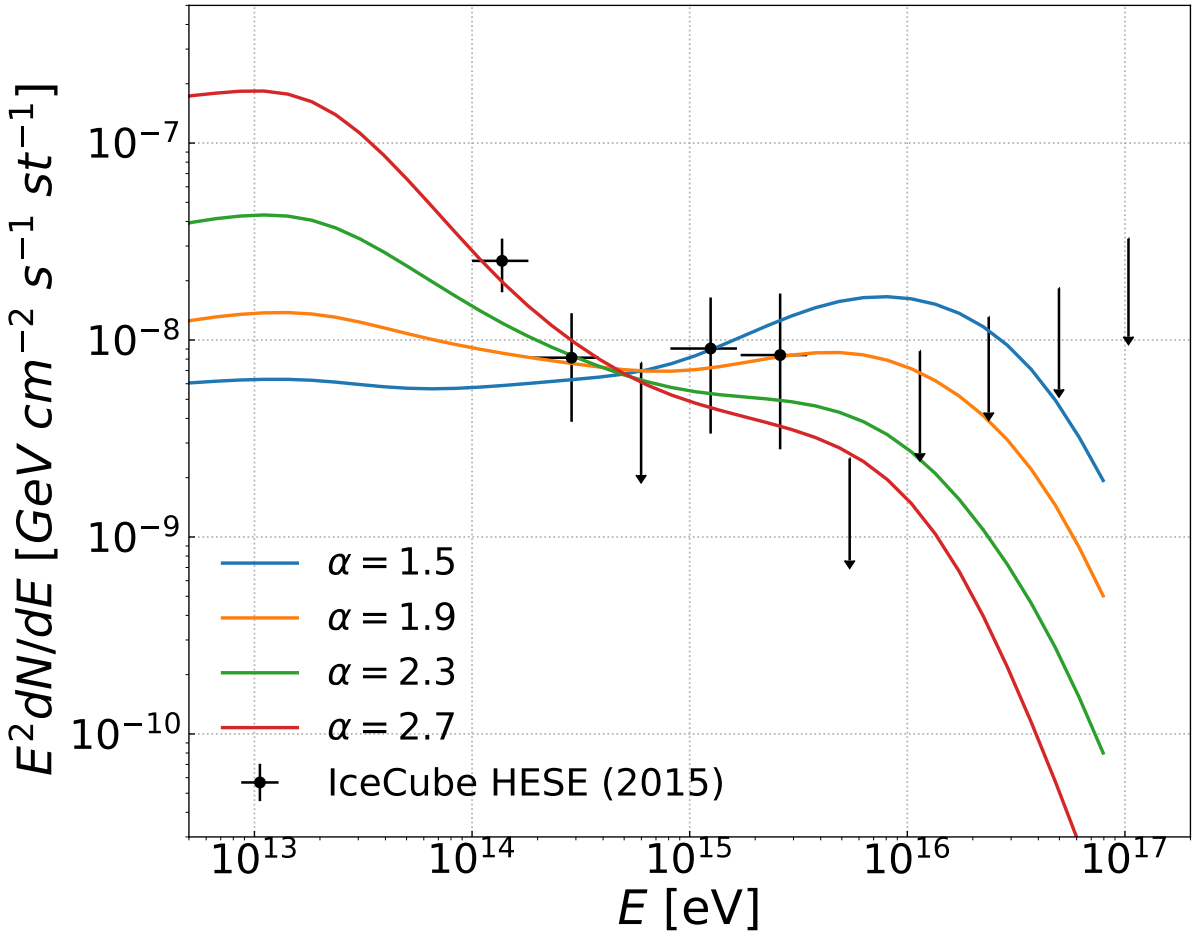

Figure 4.8: Total spectrum of neutrinos for different injected CR spectra, $\sim E^{-\alpha}$, with $\alpha = 1.5$ (blue), 1.9 (orange), 2.3 (green), 2.7 (red). We consider $E_{\max} = 5 \times 10^{17}$ eV. This figure does not include the redshift evolution of the CR sources, $\psi_{ev} = 1$ in Equation 4.3. It is assumed that 3% of the luminosity of the clusters is converted into CRs (Hussain et al., 2021).

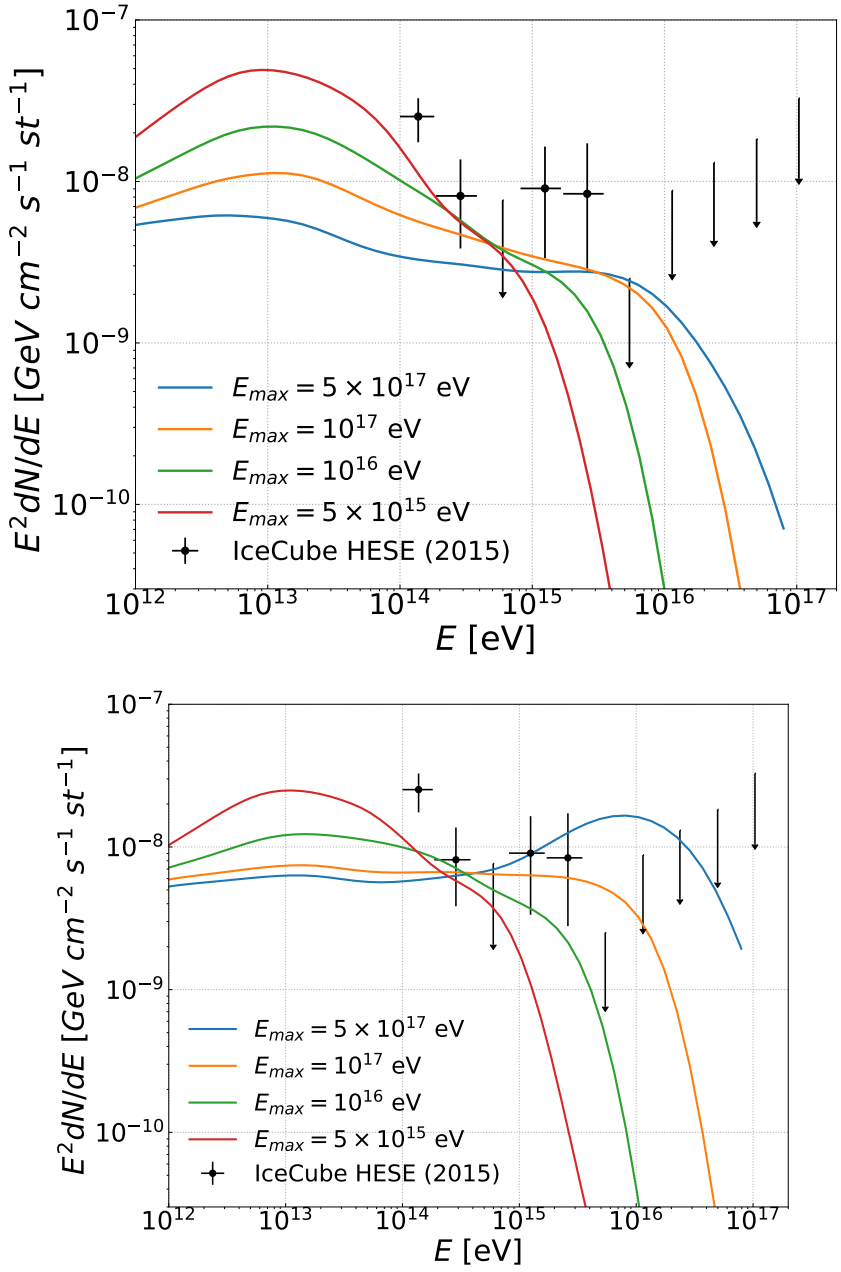

Figure 4.9: Total neutrino spectrum for different cutoff energies i.e., $E_{max} = 5 \times 10^{15}$ (red), 10^{16} (green), 10^{17} (orange), and 5×10^{17} eV (blue). In the upper panel the spectral index is $\alpha = 2$, and in lower panel $\alpha = 1.5$. This figure does not include the redshift evolution of the CR sources, $\psi_{ev} = 1$ in Equation 4.3. It is assumed that 3% of the luminosity of the clusters is converted into CRs (Hussain et al., 2021).

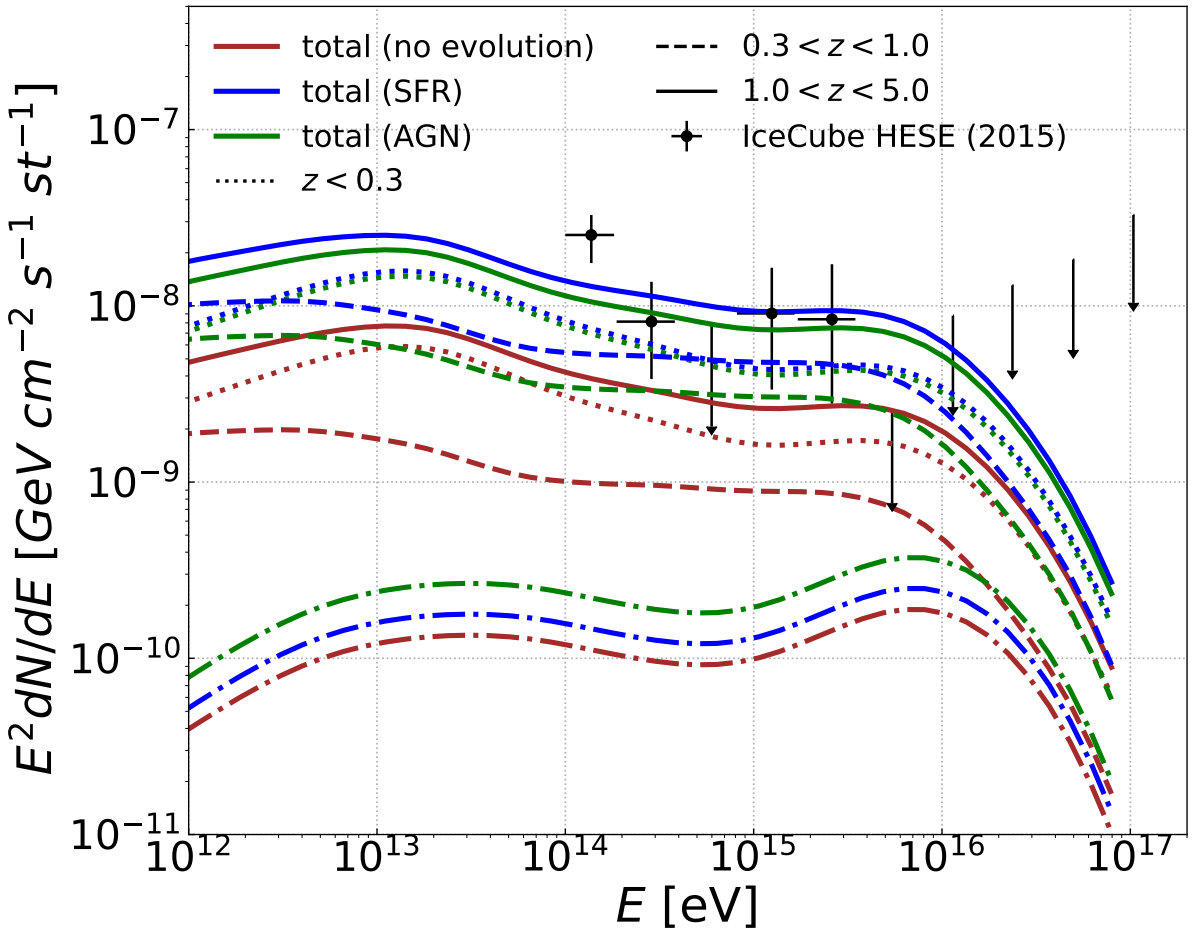

Figure 4.10: Neutrino spectrum for different assumptions on the evolution of the CR sources: SFR (blue), AGN (green), and no evolution (brown). The fluxes are shown for different redshift ranges: $z < 0.3$ (dotted lines), $0.3 < z < 1.0$ (dashed), and $1.0 < z < 5.0$ (dash-dotted lines). The CR injection spectrum has parameters $\alpha = 2$ and $E_{\rm max} = 5 \times 10^{17}$ eV. It is assumed that 3% of the luminosity of the clusters is converted into CRs (Hussain et al., 2021).

are both comparable at small redshifts ($z \leq 0.3$) which in turn, provide the dominant contribution to the total neutrino flux.

In Fig. 4.11, we plotted the flux for different combinations of spectral index α and E_{max}, with different source evolution assumptions as in Fig. 4.10. In both panels all the combinations of α and $E_{\rm max}$ are roughly matching with IceCube data (Aartsen et al., 2015), except $\alpha = 1.5$, and $E_{max} = 5 \times 10^{17}$ eV in the upper panel as it overshoots the IceCube points (Aartsen et al., 2015).

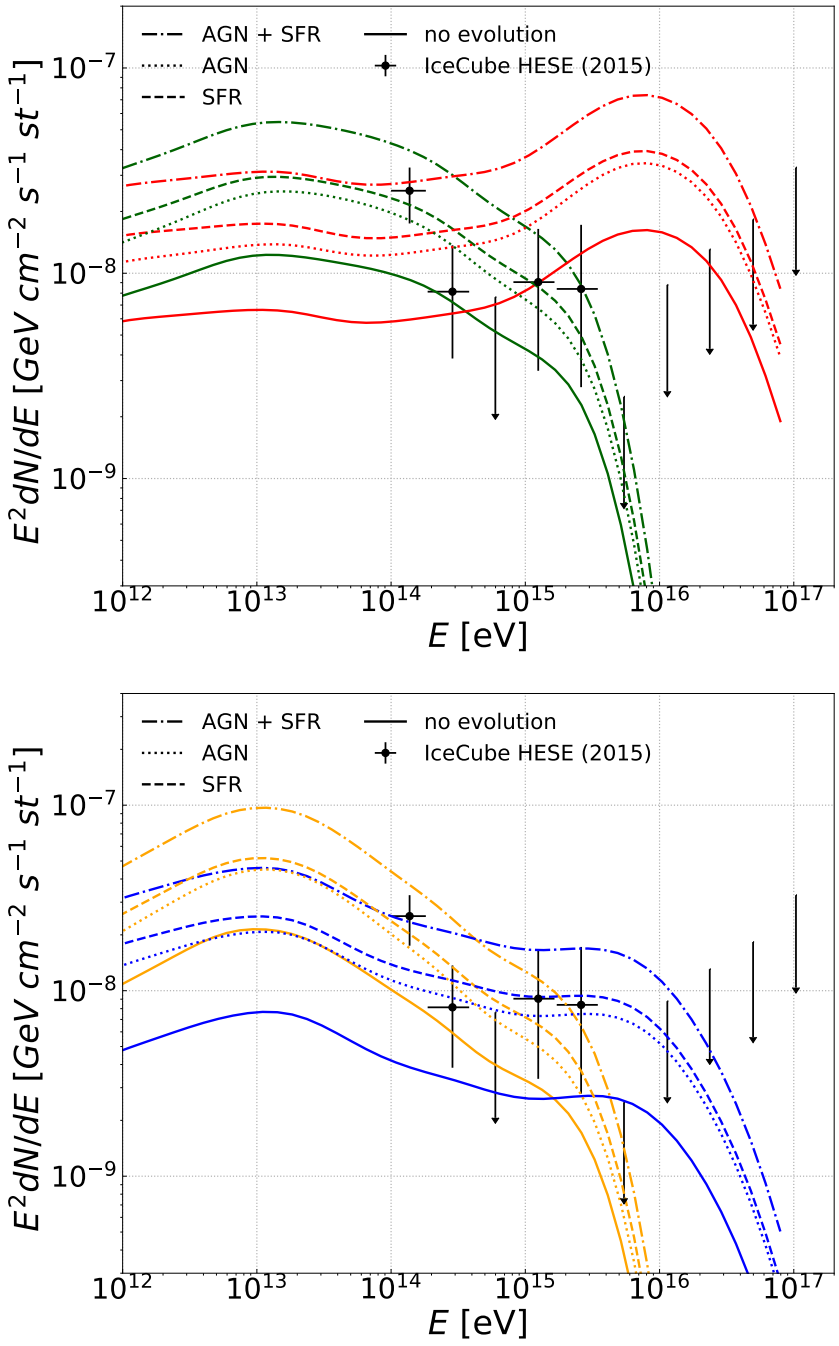

Figure 4.11: Flux of neutrinos for different assumptions on the evolution of the CR sources: no evolution (solid lines), SFR (dashed lines), AGN (dotted lines) and AGN + SFR (dash-dotted lines). In upper panel green and red lines represent $\alpha = 1.5$ for $E_{\rm max} = 10^{16}$ and 5×10^{17} eV respectively. In lower panel orange and blue lines correspond to $\alpha = 2$ for $E_{\rm max} = 10^{16}$ and 5×10^{17} eV, respectively. In both panels we assumed that 3% of the luminosity of the clusters is converted into CRs (Hussain et al., 2021).

4.4 Discussion

In our simulations, the central magnetic field strength and gas number density of the ICM are $\sim$ 10 μG and $\sim$ 10^{-2} cm^{-3}, respectively, for a cluster with mass 10^{15} $M_{\odot}$ at $z = 0.01$, and both decrease toward the outskirts of the cluster. These quantities depend on the mass of the clusters, being smaller for less massive clusters (see Figs. 2.4 - 2.6 in Chapter 2). Thus, high-energy CRs will escape with a higher probability without much interactions in the case of less massive clusters (see Fig. 4.4). Lower-energy CRs, on the other hand, contribute less to the production of high-energy neutrinos. Therefore, we have a lower neutrino flux from less massive clusters. In contrast, for massive clusters, higher magnetic field and gas density produce higher neutrino flux due to the longer confinement time, as we see in Fig. 4.4.

We tested several injection CRs spectral indices ($\alpha \simeq 1.5-2.7$), cut-off energies ($E_{\rm max} = 5\times10^{15}-10^{18}$ eV), injection power (with a fraction of $(0.5-3)\%$ of the clusters luminosity), and source evolution inside the clusters with the options (AGN, SFR, or no evolution), in order to try to interpret the IceCube data (Aartsen et al., 2015) (see Figs. 4.6 to 4.11). Overall, our results indicate that galaxy clusters can contribute to a considerable fraction of the diffuse neutrino flux measured by IceCube at energies between 100 TeV and 10 PeV (Aartsen et al., 2015), or even all of it, provided that that protons compose most of the CRs. The resulting flux has revealed to be more sensitive to the values of the spectral index and the cut-off energy than to the CR injection power, in the studied range.

Our results also look, in principle, similar to those of Fang and Olinto (2016) with no source evolution, who considered essentially the same redshift interval, but employed semi-analytical profiles to describe the cluster properties. In particular, in both cases, the largest contribution to the flux of neutrinos comes from the cluster mass group $10^{14} < M < 10^{15}$ $M_{\odot}$. However, they did not consider the interactions of CRs with CMB and EBL background as they considered them subdominant compared to the hadronic background following Kotera et al. (2009). But, we have seen in Fig. 3.6 of Chapter 3 that the MFP for pp-interaction and photopion production in the CMB are comparable for CRs of energy $\gtrsim 10^{17}$ eV. Therefore, the neutrino production due to CR interactions with the CMB is not negligible. Perhaps the most relevant difference between our results and theirs is that, in their case, the redshift range $0.3 \leq z \leq 1$ makes the largest contribution to neutrino

production, while in our case this comes from the redshift range $z \lesssim 0.3$, when considering no source evolution (see Fig 4.7).

When including source evolution, there is also a dominance in the neutrino flux from the redshift range $z \lesssim 0.3$, though the contribution due to the evolution of star forming galaxies (SFR) from redshifts $0.3 \leq z \leq 1$ is also important. Overall, the inclusion of source evolution can increase the diffuse neutrino flux by a factor of ~ 3 (when considering the separate contributions of AGN or SFR) to ~ 5 (when considering both contributions concomitantly) in the cases we studied, compared to the case with no evolution, which is in agreement with Murase and Waxman (2016). Also, our results agree with the IceCube measurements (Aartsen et al., 2015) for $E \gtrsim 10^{14}$ eV and are in rough accordance with Fang and Murase (2018). Nevertheless, since there are uncertainties related to the choice of specific populations for the CR sources, obtaining a full picture of the diffuse high-energy neutrino emission by clusters is not a straightforward task.

It is also worth comparing our results with Zandanel et al. (2015), who evaluated the neutrino spectrum based on estimations of the radio to gamma-ray luminosities of the clusters in the universe. Although our work has assumed an entirely different approach, both results are consistent, especially for a CR spectral index $\alpha \simeq 2$. High-energy ($E > 10^{17}$ eV) CRs can escape easily from clusters, effectively leading to a spectral steepening that was not considered by Zandanel et al. (2015). However, not all the clusters are expected to produce hadronic emission (Zandanel et al., 2014, 2015). In fact, we observe less hadronic interactions in the case of low-mass clusters ($M \lesssim 10^{14}\ M_{\odot}$), which could further limit the neutrino contribution from clusters.

The cluster scenario may get strong backing due to anisotropy detections above PeV energies. Recently, only a few sources of high-energy neutrinos have been observed (Aartsen et al., 2013, 2015; Albert et al., 2018; Ansoldi et al., 2018; Aartsen et al., 2020), but there are also expectations to increase the observations with future instruments like IceCube-Gen2 (The IceCube-Gen2 Collaboration, 2020), KM3NeT (KM3Net, 2016), and the Giant Radio Array for Neutrino Detection (GRAND) (Álvarez-Muñiz et al., 2020). Specifically, neutrinos from clusters are more likely to be observed if the flux of cosmogenic neutrinos is low, which might contaminate the signal, as discussed by Alves Batista et al. (2019).

4.5 Conclusions

We considered a cosmological background based on 3D-MHD simulations to model the cluster population of the entire universe, and a multidimensional Monte Carlo technique to study the propagation of CRs in this environment and obtain the flux of neutrinos that they produce. Our results can be summarized as follows:

- We found that CRs with energy $E \lesssim 10^{17}$ eV cannot escape from the innermost regions of the clusters, due to interactions with the background gas, thermal photons and magnetic fields. Massive clusters ($M \gtrsim 10^{14}\ M_{\odot}$) have stronger magnetic fields which can confine these high-energy CRs for a time comparable to the age of the universe.

- Our simulations predict that the neutrino flux above PeV energies comes from the most massive clusters because the CR interactions with the gas of the ICM are rare for clusters with $M < 10^{13}\ M_{\odot}$.

- Most of the neutrino flux comes from nearby clusters in the redshift range $z \lesssim 0.3$. The high-redshift clusters contribute less to the total flux of neutrinos compared to the low-redshift ones, as the population of massive clusters at high redshifts is low.

- The total integrated neutrino flux obtained from the interactions of CRs with the ICM gas and CMB during their propagation in the turbulent magnetic field can account for sizeable percentage of the IceCube observations, especially, between energy 100 TeV and 10 PeV.

- Our results also indicate that the redshift evolution of CR sources like AGN and SFR, enhances the flux of neutrinos.

Finally, more realistic studies considering cosmological simulations that account for AGN and star formation feedback from galaxies (e.g. Barai and de Gouveia Dal Pino, 2019; Hopkins et al., 2021) will allow to constrain better the redshift evolution of the CR sources in the computation of the total neutrino flux from clusters. Furthermore, in the future, IceCube will have detected more events. Then, combined with diffuse gamma-ray searches by the forthcoming CTA (CTA, 2018), it will be possible to better assess the contribution of galaxy clusters to the total extragalactic neutrino flux.

Chapter 5

The Diffuse Gamma-Ray Flux from Clusters of Galaxies

As stressed in Chapter 1 , the origin of the diffuse gamma-ray background (DGRB) detected by EGRET (Colafrancesco and Blasi, 1998; Sreekumar et al., 1998; Strong et al., 2004) and Fermi-LAT (Ackermann et al., 2012, 2015; Yang and Wang, 2020; Neronov and Semikoz, 2020), the one that remains after subtracting all individual sources from observed gamma-ray sky, is unknown. The DGRB gives a non-thermal perspective of the universe that is also explored through the extragalactic UHECRs and neutrinos. The observed energy fluxes of these three components are all comparable (Ahlers and Halzen, 2018; Fang and Murase, 2018) and suggest that they may have a common origin. In this Chapter, we combine the same cosmological MHD simulations of clusters of galaxies with the propagation of CRs using Monte Carlo simulations, considering redshifts $z \lesssim 5$, in order to compute the flux of gamma-rays due to the large scale structures. The results of this Chapter have been recently submitted to publication (Hussain et al., 2022).

5.1 Introduction

The DGRB possibly encompasses contributions from different source populations such as star-forming galaxies (SFGs), pulsars, active galactic nuclei (AGNs), gamma-ray bursts (GRBs) (Stecker and Venters, 2011; Fornasa et al., 2013; Di Mauro et al., 2013; Di Mauro and Donato, 2015; Ajello et al., 2015; Albert et al., 2021; Roth et al., 2021) or, even more likely, from the integrated contribution of all these sources within clusters of galaxies (Murase et al., 2013; Brunetti and Jones, 2014; Brunetti et al., 2017).

As discussed in Chapter 1 and 4, several analytical and semi-analytical models have

been employed to estimate the fluxes of gamma rays and neutrinos stemming from CR interactions in the intracluster medium (ICM) (Berezinsky et al., 1997; Rordorf et al., 2004; Kotera et al., 2009; Fang and Murase, 2018), but in all these studies the ICM is assumed to have spherically symmetric distributions of magnetic fields and gas. In this Chapter, we extend the study described in Chapter 4 (Hussain et al., 2021), and use the same approach to compute the diffuse gamma-ray flux from the galaxy clusters, at the Earth. Distinctly from the neutrino flux computed in Chapter 4, the calculation of the DGRB requires not only the evaluation of the flux that emerges from the clusters, but also its propagation and cascading into the IGM.

5.2 Simulation Setup

The simulation setup is the same as described in Chapters 2 to 4. We employ the 3D-MHD cosmological simulations described in Chapter 2. We are interested in high-energy gamma rays with $E \gtrsim 10$ GeV and thus consider CRs with energies $10^{11} \leq E/\mathrm{eV} \leq 10^{19}$. The upper limit can be achieved by primary sources, such as AGNs (Fang and Murase, 2018; Murase et al., 2008). As remarked in Chapter 3, for magnetic fields of $B \sim 1$ μG, the Larmor radius of CRs with $E \sim 10^{19}$ eV is $r_{\mathrm{L}} \sim 10$ kpc, so that they cannot remain trapped within clusters for too long. On the other hand, CRs with lower energies remain confined, producing secondaries due to their interactions with the ICM gas and the Bremsstrahlung radiation, as well as with the cosmic microwave background (CMB) and the extragalactic background light (EBL) (e.g., Pfrommer, 2008; Murase et al., 2008; Fang and Olinto, 2016; Hussain et al., 2021).

We explore the propagation of CRs in the simulated background of clusters in the same way as described in Chapters 2 and 4. The propagation has two steps (see Fig. 5.1) and we assume that the CRs are predominantly composed by protons only (see Chapter 1 for discussion). In the first step, we compute the gamma-ray flux produced by CR interactions in the clusters by considering all relevant interactions that generate both electrons and photons (see Section 3.4). In the second step, we perform the propagation of the gamma rays collected at the boundary of the clusters up to Earth. We consider the electromagnetic cascade process initiated by these gamma rays in the intergalactic medium, including inverse Compton scattering, single, double, and triplet pair production,

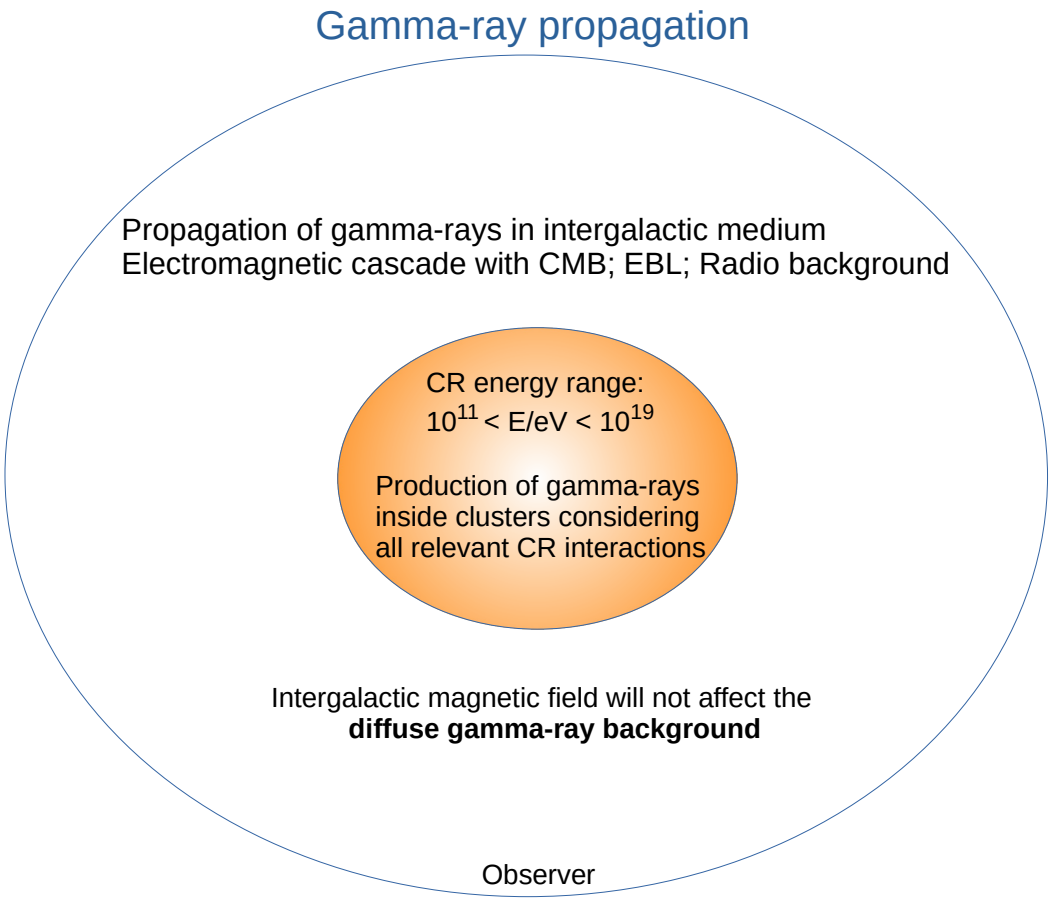

Figure 5.1: Schematic diagram of gamma-ray production in clusters of galaxies and its propagation in the intergalactic medium.

with the CMB, the EBL (Gilmore et al., 2012), and the radio background [1] (Protheroe and Biermann, 1996) (see Sections 3.3 and 3.4). We did not consider the effects of intergalactic magnetic fields outside the cluster in this step, since they are highly uncertain and are not expected to majorly affect the gamma-ray flux at energies above $\sim$ 100 GeV (Vazza et al., 2017; Alves Batista and Saveliev, 2021).

To convert the code units of the CR simulations to physical units, we have followed the same procedure described in Section 4.1 (see also Hussain et al., 2021). We considered here that 1% of the cluster luminosity goes into CRs which is consistent with Fermi-LAT predictions of gamma rays from clusters (Ackermann et al., 2014; Brunetti and Jones, 2014) [2]. We adopt for the injected CR spectral index the values $\alpha = 1.5 - 2.5$, and for

[1] Extragalactic radio background is based on the observed luminosity functions and radio spectra of normal galaxies and radio galaxies.

[2] We note that the fraction of the cluster luminosity that goes into CRs is slightly different from that adopted in the study of the neutrino emission described in Chapter 4. There, we left this fraction as a

$E_{max} = 10^{16} - 5 \times 10^{17}$ eV, which are the most suitable combination able to reproduce the Fermi-LAT observations, as we describe in Appendix C (see also Fig. 5.7).

5.3 *The flux of gamma rays*

The high-energy gamma rays produced inside clusters have the energy range $10^9 \lesssim E/\mathrm{eV} \lesssim 5 \times 10^{15}$, as shown in Figs. 5.2 and 5.3 , which depict the flux collected at the edge of clusters with different masses and redshifts. The Fig. 5.3 shows the dependence of the photon flux on the position of the CR sources inside the clusters. As expected, the photon production is smaller when the source is located farther away from the center. The CRs can escape more easily from the less dense and lower magnetic fields in the outskirts of the clusters and thus produce less photons. In addition, , both figures also shows that massive clusters can produce more photons than lighter ones. The mass range of clusters in our background simulation is $10^{12} \lesssim M/M_\odot < 5 \times 10^{15}$ and clusters with masses $\lesssim 10^{13}\ M_\odot$ barely contribute to HE gamma-ray flux. This occurs due to the lower interaction rate between CRs and the intracluster environment, which is a consequence of the interplay between the Larmor radius, determined by the magnetic field, and the cluster size. Also, there are fewer clusters with mass $\gtrsim 10^{15}\ M_\odot$, especially at high redshift ($z > 1$). Therefore, the major contribution to gamma rays flux comes from clusters in the mass range $10^{13} < M/M_\odot < 10^{15}$.

We present the integrated gamma-ray spectrum from all clusters in the redshift interval $z \leq 5.0$, propagated up to the Earth, in Figs. 5.4, 5.5, 5.7, 5.9, and C.1. The total flux (Φ) was computed as follows:

$$E^2\Phi(E) = \int_{z_{\min}}^{z_{\max}} dz \int_{M_{\min}}^{M_{\max}} dM \frac{dN}{dM} E^2 \frac{d\dot{N}(E/(1+z), M, z)}{dE} \left(\frac{\psi_{\mathrm{ev}}(z) f(M)}{4\pi d_L^2(z)} \right) \tag{5.1}$$

The above equation is the same as the Equation 4.3 of Chapter 4 except for the factor $f(M)$ which represents the gas density correction in the clusters due to star-formation and AGN feedback. The values employed here as a function of the mass of the clusters are described below (see Fig. 5.8 and 5.9). They have been constrained by observations

free parameter, given the uncertainties associated to it, and in order to reproduce the observed flux of neutrinos, we adopted values between $(0.5 - 3.0)\%$ for this ratio.

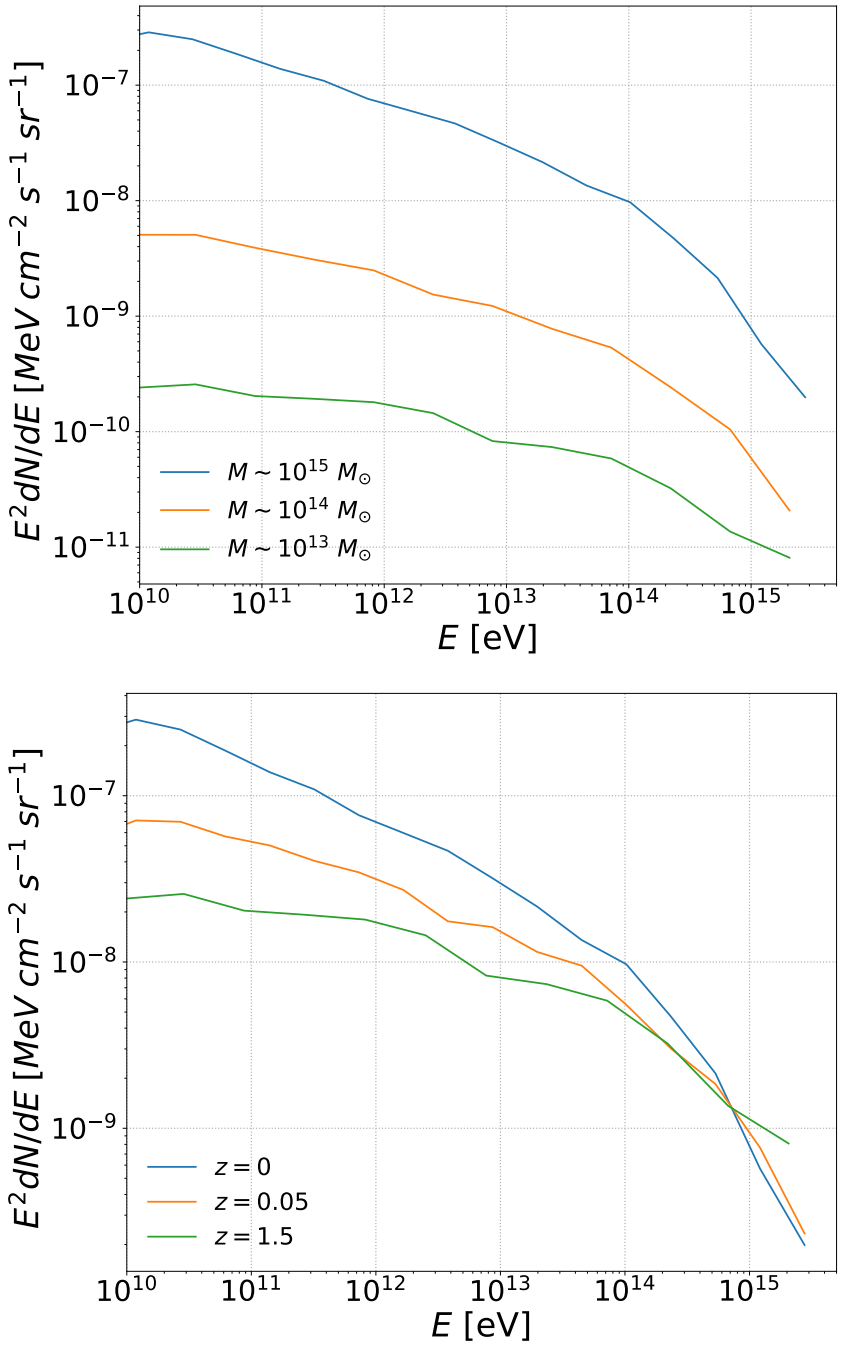

Figure 5.2: This diagram shows the photon flux for individual clusters (collected at the edge ~ 2 Mpc) of different masses (upper panel) and redshifts (lower panel). The spectral index of the CR spectrum has a power-law index $\alpha = -2$ and an exponential energy cut-off $E_{\max} = 10^{17}$ eV (Hussain et al., 2022).

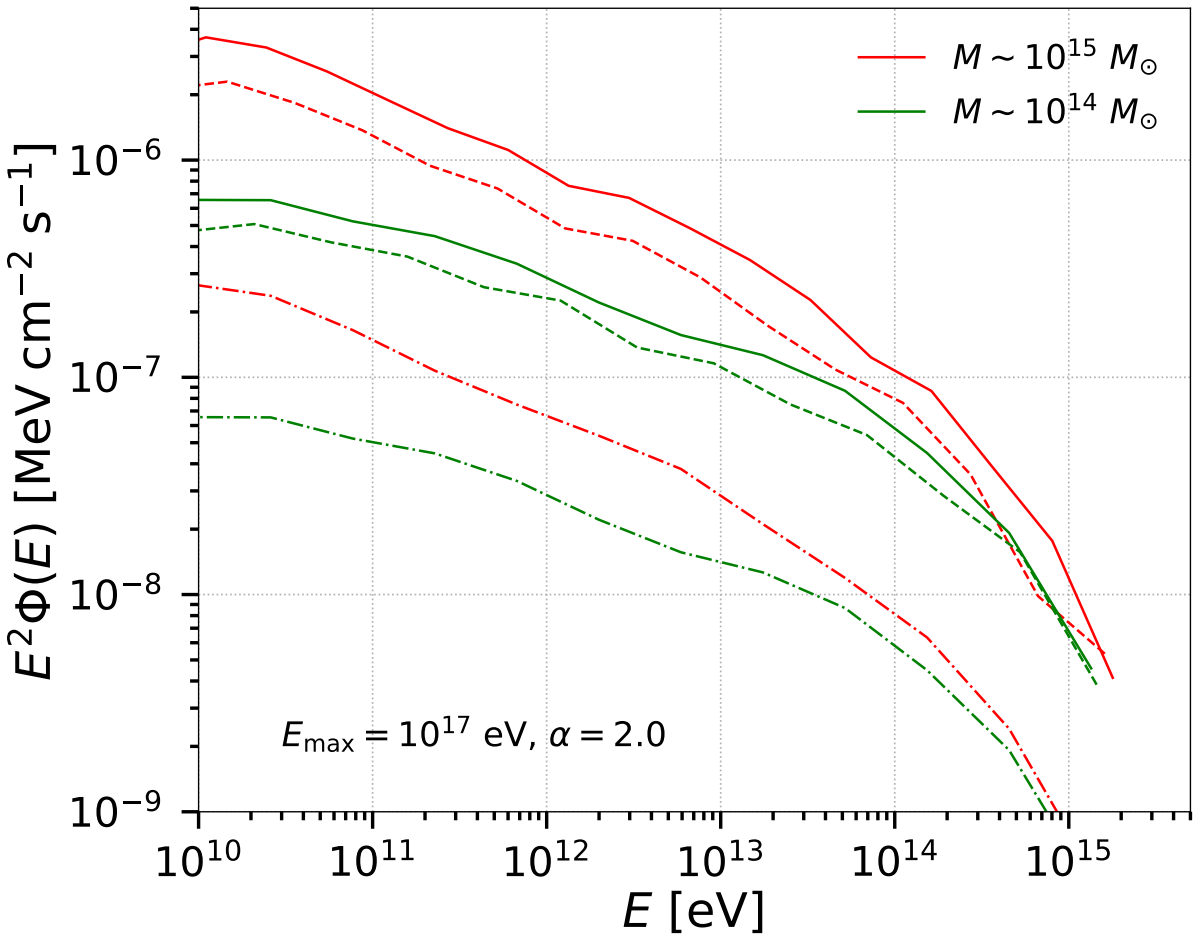

Figure 5.3: Gamma-ray flux at the edge of individual clusters (radius ~ 2 Mpc) of mass $M \sim 10^{15}\ M_\odot$ (red); and $10^{14}\ M_\odot$ (green), at redshift $z \sim 0$. We considered CR sources located at the center of the cluster (solid lines), at 300 kpc (dashed lines), and at 1 Mpc away from the center (dash-dotted lines). The spectral index of the CR spectrum has a power-law index $\alpha = -2$ and an exponential energy cut-off $E_{\rm max} = 10^{17}$ eV (Hussain et al., 2022).

(Fabjan et al., 2010; Planelles et al., 2014; Lovisari et al., 2015). For the computation of the neutrinos, we had assumed $f(M) = 1$ (see justification below).

The universe is believed to be isotropic and homogeneous at very large scales (Schneider, 2006). Therefore, for the propagation of gamma rays from the clusters to Earth, we assumed a nearly uniform distribution of sources (UDS) in comoving coordinates. In order to understand how much our results depend on the assumption of UDS, we have computed the gamma-ray fluxes for two different random distributions of sources (SMP1 and SMP2) within the same distance ranges and compared them with the UDS results. To do the random realization of the sources we calculated the number of clusters ($N_{Clusters}$ = cluster density $\times$ volume of a sphere of radius z_{max}) distributed within the maximum distance given by the maximum redshift ($z_{max} = 5.0$) of our MHD background and used these distributions in our simulations of gamma-ray propagation. The comparison of the UDS results with the two different random distributions of sources is shown in Fig. 5.4. The results are similar for both cases and we adopted the UDS distribution to compute the integrated total flux of gamma-rays in the figures that follow.

Fig. 5.5 depicts the total flux for different redshift intervals: $z \leq 0.3$, $0.3 < z \leq 1.0$, and $1.0 < z \leq 5.0$. The dominant contribution to the total flux of gamma rays comes from sources at low redshifts ($z \leq 0.3$), for which the effect of the EBL attenuation is less pronounced. This effect is more prominent at higher redshifts and also depends on the EBL model adopted Gilmore et al. (2012); Dominguez et al. (2011); Stecker et al. (2016) (see Fig. 5.6). Fig. 5.5 shows the results for the EBL model from Gilmore et al. (2012), which predicts a slightly larger gamma-ray cut-off energy for the flux. Also, our treatment of the pp-interactions (Kelner et al., 2006; Kafexhiu et al., 2014) is only an approximation and contains uncertainties due to the unknown pp cross-section at energies beyond the reach of the LHC (Aaboud et al., 2016). The figure also highlights the effects of the evolution of the CR sources on the gamma-ray flux, distinguishing the separated contributions of AGN and SFR, following the same procedure as in Alves Batista et al. (2019); Hussain et al. (2021). Similarly to the neutrinos, we find that an AGN-type evolution enhances the diffuse gamma-ray flux at high redshifts ($z \gtrsim 1.5$) compared to scenarios wherein the sources evolve as the SFR (or without any evolution), while they are both comparable at small redshifts ($z \leq 0.3$) which in turn, provide the dominant contribution to the total gamma-ray flux.

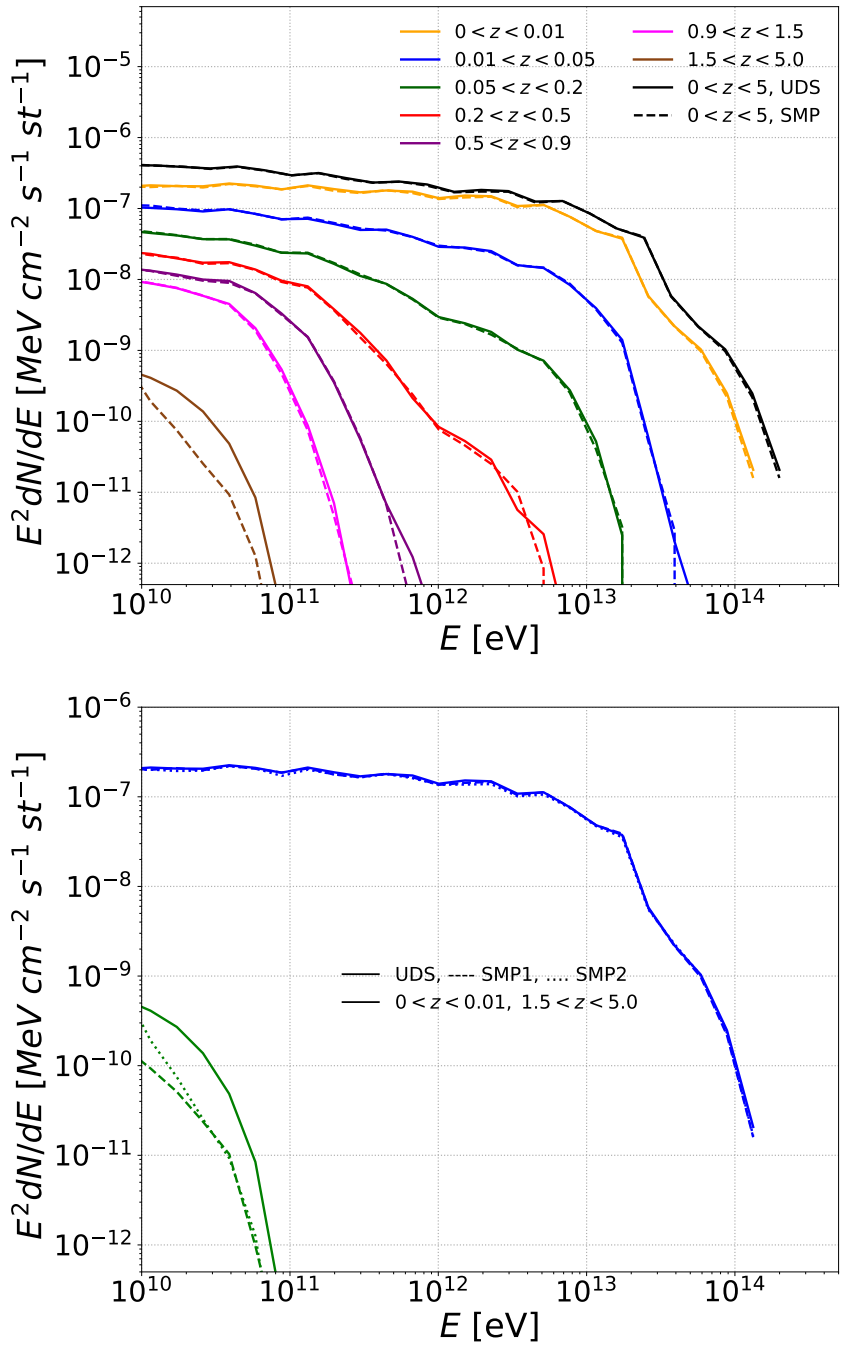

Figure 5.4: In this figure we compared the spectrum of UDS (solid lines) with the random realization of sources (dashed lines) for different radshift intervals in both panels. The spectral index and cutoff energy in both panels is $\alpha = 2.0$ and $E_{\rm max} = 10^{17}$ eV. In the upper panel, the UDS and the sources random realization SMP1 models are compared, while in the lower panel they are both compared to SMP2 model too (see text for more details). In the lower panel, blue lines represent the flux for redshift interval $0 < z < 0.01$ and green lines are for $1.5 < z < 5.0$.

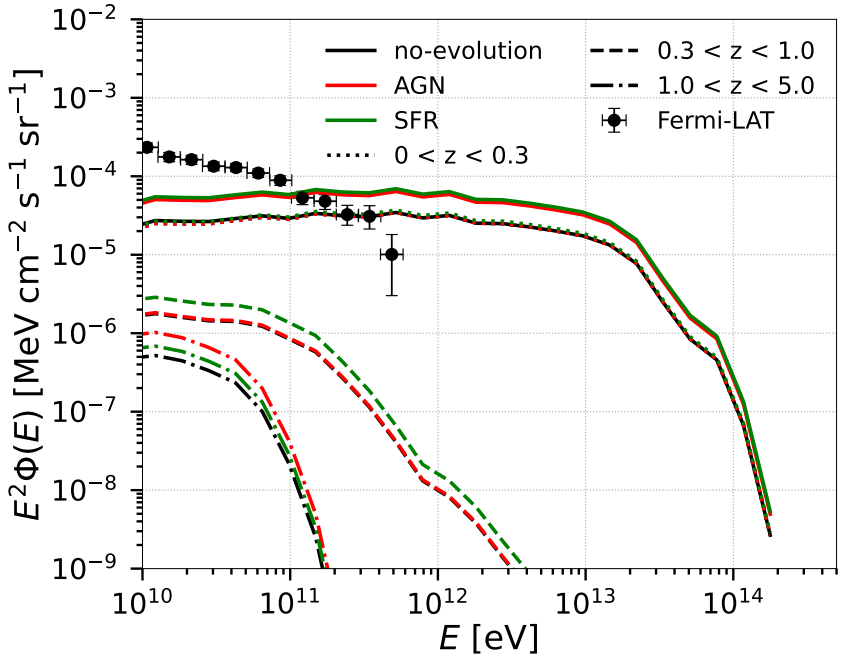

Figure 5.5: In this figure, we compared the total photon flux of UDS (solid lines) with the random distribution of sources (SMP, dashed lines). Bottom panel: Total flux of gamma rays for $\alpha = 2$ and $E_{\max} = 10^{17}$ eV over the entire redshift range (solid lines) and also for different redshift intervals. The figure also compares the flux including the separated contributions of the evolution of the CR sources (AGN and SFR) with the flux when there is no source evolution. The observed flux by Fermi-LAT is depicted too from Ackermann et al. (2015) (Hussain et al., 2022).

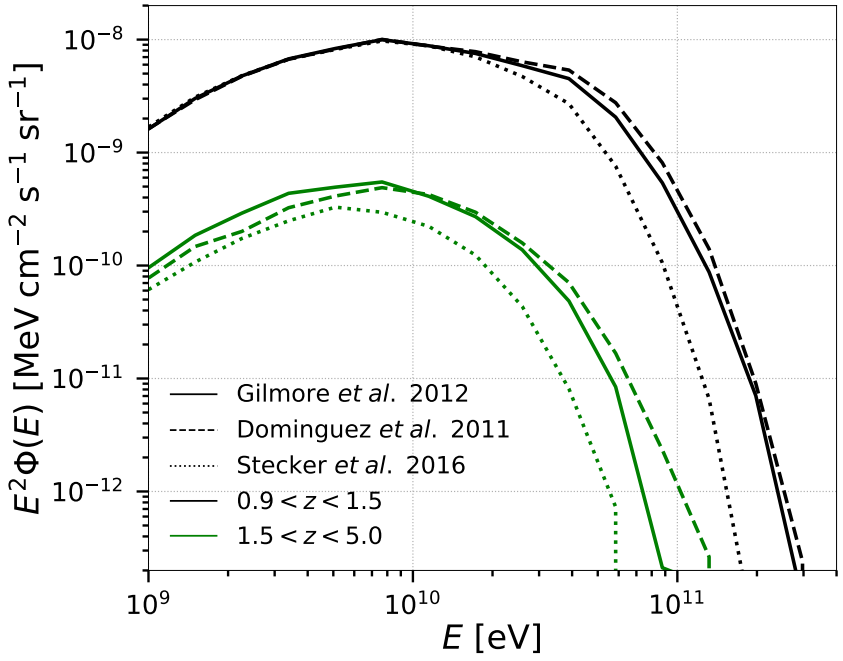

Figure 5.6: Effect of EBL attenuation on the gamma-ray flux for two redshift intervals and three different EBL models (Gilmore et al., 2012; Dominguez et al., 2011; Stecker et al., 2016) (Hussain et al., 2022).

We further notice that the flux of gamma rays above energies $\sim 10^{12}$ eV can also be attenuated by interactions with the local optical and infrared photon fields of clusters, in addition to the EBL. Nevertheless, this attenuation effect is more dominant for sources at redshift $z \gtrsim 0.3$ as predicted by Murase and Waxman (2016). In our case, the major contribution corresponds to sources at $z \leq 0.3$. Therefore, we expect that this interaction channel has likely a minor impact on our results.

The shaded region in Fig. 5.7 shows the total flux of gamma rays for the entire redshift range $0 < z \leq 5.0$, calculated for $\alpha = 1.5 - 2.5$ and $E_{\rm max} = 10^{16} - 10^{17}$ eV, including the AGN sources evolution. In Fig. 5.7 we compare our flux with the expected flux from Coma-like clusters (Nishiwaki et al., 2021), the flux from clusters obtained by Murase et al. (2013), and the flux from Zandanel et al. (2015) for 100% (solid line) and 30% (dashed line) radio-loud clusters in the redshift range $0.044 < z < 0.2$.

Besides the observed flux by Fermi LAT, we also present in Fig. 5.7 the upper limit for the DGRB obtained by the currently operating experiment HAWC with 815 days of observations (Harding, 2019) and the high-energy limit on gamma-rays obtained by CASA-MIA (Chantell et al., 1997). The flux we obtained is comparable with the observational upper limits of HAWC.

In Fig. 5.9 we have recalculated the total diffuse gamma-ray flux (black dashed line) considering correction factors $f(M) \sim 0.95$ for clusters with $M \gtrsim 10^{15}\ M_{\odot}$, $f(M) \sim 0.8$ for $M \gtrsim 10^{14}\ M_{\odot}$, $f(M) \sim 0.3$ for $M \gtrsim 10^{13}\ M_{\odot}$, and $f(M) \sim 0.3$ for $M \gtrsim 10^{12}\ M_{\odot}$, see Fig. 5.8 (see also Lovisari et al., 2015). The gas density of clusters can be reduced due to AGN-feedback and star-formation. Consequently, this can decrease the flux by a factor 2 or so (see Fig. 5.9).

5.4 *Discussion and Conclusion*

Our results indicate that the clusters can contribute to a sizeable fraction of the DGRB observed by Fermi-LAT especially above 100 GeV, for CR spectra with index $\alpha = 2.0 - 2.5$ and $E_{\rm max} = 10^{16} - 10^{17}$ eV. The spectral indices considered here are consistent with the universal CR model by Pinzke and Pfrommer (2010) used by Fermi-LAT to explore the CR induced gamma-ray emission from clusters Ackermann et al. (2014), and by H.E.S.S. for the Coma cluster ($\alpha = 2.1 - 2.4$) (Aharonian et al., 2009), while the $E_{\rm max}$ range is compatible

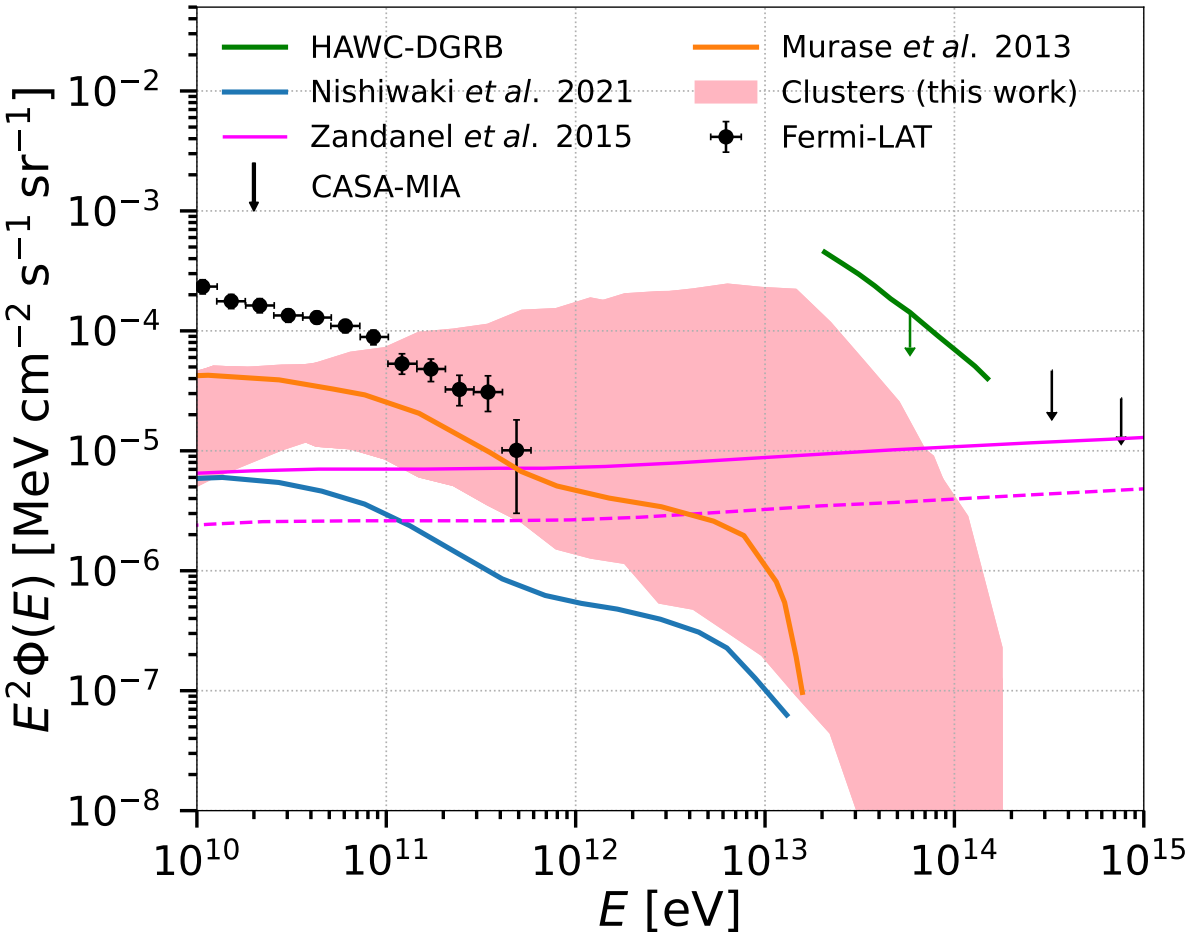

Figure 5.7: Integrated gamma-ray flux from the entire population of clusters. The pink shaded region represents the integrated gamma-ray flux obtained in this work for $E_{\rm max} = 10^{16} - 10^{17}$ eV and spectral index $\alpha = 1.5 - 2.0$. We compare our results with the total gamma-ray flux from clusters obtained in previous works Zandanel et al. (2015); Murase et al. (2013); Nishiwaki et al. (2021), and also with the DGRB from Fermi LAT (Ackermann et al., 2015) and the upper limits from HAWC Harding (2019) and the CASA-MIA Chantell et al. (1997) experiments.

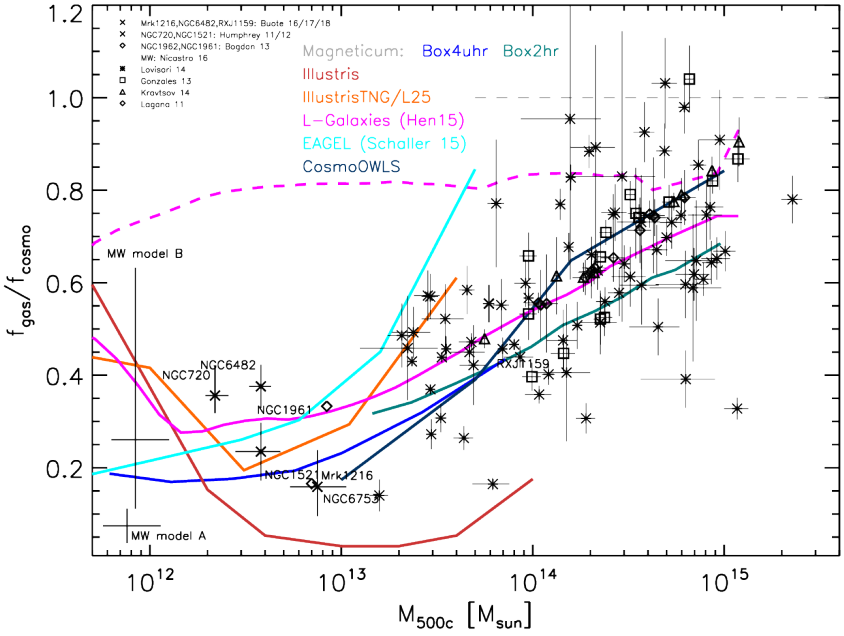

Figure 5.8: Reduction in the gas density due to star formation and stellar and AGN feedback in clusters of galaxies as a function of their masses (see Fabjan et al., 2010; Planelles et al., 2014; Lovisari et al., 2015, for review)

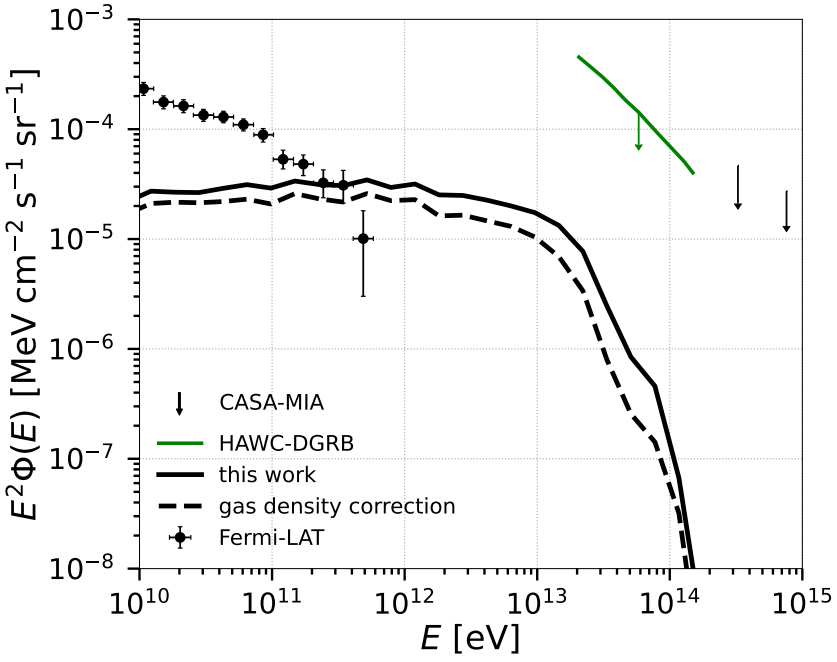

Figure 5.9: Total gamma-ray flux for $\alpha = 2.0$ and $E_{\max} = 10^{17}$ eV over the entire redshift range (solid black line). It is compared with the total gamma-ray flux we obtain when accounting for the gas loss of the clusters due to star formation and AGN feedback (black dashed line). The DGRB from Fermi-LAT and upper limit from HAWC (Harding, 2019) and CASA-MIA (Chantell et al., 1997) is also shown. See text for details.

with the fact that the clusters can confine mainly CRs with energies $E \lesssim 10^{17}$ eV (Inoue et al., 2007; Fang and Olinto, 2016; Hussain et al., 2021).

The gamma-ray flux we obtained from the entire population of clusters, specially for CR spectral index ~ 2 and energy cutoff $\sim 10^{17}$ eV, is comparable with Murase et al. (2013) (Fig. 5.7). In Murase et al. (2013), they estimated the gamma-ray flux from clusters using a purely hadronuclear scenario (pp-interaction) claiming that these sources would contribute with at least $30\% - 40\%$, or even 100% but for softer spectra ($\alpha \gtrsim 2.2$), to the DGRB. In comparison with the estimated spectrum for Coma-like clusters (Nishiwaki et al., 2021), our gamma-ray flux is a little higher. In both studies (Murase et al., 2013; Nishiwaki et al., 2021), besides the oversimplified ICM magnetic-field and density distributions, assumed to have radial profiles, they did not account for the contributions from clusters of mass $\lesssim 10^{14}\ M_\odot$. In Coma-like clusters (Nishiwaki et al., 2021), where masses are $\sim 10^{15}\ M_\odot$, the average density is $\sim 10^{-6}$ Mpc^{-3}, but it is $\sim 10^{-4}$ Mpc^{-3} for cluster masses of a few $10^{14}\ M_\odot$ (as considered in Nishiwaki et al. (2021); Murase et al. (2013)), and can be even larger for masses $< 10^{14}\ M_\odot$, as predicted by large scale cosmological simulations (Jenkins et al., 2001; Rosati et al., 2002; Bocquet et al., 2016) and obtained in our MHD cosmological simulations. Because we are considering here the entire mass range ($10^{12} \leq M/M_\odot < 5 \times 10^{15}$), the density is higher by an order of magnitude, and this is the main difference between ours and these previous studies (Murase et al., 2013; Nishiwaki et al., 2021). Also, we find that the major contribution comes from the most abundant mass interval of clusters ($10^{13} \leq M/M_\odot < 10^{15}$). Another relevant study (Zandanel et al., 2015) estimated the flux using a simple relation between the gamma-ray luminosity and the cluster mass. They constrained the radio-loud cluster count from observations by the Radio Astronomy Observatory Very Large Array sky survey (Giovannini et al., 1999; Cassano et al., 2010) and also assumed that the radio luminosity scales linearly with the hadronic high-energy emission. The flux they obtained for $\alpha = 2.0$, assuming that all clusters are radio loud but in a limited redshift range of $0.044 < z < 0.2$, is comparable to our results, as shown in Fig. 5.7. However, if only 30% of the population of clusters is radio loud, then their estimated fluxes are much lower. Also, they omitted the absorption of gamma rays due to interactions with the EBL, which for $E \gtrsim 1$ TeV is relevant only at high redshifts (Dominguez et al., 2011).

Though individual source populations such as blazars (Ajello et al., 2015), misaligned-

AGNs (Di Mauro et al., 2013) and star-forming galaxies (SFGs) (Roth et al., 2021) can contribute to a fairly large fraction to the DGRB for energies below TeV (Fornasa and Sanchez-Conde, 2015), and even considering more recent claims that indicate that SFGs alone can explain the DGRB observed by Fermi-LAT (Roth et al., 2021), our results demonstrate that the cumulative gamma-ray flux from clusters can dominate over the contribution from individual classes of sources at energies $\gtrsim 100$ GeV (see Fig.5.10). The implications of our calculations are extremely important considering that the contribution from clusters is *guaranteed* if high-energy CRs are present in the ICM.

Finally, as remarked, our MHD simulations do not include radiative-cooling, or the amount of gas that is converted into stars or removed from the clusters due to stellar and AGN feedback. This implies a slight overestimation of the density in the structures, especially for clusters of mass $\lesssim 10^{14}\ M_{\odot}$ (see Fabjan et al. (2010); Planelles et al. (2014)). Based on the observational results (Lovisari et al., 2015), we have also estimated the total gamma-ray flux taking into account the expected decrease of the gas density as a function of the cluster mass. A comparison between the dashed and solid black lines of Fig. 5.9 indicates a small reduction of the flux by at most a factor 2. Future more realistic MHD cosmological simulations that account directly for the CR sources evolution and feedback (see e.g., Barai and de Gouveia Dal Pino, 2019; Hopkins et al., 2021) may allow to constrain better the contribution of clusters to the DGRB.

As shown in Fig. 5.7, our results are comparable with the upper limits of HAWC at very high energies for the DGRB. A similar evaluation or prediction has not been performed yet by other facilities like the Large High Altitude Air Shower Observatory ((LHAASO, Di Sciascio et al., 2016)) or the forthcoming Cherenkov Telescope Array (CTA, CTA, 2018). Nevertheless, considering the sensitivity curves for point sources obtained in both cases, the gamma-ray flux we derived has likely the potential to be detected by these facilities too (see Fig.5.10).

Our results were obtained through the most detailed simulations to date of three-dimensional particle transport in cosmological environments. Combined with the other known components of the DGRB, our results strongly constrain the fraction of the diffuse flux that could be ascribed to unknown components such as the elusive dark matter. Moreover, it establishes a clear connection between the fluxes of two messengers, neutrinos and gamma rays, which, combined, enables us to indirectly study CRs in clusters even if

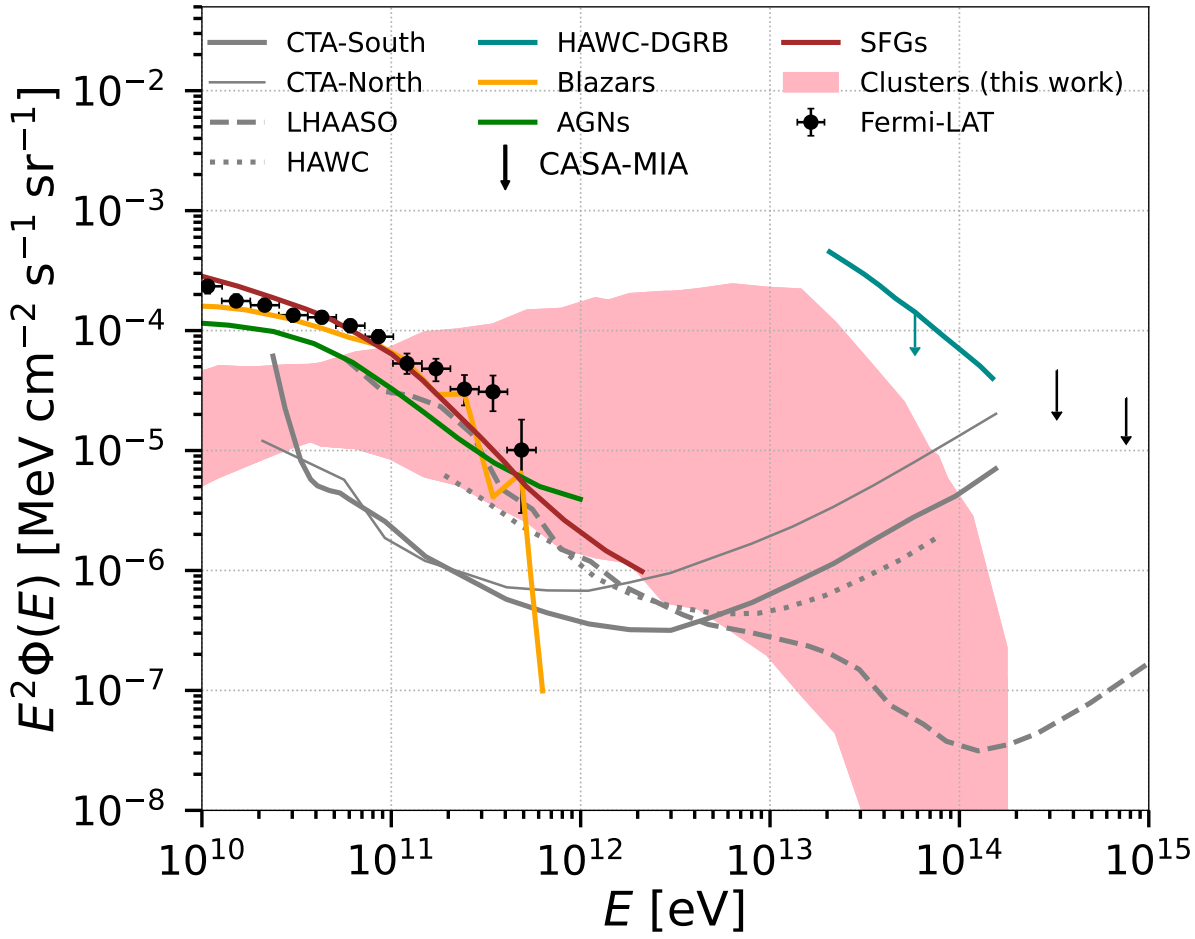

Figure 5.10: Contribution to DGRB from different types of astrophysical sources. The pink band is plotted for the fiducial range of parameters in our work $\alpha = 1.5 - 2.5$, $E_{\rm max} = 10^{16} - 10^{17}$ eV. Besides showing the observed DGRB flux from Fermi-LAT (Ackermann et al., 2015) and upper limits from HAWC (Harding, 2019) and CASA-MIA (Chantell et al., 1997) (as in Fig. 5.7), this figure also presents the sensitivity curves obtained for point sources from LHAASO (Di Sciascio et al., 2016), HAWC (Abeysekara et al., 2013), and the forthcoming CTA North and South observatories (CTA, 2018) for comparison (gray curves). We also showed the contribution from individual sources to DGRB i.e. blazars (Ajello et al., 2015), AGNs (Di Mauro et al., 2013), and SFGs (Roth et al., 2021).

they are not directly observable.

Chapter 6

Conclusions and Future Perspectives

6.1 Summary: what we have learned

In this Thesis, we explored the contribution of clusters of galaxies to the observed diffuse neutrino and gamma-ray combining cosmological MHD and CR Monte Carlo simulations, considering all relevant CR interactions during propagation in the intracluster medium and the subsequent gamma-ray cascading in the intergalactic medium. Our results indicate that clusters can contribute to a fairly large fraction of the highest energy photon flux observed by Fermi-LAT. We also predict the observation of gamma rays from these sources by future observatories (CTA and LHAASO). The neutrinos flux we obtained provides a substantial fraction of the observed emission by the IceCube at the highest energies.

This work provides relevant results in the area of gamma-ray and multi-messenger astrophysics. Firstly, it is a major step forward computationally, as it comprises the most detailed calculations to date of this type of process, employing techniques that are rarely used together (3D simulations of particle propagation with cosmological MHD simulations). Secondly, our results provide an estimate of a flux of neutrinos and gamma rays from galaxy clusters that should be taken into account when interpreting the diffuse gamma-ray and neutrino background. It has immediate implications for all studies that depend on accurate estimates of this background, ranging from models of extragalactic high-energy gamma-ray sources to dark-matter searches.

In the first Chapter 1, we described the observational and theoretical motivation for this work. We also discussed the importance of our work in the larger context of multi-messenger astrophysics and particle astrophysics.

In Chapter 2, we presented a detailed analysis of the large scale background cosmo-

logical MHD simulations of the large scale structures and galaxy clusters employed here, using the SPH GADGET code (Dolag et al., 1999; Springel et al., 2001; Dolag et al., 2005). We discussed the properties of the galaxy clusters based on the simulations and presented 2D cuts of the distributions of the magnetic fields, density and temperature in simulated clusters of different masses. We found that the clusters have no spherical symmetric which can affect the emission pattern of the multi-messengers (CRs, photons and neutrinos) from these structures. The number density of clusters of different masses within the total volume of our cosmological simulation is comparable with the cosmological simulations Jenkins et al. (2001); Bocquet et al. (2016) and with the observations as well Tinker et al. (2008).

Chapter 3 was dedicated to discuss the propagation of CRs and the interaction processes. In the first part we described the Monte Carlo code CRPropa 3 (Alves Batista et al., 2016) that we employed here to investigate the propagation of CRs. We discussed both the ballistic and diffusive regimes of CRs depending on their energy and the background astrophysical environments. We argued that the SDE approach is more suitable to study the propagation of CRs in the turbulent ICM. In the second part of Chapter 3, we described all the relevant CR interaction rates of energy loss namely, photopion production, photodisintegration, nuclear decay, proton-proton (pp) interactions, and adiabatic losses. We also derived the rates of electromagnetic cascade processes of gamma rays including inverse Compton scattering, single, double, and triplet pair production. To see the importance of these processes we compared their mean free paths (MFPs) in the context of the ICM and intergalactic medium. In addition, we also discussed all the relevant photon fields in ICM/IGM, i.e., the CMB, EBL, and Bremsstrahlung. We found that the most important channel to produce high-energy photons and neutrinos in the ICM are inelastic proton-proton collisions and CRs interactions with the CMB.

The main results of this Thesis were presented in Chapters 4 and 5, on the production of high-energy neutrinos and gamma-rays, respectively, from the clusters of galaxies.

In Chapter 4, we presented the integrated flux of neutrinos from the entire population of clusters of galaxies in the redshift range $z \leq 5.0$ and mass range $10^{12} \lesssim M/M_{\odot} < 10^{16}$. We used the most rigorous numerical approach to take into account the non-uniformity of the gas density and magnetic field distributions in clusters, as obtained from 3D-MHD simulations. Our cosmological simulations indicate that the magnetic field and gas density

distributions in massive clusters (with $M > 10^{14}\ M_{\odot}$) are larger than in the lower-mass ones, and that massive clusters ($M > 10^{15}\ M_{\odot}$) are less abundant at high redshifts (Jenkins et al., 2001; Rosati et al., 2002; Hussain et al., 2021). The neutrino flux from clusters we obtained (see also Hussain et al., 2021) is comparable with observations by the IceCube Neutrino Observatory, especially between the energies 100 TeV and 10 PeV. Most of the contribution to the total flux comes from clusters at redshift $z \leq 0.3$ with masses $M \gtrsim 10^{14} M_{\odot}$. Furthermore, our results also predicted that the next generation of neutrino observatories (e.g., IceCube-Gen2) might be able to observe high-energy neutrinos from clusters.

In Chapter 5, we presented the contribution of clusters of galaxies to the observed diffuse gamma-ray background (DGRB). In that context, we used the same cosmological MHD simulations as in Chapter 4 in the same mass and redshift range to probe the background ICM. We computed the flux of gamma-rays arising from the cluster population and their cascading through the IGM until arrival in the Earth. We have found that the total gamma-ray flux from the clusters can contribute up to 100% of the diffuse gamma-ray flux above 100 GeV observed by the Fermi-LAT. The major contribution comes from clusters with mass $10^{13} < M/M_{\odot} < 10^{15}$ in the redshift range $z \leq 0.3$. Our results are also comparable with the upper limits of HAWC at very high energies of the DGRB.

A final remark is in order, an important aspect that differed a little in the computation of both diffuse fluxes of neutrinos and gamma rays, was the assumed power of injected CRs inside the clusters, which is a free-parameter in our simulations, barely constrained by observations. In the case of the neutrino study (Chapter 4), we injected a CR power with $(0.5 - 3)\%$ of the cluster luminosity, while in the case of the gamma-rays (Chapter 5), we considered a fraction of 1%, which we found to be more than enough to reproduce the observed emission by the Femri-LAT. Also remarkable is the fact that while the flux of neutrinos is dominated by contributions from more massive clusters, the flux of gamma rays has also important contribution from less massive ones. This means that the luminosity fraction that is injected in the CRs that will produce the observed neutrino flux does not have to be the same as the one that will produce the observed DGRB. A better constraint of this parameter will be provided by confronting our predictions with observations of the forthcoming observatories and experiments.

At last, we summarize our results in Fig. 6.1, the high-energy fluxes of gamma-rays and

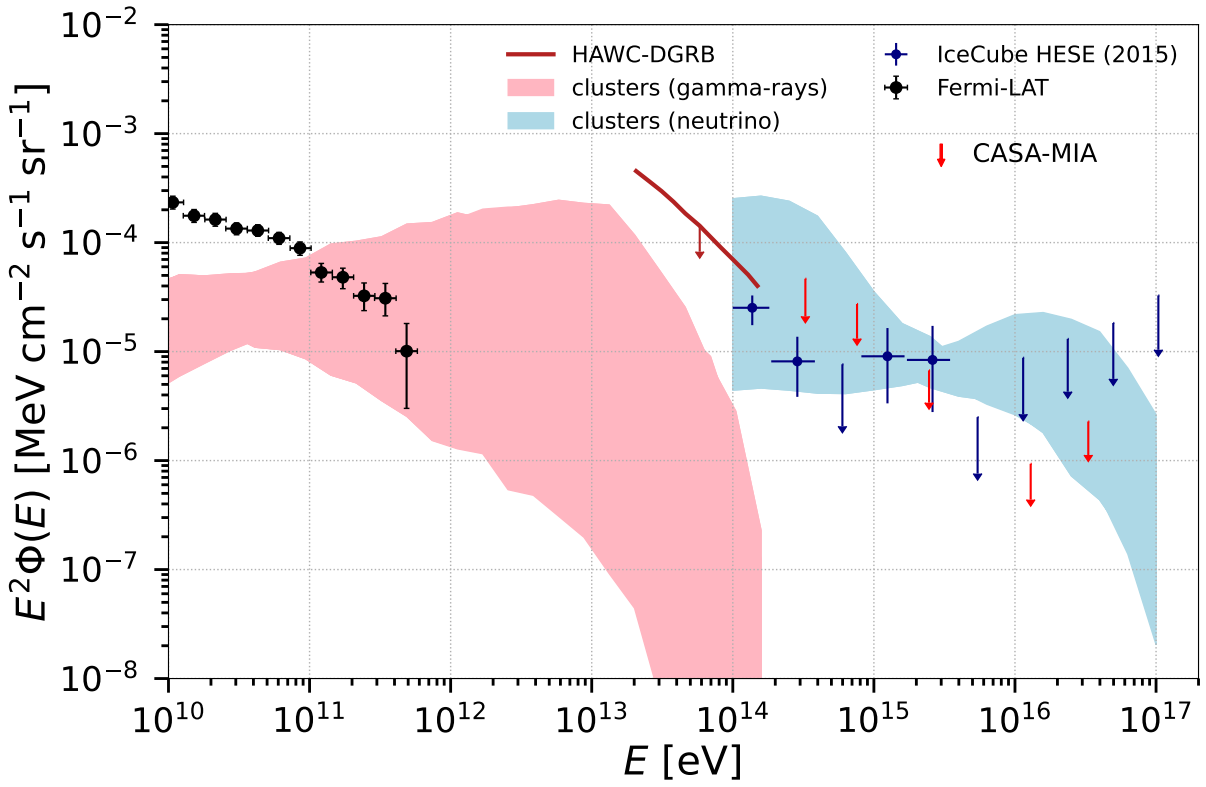

Figure 6.1: High-energy neutrinos (blue band) and gamma-rays (pink band) from the entire population of galaxy clusters obtained in this work. We compare the gamma-ray flux with the DGRB observed by Fermi-LAT (Ackermann et al., 2015), and the upper limits from HAWC (Harding, 2019) and CASA-MIA (Chantell et al., 1997). We also compare the neutrino flux with the diffuse neutrino background observed by IceCube (Aartsen et al., 2015).

neutrinos from clusters are comparable with the DGRB (observed by Fermi-LAT above energy 5×10^{11} eV) and the diffuse neutrino background (observed by IceCube above energy 10^{14} eV), which makes them very attractive candidates for the observations of these high-energy multi-messengers.

6.2 Future Perspectives

The results of this work open new window for the search of multi-messengers especially high-energy neutrinos and gamma-rays from clusters of galaxies. These cosmic messengers provide us information about their sources and the properties of intergalactic medium.

Our results are based on the non-radiative MHD simulations that did not consider the radiative-cooling, or the amount of gas that is converted into stars or removed from the clusters due to stellar and AGN feedback. The most immediate research work that

can be done in this direction is to consider more realistic background MHD simulations that account for the sources evolution such as SFR and AGN-feedback (e.g., Barai and de Gouveia Dal Pino, 2019; Hopkins et al., 2021) which will allow us to constrain better the contribution of clusters to the neutrinos and DGRB.

Another obvious channel, is to explore further the effects of CR chemical compositions on the neutrino and DGRB fluxes. In the present study, we focused on the most abundant component, the protons. If there are heavier nuclei in clusters, then they should be subdominant with respect to protons because the CR acceleration depends on the rigidity (energy over charge). Even though, we expect a much smaller contribution from heavier elements (see e.g., Kotera et al., 2009), it will be straightforward to perform similar simulations as those carried out here combining the cosmological with Monte Carlo simulations, in order to quantify these contributions. In this context, we did a preliminary study where we computed the flux for three different primary composition Fe, N, p of CRs, from two individual clusters which are presented in the Appendix D.

Employing similar methods as those applied in this Thesis, we can also explore the MWL emission by modeling the reacceleration and propagation of CR protons and electrons from individual sources like Virgo, Centaurus, Perseus, Coma cluster (e.g., Nishiwaki et al., 2021). Our results also indicate that the distribution of magnetic field and density in clusters deviate from spherical symmetry. Though it does not affect the high-energy emissions too much, it may affect largely the low energy emission such as in the radio halo of the clusters which is commonly attributed to synchrotron emission.

In galaxy clusters, the most prominent processes that can produce high-energy particles in turbulent media is diffusive shock acceleration, and magnetic reconnection also appears as a powerful candidate particularly for reacceleration in the turbulent environment (Hillas, 1984; Berezinsky et al., 1997; Murase et al., 2008; Pfrommer, 2008; Pinzke and Pfrommer, 2010; Lazarian et al., 2012; Kowal et al., 2012; Blasi, 2013; Murase et al., 2013; de Gouveia Dal Pino and Kowal, 2015; Bonafede et al., 2021; Brunetti and Jones, 2014; Brunetti et al., 2017). CRs are present in galaxies and clusters with an approximate equipartition to the thermal turbulent gas and magnetic energy densities that can have a significant impact on the interstellar medium (ISM) and ICM, through the dynamical coupling between gas and CRs. These CRs can heat up the gas in galaxies. Being of non thermal nature, CRs do not cool quickly as compared to the gas which allow them to escape from the disc of galaxies.

The escaping of CRs produce a gradient of pressure which can create a gas outflows from the galactic discs. This process is responsible for launching the galactic-scale winds and quenching the star-formation by the removal of gas (Hopkins et al., 2020). Therefore, CRs coupled with magnetic field are crucial to understand the dynamics of gas in galaxies and clusters. More importantly, they can play a central role in the evolution of galaxies. We can also study the evolution of these sources that host AGN jets composed of CRs and magnetic field, with the same tools we have employed here.

Apparently, black hole jets embedded in large-scale structures (e.g., galaxies and clusters) are the major contributor in the production of multi-frequency cosmic particles and the evolution of these sources. Thus, to probe the multi-messenger and MWL emission from galaxies and clusters, the study of AGN jets (e.g., blazars) have antic importance. The spectra of blazars are fully dominated by the jet emission, so we can model these jets and accretion flow through the MHD or general-relativistic (GR) MHD simulations (de Gouveia Dal Pino et al., 2020; Medina-Torrejon et al., 2021; Kadowaki et al., 2021). The emission of non-thermal radiation over the whole electromagnetic spectrum from blazars is commonly explained due to synchrotron emission, inverse Compton scattering, and subdominant hadronic interactions. With these background environments (MHD or GR-MHD) combined with Monte Carlo simulations, we can constrain the MWL emission from blazars, especially HE neutrinos and gamma-rays because they are among the brightest gamma-ray sources in the sky (Ackermann et al., 2015; Rodríguez-Ramírez et al., 2019; Alves Batista and Saveliev, 2021). By modeling the time-dependent blazar jets, we can also investigate the spectral lags (the time delays between photons of different energies) that can arise in acceleration and emission patterns, employing the same combination of MHD and Monte Carlo particle simulation techniques used in the present work.

We did not consider the effect of axion-like particles (ALPs) while estimating the gamma-ray flux from clusters of galaxies. ALPs are hypothetical particles predicted by several theories beyond the standard model, especially by the string theory Witten (1984); Conlon (2006); Ringwald (2012); Cicoli et al. (2012). These particles can be one of the best candidates to account for dark matter (Alonso-Alvarez et al., 2020). Several studies constrained the ALPs through a detailed Chandra spectroscopic analysis of clusters hosting AGNs Marsh et al. (2017); Berg et al. (2017); Reynolds et al. (2020); Schallmoser et al. (2021); Sisk-Reynés et al. (2022). Coupling of ALPs with photons in a magnetized

plasma like in galaxy clusters can modulate the X-ray and gamma-ray spectra from these sources (Sisk-Reynés et al., 2022). This modulation effect can appear either in the form of flux excess or distortion of spectra or both (Galanti et al., 2022). Also, the absorption of high-energy photons ($\gtrsim 10^{12}$ eV) by EBL can be avoided by the inter-conversion of photon and ALPs (Raffelt and Stodolsky, 1988; Reesman and Walker, 2014; Harris and Chadwick, 2014; Galanti et al., 2020)

This is one of the future endeavors to study the emission of gamma-rays from galaxy clusters including the effect of ALPs.

In summary, there are many important open issues to be further explored and constrained in the context of the propagation of CRs and their secondaries from large scale structures in which we can apply the methodology and results described in this work. These issues include:

- What is the actual distribution and composition of CRs in the ICM?
- What are the real effects of SFR and AGN feedback on the galaxy clusters evolutions and how they affect the CR, gamma-ray and neutrino flux?
- What is maximum energy that can be achieved by CRs in the clusters of galaxies?
- What is the contribution to the emission of gamma rays in galaxy clusters?
- What are the acceleration mechanisms that produce UHECRs?
- What is the role of CRs and magnetic fields, in the evolution of clusters of galaxies?
- Will the predictions and constraints on the diffusive gamma-ray and neutrino fluxes from galaxy clusters provided in this Thesis be confirmed by forthcoming observatories such as CTA and LHAASO for gamma-rays and IceCube-Gen2 and GRAND for extragalactic neutrinos?

Finally we would say, there is no end in sight for the work of multi-messenger and MWL study of astrophysical sources, a pleasant prospect for any science, and for me in particular.

Bibliography

Aab A., Abreu P., Aglietta M., Ahn E., Al Samarai I., Albuquerque I., Allekotte I., Allen J., Allison P., Almela A., et al., Depth of maximum of air-shower profiles at the Pierre Auger Observatory. II. Composition implications, Physical Review D, 2014, vol. 90, p. 122006

Aab A., Abreu P., Aglietta M., Ahn E., Al Samarai I., Albuquerque I., Allekotte I., Allen J., Allison P., Almela A., et al., Searches for anisotropies in the arrival directions of the highest energy cosmic rays detected by the Pierre Auger Observatory, The Astrophysical Journal, 2015, vol. 804, p. 15

Aab A., Abreu P., Aglietta M., Ahn E., Al Samarai I., Albuquerque I., Allekotte I., Allison P., Almela A., Castillo J. A., et al., Evidence for a mixed mass composition at the 'ankle' in the cosmic-ray spectrum, Physics Letters B, 2016, vol. 762, p. 288

Aab A., Abreu P., Aglietta M., Al Samarai I., Albuquerque I., Allekotte I., Almela A., Castillo J. A., Alvarez-Muñiz J., Anastasi G., et al., Combined fit of spectrum and composition data as measured by the Pierre Auger Observatory, Journal of Cosmology and Astroparticle Physics, 2017, vol. 2017, p. 038

Aab A., Abreu P., Aglietta M., Albuquerque I., Albury J. M., Allekotte I., Almela A., Castillo J. A., Alvarez-Muñiz J., Anastasi G. A., et al., Large-scale cosmic-ray anisotropies above 4 EeV measured by the Pierre Auger Observatory, The Astrophysical Journal, 2018, vol. 868, p. 4

Aab A., Abreu P., Aglietta M., Albury J. M., Allekotte I., Almela A., Castillo J. A., Alvarez-Muñiz J., Alves Batista R., Anastasi G. A., et al., Features of the Energy

Spectrum of Cosmic Rays above 2.5× 10 18 eV Using the Pierre Auger Observatory, Physical review letters, 2020, vol. 125, p. 121106

Aaboud M., Aad G., Abbott B., Abdallah J., Abeloos B., Aben R., AbouZeid O., Abraham N., Abramowicz H., Abreu H., et al., Measurement of the Inelastic Proton-Proton Cross Section at s= 13 TeV with the ATLAS Detector at the LHC, Physical review letters, 2016, vol. 117, p. 182002

Aartsen M., Abraham K., Ackermann M., Adams J., Aguilar J., Ahlers M., Ahrens M., Altmann D., Andeen K., Anderson T., et al., the contribution of FERMI-2LAC blazars to diffuse TeV–PeV neutrino flux, The Astrophysical Journal, 2017, vol. 835, p. 45

Aartsen M., Ackermann M., Adams J., Aguilar J., Ahlers M., Ahrens M., Alispach C., Andeen K., Anderson T., Ansseau I., et al., Time-integrated neutrino source searches with 10 years of IceCube data, Physical review letters, 2020, vol. 124, p. 051103

Aartsen M., Ackermann M., Adams J., Aguilar J., Ahlers M., Ahrens M., Altmann D., Anderson T., Arguelles C., Arlen T., et al., Atmospheric and astrophysical neutrinos above 1 TeV interacting in IceCube, Physical Review D, 2015, vol. 91, p. 022001

Aartsen M. G., Abbasi R., Abdou Y., Ackermann M., Adams J., Aguilar J., Ahlers M., Altmann D., Auffenberg J., Bai X., et al., First observation of PeV-energy neutrinos with IceCube, Physical review letters, 2013, vol. 111, p. 021103

Abbasi R., Abu-Zayyad T., Al-Seady M., Allen M., Amman J., Anderson R., Archbold G., Belov K., Belz J., Bergman D., et al., Indications of proton-dominated cosmic-ray composition above 1.6 EeV, Physical Review Letters, 2010, vol. 104, p. 161101

Abbasi R., Abu-Zayyad T., Archbold G., Atkins R., Bellido J., Belov K., Belz J., BenZvi S., Bergman D., Boyer J., et al., A study of the composition of ultra-high-energy cosmic rays using the high-resolution fly's eye, The astrophysical journal, 2005, vol. 622, p. 910

Abeysekara A., Alfaro R., Alvarez C., Álvarez J., Arceo R., Arteaga-Velázquez J., Solares H. A., Barber A., Baughman B., Bautista-Elivar N., et al., Sensitivity of the high altitude water Cherenkov detector to sources of multi-TeV gamma rays, Astroparticle Physics, 2013, vol. 50, p. 26

Ackermann M., Ahlers M., Anchordoqui L., Bustamante M., Connolly A., Deaconu C., Grant D., Gorham P., Halzen F., Karle A., et al., Astrophysics uniquely enabled by observations of high-energy cosmic neutrinos, arXiv preprint arXiv:1903.04334, 2019

Ackermann M., Ajello M., Albert A., Allafort A., Atwood W., Baldini L., Ballet J., Barbiellini G., Bastieri D., Bechtol K., et al., Search for cosmic-ray-induced gamma-ray emission in galaxy clusters, The Astrophysical Journal, 2014, vol. 787, p. 18

Ackermann M., Ajello M., Albert A., Atwood W., Baldini L., Ballet J., Barbiellini G., Bastieri D., Bechtol K., Bellazzini R., et al., The spectrum of isotropic diffuse gamma-ray emission between 100 MeV and 820 GeV, The Astrophysical Journal, 2015, vol. 799, p. 86

Ackermann M., Ajello M., Atwood W., Baldini L., Ballet J., Barbiellini G., Bastieri D., Bechtol K., Bellazzini R., Berenji B., et al., Fermi-LAT observations of the diffuse γ-ray emission: implications for cosmic rays and the interstellar medium, The Astrophysical Journal, 2012, vol. 750, p. 3

Ackermann M., Ajello M., Atwood W., Baldini L., Barbiellini G., Bastieri D., Bechtol K., Bellazzini R., Blandford R., Bloom E., et al., Constraints on the galactic halo dark matter from Fermi-LAT diffuse measurements, The Astrophysical Journal, 2012, vol. 761, p. 91

Ade P. A., Aghanim N., Armitage-Caplan C., Arnaud M., Ashdown M., Atrio-Barandela F., Aumont J., Baccigalupi C., Banday A. J., Barreiro R., et al., Planck 2013 results. XVI. Cosmological parameters, Astronomy & Astrophysics, 2014, vol. 571, p. A16

Aharonian F., Akhperjanian A., Anton G., De Almeida U. B., Bazer-Bachi A., Becherini Y., Behera B., Bernlöhr K., Boisson C., Bochow A., et al., Constraints on the multi-TeV particle population in the Coma galaxy cluster with HESS observations, Astronomy & Astrophysics, 2009, vol. 502, p. 437

Aharonian F., Akhperjanian A., Bazer-Bachi A., Beilicke M., Benbow W., Berge D., Bernlöhr K., Boisson C., Bolz O., Borrel V., et al., A low level of extragalactic background light as revealed by γ-rays from blazars, Nature, 2006, vol. 440, p. 1018

Aharonian F., Atoyan A., Cosmic ray positrons connected with galactic gamma radiation of high and very high energies, Journal of Physics G: Nuclear and Particle Physics, 1991, vol. 17, p. 1769

Aharonian F., Belyanin A., Derishev E., Kocharovsky V., Kocharovsky V. V., Constraints on the extremely high-energy cosmic ray accelerators from classical electrodynamics, Physical Review D, 2002, vol. 66, p. 023005

Aharonian F., et al., HESS collaboration, Nature, 2006, vol. 440, p. 1018

Aharonian F. A., Very high energy cosmic gamma radiation: a crucial window on the extreme Universe. World Scientific, 2004

Ahlers M., Denton P., Rameez M., Analyzing UHECR arrival directions through the Galactic magnetic field in view of the local universe as seen in 2MRS, PoS (ICRC2017), 2018, vol. 282

Ahlers M., Halzen F., Opening a new window onto the universe with IceCube, Progress in Particle and Nuclear Physics, 2018, vol. 102, p. 73

Ahn H., Allison P., Bagliesi M., Barbier L., Beatty J., Bigongiari G., Brandt T., Childers J., Conklin N., Coutu S., et al., Energy spectra of cosmic-ray nuclei at high energies, The Astrophysical Journal, 2009, vol. 707, p. 593

Ajello M., Gasparrini D., Sánchez-Conde M., Zaharijas G., Gustafsson M., Cohen-Tanugi J., Dermer C., Inoue Y., Hartmann D., Ackermann M., et al., The origin of the extragalactic gamma-ray background and implications for dark matter annihilation, The Astrophysical Journal Letters, 2015, vol. 800, p. L27

Albert A., Alvarez C., Camacho J. A., Arteaga-Velázquez J., Arunbabu K., Rojas D. A., Solares H. A., Baghmanyan V., Belmont-Moreno E., BenZvi S., et al., A survey of active galaxies at TeV photon energies with the HAWC gamma-ray observatory, The Astrophysical Journal, 2021, vol. 907, p. 67

Albert A., André M., Anghinolfi M., Anton G., Ardid M., Aubert J.-J., Aublin J., Avgitas T., Baret B., Barrios-Martí J., et al., The Search for Neutrinos from TXS 0506+ 056

with the ANTARES Telescope, The Astrophysical Journal Letters, 2018, vol. 863, p. L30

Aloisio R., Berezinsky V., Blasi P., Ultra high energy cosmic rays: implications of Auger data for source spectra and chemical composition, Journal of Cosmology and Astroparticle Physics, 2014, vol. 2014, p. 020

Aloisio R., Berezinsky V., Gazizov A., Ultra high energy cosmic rays: The disappointing model, Astroparticle Physics, 2011, vol. 34, p. 620

Aloisio R., Berezinsky V., Gazizov A., Transition from galactic to extragalactic cosmic rays, Astroparticle Physics, 2012, vol. 39, p. 129

Aloisio R., Boncioli D., Di Matteo A., Grillo A. F., Petrera S., Salamida F., SimProp v2r4: Monte Carlo simulation code for UHECR propagation, Journal of Cosmology and Astroparticle Physics, 2017, vol. 2017, p. 009

Aloisio R., Boncioli D., Grillo A., Petrera S., Salamida F., SimProp: a simulation code for ultra high energy cosmic ray propagation, Journal of Cosmology and Astroparticle Physics, 2012, vol. 2012, p. 007

Alonso-Alvarez G., Gupta R. S., Jaeckel J., Spannowsky M., On the wondrous stability of ALP dark matter, Journal of Cosmology and Astroparticle Physics, 2020, vol. 2020, p. 052

Álvarez-Muñiz J., Alves Batista R., Bolmont J., Bustamante M., Carvalho W., Charrier D., Cognard I., Decoene V., Denton P. B., De Jong S., et al., The giant radio array for neutrino detection (GRAND): science and design, Science China Physics, Mechanics & Astronomy, 2020, vol. 63, p. 219501

Alves Batista R., On the cosmological propagation of high energy particles in magnetic fields, Staats-und Universitätsbibliothek Hamburg, 2015, Ph.D. Thesis

Alves Batista R., Biteau J., Bustamante M., Dolag K., Engel R., Fang K., Kampert K.-H., Kostunin D., Mostafa M., Murase K., et al., Open questions in cosmic-ray research at ultrahigh energies, Frontiers in Astronomy and Space Sciences, 2019, vol. 6, p. 23

Alves Batista R., De Almeida R. M., Lago B., Kotera K., Cosmogenic photon and neutrino fluxes in the Auger era, Journal of Cosmology and Astroparticle Physics, 2019, vol. 2019, p. 002

Alves Batista R., de Gouveia Dal Pino E. M., Dolag K., Hussain S., Cosmic-ray propagation in the turbulent intergalactic medium, arXiv preprint arXiv:1811.03062, 2018

Alves Batista R., Dundovic A., Erdmann M., Kampert K.-H., Kuempel D., Mueller G., Sigl G., van Vliet A., Walz D., Winchen T., CRPropa 3-a public astrophysical simulation framework for propagating extraterrestrial ultra-high energy particles, Journal of Cosmology and Astroparticle Physics, 2016, vol. 2016, p. 038

Alves Batista R., Erdmann M., Evoli C., Kampert K.-H., Kuempel D., Mueller G., Sigl G., Van Vliet A., Walz D., Winchen T., Cosmic ray propagation with CRPropa 3. In Journal of Physics: Conference Series , vol. 608, 2015, p. 012076

Alves Batista R., Erdmann M., Evoli C., Kampert K.-H., Kuempel D., Müller G., Schiffer P., Sigl G., van Vliet A., Walz D., et al., CRPropa 3.0-a public framework for propagating UHE cosmic rays through galactic and extragalactic space, arXiv preprint arXiv:1307.2643, 2013

Alves Batista R., Saveliev A., The Gamma-Ray Window to Intergalactic Magnetism, Universe, 2021, vol. 7, p. 223

Alves Batista R., Shin M.-S., Devriendt J., Semikoz D., Sigl G., Implications of strong intergalactic magnetic fields for ultrahigh-energy cosmic-ray astronomy, Physical Review D, 2017, vol. 96, p. 023010

Alves Batista R., Silk J., Ultrahigh-energy cosmic rays from tidally-ignited white dwarfs, Physical Review D, 2017, vol. 96, p. 103003

Amato E., Blasi P., Cosmic ray transport in the Galaxy: A review, Advances in Space Research, 2018, vol. 62, p. 2731

Ambrosone A., Chianese M., Fiorillo D. F., Marinelli A., Miele G., Could Nearby Star-forming Galaxies Light Up the Pointlike Neutrino Sky?, The Astrophysical Journal Letters, 2021, vol. 919, p. L32

Anchordoqui L. A., Acceleration of ultrahigh-energy cosmic rays in starburst superwinds, Physical Review D, 2018, vol. 97, p. 063010

Anchordoqui L. A., Paul T. C., da Silva L. H., Torres D. F., Vlcek B. J., What IceCube data tell us about neutrino emission from star-forming galaxies (so far), Physical Review D, 2014, vol. 89, p. 127304

Anchordoqui L. A., Soriano J. F., Evidence for UHECR origin in starburst galaxies, arXiv preprint arXiv:1905.13243, 2019

Anjos R., Coimbra-Araújo C., Central accumulation of magnetic flux in massive Seyfert galaxies as a possible engine to trigger ultrahigh energy cosmic rays, Physical Review D, 2017, vol. 96, p. 023008

Ansoldi S., Antonelli L. A., Arcaro C., Baack D., Babić A., Banerjee B., Bangale P., De Almeida U. B., Barrio J. A., González J. B., et al., The Blazar TXS 0506+ 056 Associated with a High-energy Neutrino: Insights into Extragalactic Jets and Cosmic-Ray Acceleration, The Astrophysical Journal Letters, 2018, vol. 863, p. L10

Apel W., Arteaga J., Bekk K., Bertaina M., Blümer J., Bozdog H., Brancus I., Buchholz P., Büttner C., Cantoni E., et al., Muon production height studies with the air shower experiment KASCADE-Grande, Astroparticle Physics, 2011, vol. 34, p. 476

Apel W., Arteaga-Velazquez J., Bekk K., Bertaina M., Bluemer J., Bozdog H., Brancus I., Cantoni E., Chiavassa A., Cossavella F., et al., The KASCADE-Grande energy spectrum of cosmic rays and the role of hadronic interaction models, Advances in Space Research, 2014, vol. 53, p. 1456

Apel W., Arteaga-Velázquez J., Bekk K., Bertaina M., Blümer J., Bozdog H., Brancus I., Cantoni E., Chiavassa A., Cossavella F., et al., KASCADE-Grande measurements of energy spectra for elemental groups of cosmic rays, Astroparticle Physics, 2013, vol. 47, p. 54

Arámburo-García A., Bondarenko K., Boyarsky A., Nelson D., Pillepich A., Sokolenko A., Ultrahigh energy cosmic ray deflection by the intergalactic magnetic field, Physical Review D, 2021, vol. 104, p. 083017

Arteaga-Velázquez J., Apel W., Bekk K., Bertaina M., Blümer J., Bozdog H., Brancus I., Cantoni E., Chiavassa A., Cossavella F., et al., The KASCADE-Grande observatory and the composition of very high-energy cosmic rays. In Journal of Physics: Conference Series , vol. 651, 2015, p. 012001

Arteaga-Velázquez J., Apel W., Bekk K., Bertaina M., Blümer J., Bozdog H., Brancus I., Cantoni E., Chiavassa A., Cossavella F., et al., Muon density measurements for the light and heavy mass groups of cosmic rays at the KASCADE-Grande observatory, Nuclear and particle physics proceedings, 2017, vol. 291, p. 152

Auger-Collaboration o., The Pierre Auger cosmic ray observatory, Nuclear Instruments and Methods in Physics Research Section A: Accelerators, Spectrometers, Detectors and Associated Equipment, 2015, vol. 798, p. 172

Baade W., Zwicky F., Cosmic rays from super-novae, Proceedings of the National Academy of Sciences, 1934, vol. 20, p. 259

Barai P., de Gouveia Dal Pino E. M., Intermediate-mass black hole growth and feedback in dwarf galaxies at high redshifts, Monthly Notices of the Royal Astronomical Society, 2019, vol. 487, p. 5549

Beresnyak A., Particle acceleration in MHD turbulence. In Journal of Physics: Conference Series , vol. 837, 2017, p. 012001

Berezinsky V., On transiton from galactic to extragalactic cosmic rays. In Journal of Physics: Conference Series , vol. 47, 2006, p. 018

Berezinsky V., Gazizov A., Diffusion of Cosmic Rays in the Expanding Universe. I., The Astrophysical Journal, 2006, vol. 643, p. 8

Berezinsky V. S., Blasi P., Ptuskin V., Clusters of galaxies as storage room for cosmic rays, The Astrophysical Journal, 1997, vol. 487, p. 529

Berg M., Conlon J. P., Day F., Jennings N., Krippendorf S., Powell A. J., Rummel M., Constraints on axion-like particles from X-ray observations of NGC1275, The Astrophysical Journal, 2017, vol. 847, p. 101

Blandford R., Eichler D., Particle acceleration at astrophysical shocks: A theory of cosmic ray origin, Physics Reports, 1987, vol. 154, p. 1

Blandford R., Simeon P., Yuan Y., Cosmic ray origins: an introduction, Nuclear Physics B-proceedings supplements, 2014, vol. 256, p. 9

Blasi P., The origin of galactic cosmic rays, The Astronomy and Astrophysics Review, 2013, vol. 21, p. 70

Blasi P., Gabici S., Brunetti G., Gamma rays from clusters of galaxies, International Journal of Modern Physics A, 2007, vol. 22, p. 681

Blumenthal G. R., Energy loss of high-energy cosmic rays in pair-producing collisions with ambient photons, Physical review D, 1970, vol. 1, p. 1596

Bocquet S., Saro A., Dolag K., Mohr J. J., Halo mass function: baryon impact, fitting formulae, and implications for cluster cosmology, Monthly Notices of the Royal Astronomical Society, 2016, vol. 456, p. 2361

Boldyrev S., Cattaneo F., Magnetic-field generation in Kolmogorov turbulence, Physical Review Letters, 2004, vol. 92, p. 144501

Bonafede A., Brüggen M., van Weeren R., Vazza F., Giovannini G., Ebeling H., Edge A., Hoeft M., Klein U., Discovery of radio haloes and double relics in distant MACS galaxy clusters: clues to the efficiency of particle acceleration, Monthly Notices of the Royal Astronomical Society, 2012, vol. 426, p. 40

Bonafede A., Brunetti G., Vazza F., Simionescu A., Giovannini G., Bonnassieux E., Shimwell T., Brüggen M., van Weeren R., Botteon A., et al., The Coma Cluster at LOw Frequency ARray Frequencies. I. Insights into Particle Acceleration Mechanisms in the Radio Bridge, The Astrophysical Journal, 2021, vol. 907, p. 32

Bovino S., Schleicher D. R., Schober J., Turbulent magnetic field amplification from the smallest to the largest magnetic Prandtl numbers, New Journal of Physics, 2013, vol. 15, p. 013055

Brown R., Hunt W., Mikaelian K., Muzinich I., Role of $\gamma+ \gamma \rightarrow$ e++ e-+ e++ e- in photoproduction, colliding beams, and cosmic photon absorption, Physical Review D, 1973, vol. 8, p. 3083

Brunetti G., Cassano R., Dolag K., Setti G., On the evolution of giant radio halos and their connection with cluster mergers, Astronomy & Astrophysics, 2009, vol. 507, p. 661

Brunetti G., Giacintucci S., Cassano R., Lane W., Dallacasa D., Venturi T., Kassim N., Setti G., Cotton W., Markevitch M., A low-frequency radio halo associated with a cluster of galaxies, Nature, 2008, vol. 455, p. 944

Brunetti G., Jones T. W., Cosmic rays in galaxy clusters and their nonthermal emission, International Journal of Modern Physics D, 2014, vol. 23, p. 1430007

Brunetti G., Lazarian A., Compressible turbulence in galaxy clusters: physics and stochastic particle re-acceleration, Monthly Notices of the Royal Astronomical Society, 2007, vol. 378, p. 245

Brunetti G., Vazza F., Second-order Fermi Reacceleration Mechanisms and Large-Scale Synchrotron Radio Emission in Intracluster Bridges, Physical Review Letters, 2020, vol. 124, p. 051101

Brunetti G., Zimmer S., Zandanel F., Relativistic protons in the Coma galaxy cluster: first gamma-ray constraints ever on turbulent reacceleration, Monthly Notices of the Royal Astronomical Society, 2017, vol. 472, p. 1506

Buckman B. J., Linden T., Thompson T. A., Cosmic rays and magnetic fields in the core and halo of the starburst M82: implications for galactic wind physics, Monthly Notices of the Royal Astronomical Society, 2020, vol. 494, p. 2679

Buitink S., Corstanje A., Falcke H., Hörandel J., Huege T., Nelles A., Rachen J., Rossetto L., Schellart P., Scholten O., et al., A large light-mass component of cosmic rays at 1017–1017.5 electronvolts from radio observations, Nature, 2016, vol. 531, p. 70

Caprioli D., Spitkovsky A., Simulations of ion acceleration at non-relativistic shocks. I. Acceleration efficiency, The Astrophysical Journal, 2014, vol. 783, p. 91

Cash J. R., Karp A. H., A variable order Runge-Kutta method for initial value problems with rapidly varying right-hand sides, ACM Transactions on Mathematical Software (TOMS), 1990, vol. 16, p. 201

Cassano R., Ettori S., Giacintucci S., Brunetti G., Markevitch M., Venturi T., Gitti M., On the connection between giant radio halos and cluster mergers, The Astrophysical Journal Letters, 2010, vol. 721, p. L82

Castelvecchi D., High-energy cosmic rays come from outside our Galaxy, Nature News, 2017, vol. 549, p. 440

Cerruti M., Benbow W., Chen X., Dumm J. P., Fortson L., Shahinyan K., Luminous and high-frequency peaked blazars: the origin of the γ-ray emission from PKS 1424+ 240, Astronomy & Astrophysics, 2017, vol. 606, p. A68

Chakraborty S., Izaguirre I., Diffuse neutrinos from extragalactic supernova remnants: Dominating the 100 TeV IceCube flux, Physics Letters B, 2015, vol. 745, p. 35

Chantell M., Covault C., Cronin J., Fick B., Fortson L., Fowler J., Green K., Newport B., Ong R., Oser S., et al., Limits on the isotropic diffuse flux of ultrahigh energy γ radiation, Physical review letters, 1997, vol. 79, p. 1805

Chodorowski M. J., Zdziarski A. A., Sikora M., Reaction rate and energy-loss rate for photopair production by relativistic nuclei, The Astrophysical Journal, 1992, vol. 400, p. 181

Cicoli M., Goodsell M. D., Ringwald A., The type IIB string axiverse and its low-energy phenomenology, Journal of High Energy Physics, 2012, vol. 2012, p. 1

Colafrancesco S., Blasi P., Clusters of galaxies and the diffuse gamma-ray background, Astroparticle Physics, 1998, vol. 9, p. 227

Conlon J. P., Seeing an invisible axion in the supersymmetric particle spectrum, Physical review letters, 2006, vol. 97, p. 261802

CTA Acharya B., Science with the Cherenkov Telescope Array. World Scientific, 2018

D'Amato Q., Gilli R., Vignali C., Massardi M., Pozzi F., Zamorani G., Circosta C., Vito F., Fritz J., Cresci G., et al., Dust and gas content of high-redshift galaxies hosting obscured AGN in the Chandra Deep Field-South, Astronomy & Astrophysics, 2020, vol. 636, p. A37

Das S., Razzaque S., Gupta N., Modeling the spectrum and composition of ultrahigh-energy cosmic rays with two populations of extragalactic sources, The European Physical Journal C, 2021, vol. 81, p. 1

De Domenico M., Lyberis H., Settimo M., HERMES: a Monte Carlo Code for the Propagation of Ultra-High Energy Nuclei, arXiv preprint arXiv:1307.4356, 2013

de Gouveia Dal Pino E. M., Kowal G., , 2015 in , Magnetic Fields in Diffuse Media. Springer pp 373–398

de Gouveia Dal Pino E. M., Kowal G., Kadowaki L., Medina-Torrejón T. E., Mizuno Y., Singh C., Particle acceleration and the origin of the very high energy emission around black holes and relativistic jets, Proceedings of the International Astronomical Union, 2020, vol. 14, p. 13

de Gouveia Dal Pino E. M., Lazarian A., Ultra-high-energy cosmic-ray acceleration by magnetic reconnection in newborn accretion-induced collapse pulsars, The Astrophysical Journal Letters, 2000, vol. 536, p. L31

Dembinski H., The Muon Puzzle in high-energy air showers, Physics of Atomic Nuclei, 2019, vol. 82, p. 644

di Matteo A., Anchordoqui L., Bister T., Biteau J., Caccianiga L., de Almeida R., Deligny O., Giaccari U., Harari D., Kim J., et al., UHECR arrival directions in the latest data from the original Auger and TA surface detectors and nearby galaxies, arXiv preprint arXiv:2111.12366, 2021

Di Mauro M., Calore F., Donato F., Ajello M., Latronico L., Diffuse γ-ray emission from misaligned active galactic nuclei, The Astrophysical Journal, 2013, vol. 780, p. 161

Di Mauro M., Donato F., Composition of the Fermi-LAT isotropic gamma-ray background intensity: Emission from extragalactic point sources and dark matter annihilations, Physical Review D, 2015, vol. 91, p. 123001

Di Sciascio G., Collaboration L., et al., The LHAASO experiment: from gamma-ray astronomy to cosmic rays, Nuclear and particle physics proceedings, 2016, vol. 279, p. 166

Di Sciascio G., Iuppa R., On the Observation of the Cosmic Ray Anisotropy below 10^{15} eV, arXiv preprint arXiv:1407.2144, 2014

Dicke R. H., Peebles P. J. E., Roll P. G., Wilkinson D. T., Cosmic black-body radiation., The Astrophysical Journal, 1965, vol. 142, p. 414

Dolag K., Bartelmann M., Lesch H., SPH simulations of magnetic fields in galaxy clusters, arXiv preprint astro-ph/9906329, 1999

Dolag K., Bartelmann M., Lesch H., Evolution and structure of magnetic fields in simulated galaxy clusters, Astronomy & Astrophysics, 2002, vol. 387, p. 383

Dolag K., Grasso D., Springel V., Tkachev I., Mapping deflections of extragalactic ultra high energy cosmic rays in magnetohydrodynamic simulations of the local universe, Nuclear Physics B-Proceedings Supplements, 2004, vol. 136, p. 234

Dolag K., Grasso D., Springel V., Tkachev I., Constrained simulations of the magnetic field in the local Universe and the propagation of ultrahigh energy cosmic rays, Journal of Cosmology and Astroparticle Physics, 2005, vol. 2005, p. 009

Dolag K., Kachelrieß M., Semikoz D., UHECR observations and lensing in the magnetic field of the Virgo cluster, Journal of Cosmology and Astroparticle Physics, 2009, vol. 2009, p. 033

Dominguez A., Primack J. R., Rosario D., Prada F., Gilmore R., Faber S. M., Koo D. C., Somerville R. S., Pérez-Torres M., Perez-Gonzalez P., et al., Extragalactic background light inferred from AEGIS galaxy-SED-type fractions, Monthly Notices of the Royal Astronomical Society, 2011, vol. 410, p. 2556

Edge A., Stewart G., EXOSAT observations of clusters of galaxies–I. the X-ray data, Monthly Notices of the Royal Astronomical Society, 1991, vol. 252, p. 414

Evoli C., Gaggero D., Vittino A., Di Bernardo G., Di Mauro M., Ligorini A., Ullio P., Grasso D., Cosmic-ray propagation with DRAGON2: I. numerical solver and astrophysical ingredients, Journal of Cosmology and Astroparticle Physics, 2017, vol. 2017, p. 015

Fabjan D., Borgani S., Tornatore L., Saro A., Murante G., Dolag K., Simulating the effect of active galactic nuclei feedback on the metal enrichment of galaxy clusters, Monthly Notices of the Royal Astronomical Society, 2010, vol. 401, p. 1670

Fang K., Kotera K., Olinto A. V., Newly born pulsars as sources of ultrahigh energy cosmic rays, The Astrophysical Journal, 2012, vol. 750, p. 118

Fang K., Murase K., Linking high-energy cosmic particles by black-hole jets embedded in large-scale structures, Nature Physics, 2018, vol. 14, p. 396

Fang K., Olinto A. V., High-energy neutrinos from sources in clusters of galaxies, The Astrophysical Journal, 2016, vol. 828, p. 37

Farrar G. R., Gruzinov A., Giant AGN flares and cosmic ray bursts, The Astrophysical Journal, 2009, vol. 693, p. 329

Feng J., Tomassetti N., Oliva A., Bayesian analysis of spatial-dependent cosmic-ray propagation: astrophysical background of antiprotons and positrons, Physical Review D, 2016, vol. 94, p. 123007

Feretti L., Dallacasa D., Giovannini G., Tagliani A., The magnetic field in the Coma cluster, arXiv preprint astro-ph/9504058, 1995

Feretti L., Dallacasa D., Govoni F., Giovannini G., Taylor G., Klein U., The radio galaxies and the magnetic field in Abell 119, arXiv preprint astro-ph/9902019, 1999

Fermi-LAT C., et al., Limits on dark matter annihilation signals from the Fermi LAT 4-year measurement of the isotropic gamma-ray background, Journal of Cosmology and Astroparticle Physics, 2015, vol. 2015, p. 008

Ferrari C., Govoni F., Schindler S., Bykov A., Rephaeli Y., , 2008 in , Clusters of Galaxies. Springer pp 93–118

Finke J. D., Razzaque S., Dermer C. D., Modeling the extragalactic background light from stars and dust, The Astrophysical Journal, 2010, vol. 712, p. 238

Fornasa M., Sanchez-Conde M. A., The nature of the diffuse gamma-ray background, Physics Reports, 2015, vol. 598, p. 1

Fornasa M., Zavala J., Sánchez-Conde M. A., Siegal-Gaskins J. M., Delahaye T., Prada F., Vogelsberger M., Zandanel F., Frenk C. S., Characterization of dark-matter-induced anisotropies in the diffuse gamma-ray background, Monthly Notices of the Royal Astronomical Society, 2013, vol. 429, p. 1529

Galanti G., Roncadelli M., De Angelis A., Bignami G. F., Hint at an axion-like particle from the redshift dependence of blazar spectra, Monthly Notices of the Royal Astronomical Society, 2020, vol. 493, p. 1553

Galanti G., Roncadelli M., Tavecchio F., ALP induced polarization effects on photons from galaxy clusters, arXiv preprint arXiv:2202.12286, 2022

Gelmini G. B., Kalashev O., Semikoz D. V., Gamma-ray constraints on maximum cosmogenic neutrino fluxes and UHECR source evolution models, Journal of Cosmology and Astroparticle Physics, 2012, vol. 2012, p. 044

Giacinti G., Kachelrieß M., Semikoz D., Escape model for Galactic cosmic rays and an early extragalactic transition, Physical Review D, 2015, vol. 91, p. 083009

Giacomazzo B., et al., General Relativistic Magnetohydrodynamics: fundamental aspects and applications, 2006

Gilmore R., Somerville R., Primack J., Domínguez A., Semi-analytic modeling of the EBL and consequences for extragalactic gamma-ray spectra https://doi. org/10.1111/j. 1365-2966.2012. 20841. x Mon, Not. Roy. Astron. Soc, 2012, vol. 422, p. 1104

Gilmore R. C., Madau P., Primack J. R., Somerville R. S., Haardt F., GeV gamma-ray attenuation and the high-redshift UV background, Monthly Notices of the Royal Astronomical Society, 2009, vol. 399, p. 1694

Gingold R. A., Monaghan J. J., Smoothed particle hydrodynamics: theory and application to non-spherical stars, Monthly notices of the royal astronomical society, 1977, vol. 181, p. 375

Giovannini G., Tordi M., Feretti L., Radio halo and relic candidates from the NRAO VLA Sky Survey, New Astronomy, 1999, vol. 4, p. 141

Gliozzi M., Bodo G., Ghisellini G., Trussoni E., On the cyclo-synchrotron cross-section, Monthly Notices of the Royal Astronomical Society, 1996, vol. 280, p. 1094

Globus N., Allard D., Parizot E., A complete model of the cosmic ray spectrum and composition across the Galactic to extragalactic transition, Physical Review D, 2015, vol. 92, p. 021302

Gonzalez A. H., Sivanandam S., Zabludoff A. I., Zaritsky D., Galaxy cluster baryon fractions revisited, The Astrophysical Journal, 2013, vol. 778, p. 14

Gouin C., Aghanim N., Bonjean V., Douspis M., Probing the azimuthal environment of galaxies around clusters-From cluster core to cosmic filaments, Astronomy & Astrophysics, 2020, vol. 635, p. A195

Govoni F., Orrù E., Bonafede A., Iacobelli M., Paladino R., Vazza F., Murgia M., Vacca V., Giovannini G., Feretti L., et al., A radio ridge connecting two galaxy clusters in a filament of the cosmic web, Science, 2019, vol. 364, p. 981

Greisen K., End to the cosmic-ray spectrum?, Physical Review Letters, 1966, vol. 16, p. 748

Gu Y.-J., Jirka M., Klimo O., Weber S., Gamma photons and electron-positron pairs from ultra-intense laser-matter interaction: A comparative study of proposed configurations, Matter and Radiation at Extremes, 2019, vol. 4, p. 064403

Hackstein S., Vazza F., Brüggen M., Sorce J. G., Gottlöber S., Simulations of ultra-high energy cosmic rays in the local Universe and the origin of cosmic magnetic fields, Monthly Notices of the Royal Astronomical Society, 2018, vol. 475, p. 2519

Harari D., Mollerach S., Roulet E., On the ultrahigh energy cosmic ray horizon, Journal of Cosmology and Astroparticle Physics, 2006, vol. 2006, p. 012

Harding J. P., Constraints on the diffuse gamma-ray background with hawc, arXiv preprint arXiv:1908.11485, 2019

Harris J., Chadwick P. M., Photon-axion mixing within the jets of active galactic nuclei and prospects for detection, Journal of Cosmology and Astroparticle Physics, 2014, vol. 2014, p. 018

Hasinger G., Miyaji T., Schmidt M., Luminosity-dependent evolution of soft X-ray selected AGN-New Chandra and XMM-Newton surveys, Astronomy & Astrophysics, 2005, vol. 441, p. 417

Hawley J. F., Gammie C. F., Balbus S. A., Local three-dimensional magnetohydrodynamic simulations of accretion disks, The Astrophysical Journal, 1995, vol. 440, p. 742

He H.-N., Wang T., Fan Y.-Z., Liu S.-M., Wei D.-M., Diffuse PeV neutrino emission from ultraluminous infrared galaxies, Physical Review D, 2013, vol. 87, p. 063011

Heinbach U., Simon M., Propagation of galactic cosmic rays under diffusive reacceleration, The Astrophysical Journal, 1995, vol. 441, p. 209

Heinze J., Boncioli D., Bustamante M., Winter W., Cosmogenic neutrinos challenge the cosmic-ray proton dip model, The Astrophysical Journal, 2016, vol. 825, p. 122

Heiter C., Kuempel D., Walz D., Erdmann M., Production and propagation of ultra-high energy photons using CRPropa 3, Astroparticle Physics, 2018, vol. 102, p. 39

Hillas A. M., The origin of ultra-high-energy cosmic rays, Annual review of astronomy and astrophysics, 1984, vol. 22, p. 425

Hoffman Y., Ribak E., Constrained realizations of Gaussian fields-A simple algorithm, The Astrophysical Journal, 1991, vol. 380, p. L5

Holler M., Berge D., Van Eldik C., Lenain J.-P., Marandon V., Murach T., de Naurois M., Parsons R., Prokoph H., Zaborov D., Observations of the crab nebula with HESS Phase II, arXiv preprint arXiv:1509.02902, 2015

Hopkins A. M., Beacom J. F., On the normalization of the cosmic star formation history, The Astrophysical Journal, 2006, vol. 651, p. 142

Hopkins P. F., Butsky I. S., Panopoulou G. V., Ji S., Quataert E., Faucher-Giguere C.-A., Keres D., First Predicted Cosmic Ray Spectra, Primary-to-Secondary Ratios, and Ionization Rates from MHD Galaxy Formation Simulations, arXiv preprint arXiv:2109.09762, 2021

Hopkins P. F., Chan T., Garrison-Kimmel S., Ji S., Su K.-Y., Hummels C. B., Kereš D., Quataert E., Faucher-Giguère C.-A., But what about...: cosmic rays, magnetic fields, conduction, and viscosity in galaxy formation, Monthly Notices of the Royal Astronomical Society, 2020, vol. 492, p. 3465

Hümmer S., Baerwald P., Winter W., Neutrino emission from gamma-ray burst fireballs, revised, Physical Review Letters, 2012, vol. 108, p. 231101

Hussain S., Alves Batista R., de Gouveia Dal Pino E. M., Propagation of Cosmic Rays and their Secondaries in the Intracluster Medium. In 36th International Cosmic Ray Conference (ICRC2019) , vol. 36, 2019, p. 81

Hussain S., Alves Batista R., de Gouveia Dal Pino E. M., Dolag K., High-energy neutrino production in clusters of galaxies, Monthly Notices of the Royal Astronomical Society, 2021, vol. 507, p. 1762

Hussain S., Alves Batista R., de Gouveia Dal Pino E. M., Dolag K., The Diffuse Gamma-Ray Flux from Clusters of Galaxies, arXiv:2203.01260, 2022

IceCube-Collaboration Aartsen M., Ackermann M., Adams J., Aguilar J. A., Ahlers M., Ahrens M., Al Samarai I., Altmann D., Andeen K., et al., Neutrino emission from the direction of the blazar TXS 0506+ 056 prior to the IceCube-170922A alert, Science, 2018, vol. 361, p. 147

Inoue S., Aharonian F. A., Sugiyama N., Hard X-ray and gamma-ray emission induced by ultra-high-energy protons in cluster accretion shocks, The Astrophysical Journal Letters, 2005, vol. 628, p. L9

Inoue S., Sigl G., Miniati F., Armengaud E., Ultrahigh energy cosmic rays as heavy nuclei from cluster accretion shocks, arXiv preprint astro-ph/0701167, 2007

Ioka K., Murase K., Toma K., Nagataki S., Nakamura T., Unstable GRB photospheres and e± annihilation lines, The Astrophysical Journal Letters, 2007, vol. 670, p. L77

Ishibashi W., Courvoisier T.-L., Synchrotron radio emission in radio-quiet AGNs, Astronomy & Astrophysics, 2011, vol. 525, p. A118

Ito T., Makino J., Fukushige T., Ebisuzaki T., Okumura S. K., Sugimoto D., A Special-Purpose Computer forN-Body Simulations: GRAPE-2A, Publications of the Astronomical Society of Japan, 1993, vol. 45, p. 339

Jackson J. D., Classical electrodynamics 3rd ed john wiley & sons, Inc., NewYork, NY, 1999

Jansson R., Farrar G. R., A new model of the galactic magnetic field, The Astrophysical Journal, 2012, vol. 757, p. 14

Jeltema T. E., Profumo S., Implications of Fermi observations for hadronic models of radio halos in clusters of galaxies, The Astrophysical Journal, 2011, vol. 728, p. 53

Jenkins A., Frenk C., White S. D., Colberg J., Cole S., Evrard A. E., Couchman H., Yoshida N., The mass function of dark matter haloes, Monthly Notices of the Royal Astronomical Society, 2001, vol. 321, p. 372

Kachelriess M., Transition from Galactic to Extragalactic Cosmic Rays. In EPJ Web of Conferences , vol. 210, 2019, p. 04003

Kachelrieß M., Ostapchenko S., Tomas R., ELMAG: A Monte Carlo simulation of electromagnetic cascades on the extragalactic background light and in magnetic fields, Computer Physics Communications, 2012, vol. 183, p. 1036

Kadowaki L. H., de Gouveia Dal Pino E. M., Medina-Torrejón T. E., Mizuno Y., Kushwaha P., Fast Magnetic Reconnection Structures in Poynting Flux-dominated Jets, The Astrophysical Journal, 2021, vol. 912, p. 109

Kadowaki L. H., de Gouveia Dal Pino E. M., Singh C. B., The role of fast magnetic reconnection on the radio and gamma-ray emission from the nuclear regions of microquasars and low luminosity AGNs, The Astrophysical Journal, 2015, vol. 802, p. 113

Kafexhiu E., Aharonian F., Taylor A. M., Vila G. S., Parametrization of gamma-ray production cross sections for p p interactions in a broad proton energy range from the kinematic threshold to PeV energies, Physical Review D, 2014, vol. 90, p. 123014

Kampert K.-H., Kulbartz J., Maccione L., Nierstenhoefer N., Schiffer P., Sigl G., van Vliet A. R., CRPropa 2.0–A public framework for propagating high energy nuclei, secondary gamma rays and neutrinos, Astroparticle Physics, 2013, vol. 42, p. 41

Kashiyama K., Mészáros P., Galaxy mergers as a source of cosmic rays, neutrinos, and gamma rays, The Astrophysical Journal Letters, 2014, vol. 790, p. L14

Katou T., Amano T., Theory of stochastic shock drift acceleration for electrons in the shock transition region, The Astrophysical Journal, 2019, vol. 874, p. 119

Kelner S., Aharonian F., Energy spectra of gamma rays, electrons, and neutrinos produced at interactions of relativistic protons with low energy radiation, Physical Review D, 2008, vol. 78, p. 034013

Kelner S., Aharonian F. A., Bugayov V., Energy spectra of gamma rays, electrons, and neutrinos produced at proton-proton interactions in the very high energy regime, Physical Review D, 2006, vol. 74, p. 034018

Khan E., Goriely S., Allard D., Parizot E., Suomijärvi T., Koning A. J., Hilaire S., Duijvestijn M. C., Photodisintegration of ultra-high-energy cosmic rays revisited, Astroparticle Physics, 2005, vol. 23, p. 191

Khiali B., de Gouveia Dal Pino E. M., High-energy neutrino emission from the core of low luminosity AGNs triggered by magnetic reconnection acceleration, Monthly Notices of the Royal Astronomical Society, 2016, vol. 455, p. 838

Kim J., Ryu D., Kang H., Kim S., Rey S.-C., Filaments of galaxies as a clue to the origin of ultrahigh-energy cosmic rays, Science advances, 2019, vol. 5, p. eaau8227

Kleimann J., Schorlepp T., Merten L., Tjus J. B., Solenoidal improvements for the JF12 Galactic magnetic field model, The Astrophysical Journal, 2019, vol. 877, p. 76

KM3Net S., Adrian-Martinez et al, J. Phys. G, 2016, vol. 43, p. 1601

Kneiske T. M., Bretz T., Mannheim K., Hartmann D., Implications of cosmological gamma-ray absorption-II. Modification of gamma-ray spectra, Astronomy & Astrophysics, 2004, vol. 413, p. 807

Knežević S., An Integral View of Shocks, 2014, Ph.D. Thesis

Kobzar O., Hnatyk B., Marchenko V., Sushchov O., Search for ultra high-energy cosmic rays from radiogalaxy Virgo A, Monthly Notices of the Royal Astronomical Society, 2019, vol. 484, p. 1790

Kolmogorov A. N., Dissipation of energy in the locally isotropic turbulence, Proceedings of the Royal Society of London. Series A: Mathematical and Physical Sciences, 1991, vol. 434, p. 15

Komatsu E., Dunkley J., Nolta M., Bennett C., Gold B., Hinshaw G., Jarosik N., Larson D., Limon M., Page L., et al., Five-year wilkinson microwave anisotropy probe* observations: cosmological interpretation, The Astrophysical Journal Supplement Series, 2009, vol. 180, p. 330

Koning A., Delaroche J., Local and global nucleon optical models from 1 keV to 200 MeV, Nuclear Physics A, 2003, vol. 713, p. 231

Koning A., Hilaire S., Goriely S., TALYS-1.6, User manual, Nuclear Research and Consultancy Group NRG, Petten, 2013

Koning A. J., Hilaire S., Duijvestijn M. C., TALYS: Comprehensive nuclear reaction modeling. In AIP Conference Proceedings , vol. 769, 2005, p. 1154

Kopp A., Büsching I., Strauss R., Potgieter M., A stochastic differential equation code for multidimensional Fokker–Planck type problems, Computer Physics Communications, 2012, vol. 183, p. 530

Kornecki P., Peretti E., del Palacio S., Benaglia P., Pellizza L., Exploring the physics behind the non-thermal emission from star-forming galaxies detected in γ rays, Astronomy & Astrophysics, 2022, vol. 657, p. A49

Kotera K., Allard D., Murase K., Aoi J., Dubois Y., Pierog T., Nagataki S., Propagation of ultrahigh energy nuclei in clusters of galaxies: resulting composition and secondary emissions, The Astrophysical Journal, 2009, vol. 707, p. 370

Kowal G., de Gouveia Dal Pino E. M., Lazarian A., Particle acceleration in turbulence and weakly stochastic reconnection, Physical Review Letters, 2012, vol. 108, p. 241102

Lazarian A., Vlahos L., Kowal G., Yan H., Beresnyak A., de Gouveia Dal Pino E., Turbulence, magnetic reconnection in turbulent fluids and energetic particle acceleration, Space science reviews, 2012, vol. 173, p. 557

Lazarian A., Xu S., Diffusion of cosmic rays in MHD turbulence with magnetic mirrors, arXiv preprint arXiv:2106.08362, 2021

Le Roux J., Zank G., Ptuskin V., An evaluation of perpendicular diffusion models regarding cosmic ray modulation on the basis of a hydromagnetic description for solar wind turbulence, Journal of Geophysical Research: Space Physics, 1999, vol. 104, p. 24845

Lee S., Propagation of extragalactic high energy cosmic and γ rays, Physical Review D, 1998, vol. 58, p. 043004

Linsley J., Scarsi L., Arrival times of air shower particles at large distances from the axis, Physical Review, 1962, vol. 128, p. 2384

Liu R.-Y., Wang X.-Y., Diffuse PeV neutrinos from gamma-ray bursts, The Astrophysical Journal, 2013, vol. 766, p. 73

Liu R.-Y., Wang X.-Y., Inoue S., Crocker R., Aharonian F., Diffuse PeV neutrinos from EeV cosmic ray sources: Semirelativistic hypernova remnants in star-forming galaxies, Physical Review D, 2014, vol. 89, p. 083004

Lovisari L., Reiprich T., Schellenberger G., Scaling properties of a complete X-ray selected galaxy group sample, Astronomy & Astrophysics, 2015, vol. 573, p. A118

Mao X., Convergence rates of the truncated Euler–Maruyama method for stochastic differential equations, Journal of Computational and Applied Mathematics, 2016, vol. 296, p. 362

Marris A., Passman S., Vector fields and flows on developable surfaces, Archive for Rational Mechanics and Analysis, 1969, vol. 32, p. 29

Marsh M. D., Russell H. R., Fabian A. C., McNamara B. R., Nulsen P., Reynolds C. S., A new bound on axion-like particles, Journal of Cosmology and Astroparticle Physics, 2017, vol. 2017, p. 036

Mastichiadis A., Consequences of proton acceleration in blazar jets, Galaxies, 2016, vol. 4, p. 59

Mathis H., Lemson G., Springel V., Kauffmann G., White S., Eldar A., Dekel A., Simulating the formation of the local galaxy population, Monthly notices of the royal astronomical society, 2002, vol. 333, p. 739

Maximon L. C., Electromagnetic Interactions from 5 to 500 MeV and Nuclear Research: A Position Paper as of March 1977. vol. 13, Department of Commerce, National Bureau of Standards, 1977

Mbarek R., Caprioli D., Bottom-up Acceleration of Ultra-high-energy Cosmic Rays in the Jets of Active Galactic Nuclei, The Astrophysical Journal, 2019, vol. 886, p. 8

Medina Tanco G., de Gouveia Dal Pino E. M., Horvath J. E., Non-diffusive propagation of ultra high energy cosmic rays, Astroparticle Physics, 1997, vol. 6, p. 337

Medina-Tanco G., Enßlin T. A., Isotropization of ultra-high energy cosmic ray arrival directions by radio ghosts, Astroparticle Physics, 2001, vol. 16, p. 47

Medina-Torrejon T. E., de Gouveia Dal Pino E. M., Kadowaki L. H., Kowal G., Singh C. B., Mizuno Y., Particle Acceleration by Relativistic Magnetic Reconnection Driven by Kink Instability Turbulence in Poynting Flux–Dominated Jets, The Astrophysical Journal, 2021, vol. 908, p. 193

Merten L., Tjus J. B., Fichtner H., Eichmann B., Sigl G., CRPropa 3.1-a low energy extension based on stochastic differential equations, Journal of Cosmology and Astroparticle Physics, 2017, vol. 2017, p. 046

Mollerach S., Roulet E., Extragalactic cosmic rays diffusing from two populations of sources, Physical Review D, 2020, vol. 101, p. 103024

Monaghan J. J., Why particle methods work, SIAM Journal on Scientific and Statistical Computing, 1982, vol. 3, p. 422

Monaghan J. J., Smoothed particle hydrodynamics, Annual review of astronomy and astrophysics, 1992, vol. 30, p. 543

Montes M., Trujillo I., Intracluster light: a luminous tracer for dark matter in clusters of galaxies, Monthly Notices of the Royal Astronomical Society, 2019, vol. 482, p. 2838

Moriya T. J., Tanaka M., Yasuda N., Jiang J.-a., Lee C.-H., Maeda K., Morokuma T., Nomoto K., Quimby R. M., Suzuki N., et al., First release of high-redshift superluminous supernovae from the subaru HIgh-Z SUpernova CAmpaign (SHIZUCA). I. Photometric properties, The Astrophysical Journal Supplement Series, 2019, vol. 241, p. 16

Motz J., Olsen H. A., Koch H., Pair production by photons, Reviews of Modern Physics, 1969, vol. 41, p. 581

Mücke A., Engel R., Rachen J., Protheroe R., Stanev T., Monte Carlo simulations of photohadronic processes in astrophysics, Computer Physics Communications, 2000, vol. 124, p. 290

Mucke A., Rachen J., Stanev T., Protheroe R., Engel R., Photohadronic processes in astrophysical environments, Publications of the Astronomical Society of Australia, 1999, vol. 16, p. 160

Murase K., Ahlers M., Lacki B. C., Testing the hadronuclear origin of PeV neutrinos observed with IceCube, Physical Review D, 2013, vol. 88, p. 121301

Murase K., Beacom J. F., Galaxy clusters as reservoirs of heavy dark matter and high-energy cosmic rays: constraints from neutrino observations, Journal of Cosmology and Astroparticle Physics, 2013, vol. 2013, p. 028

Murase K., Inoue S., Nagataki S., Cosmic rays above the second knee from clusters of galaxies and associated high-energy neutrino emission, The Astrophysical Journal Letters, 2008, vol. 689, p. L105

Murase K., Kashiyama K., Kiuchi K., Bartos I., Gamma-ray and hard X-ray emission from pulsar-aided supernovae as a probe of particle acceleration in embryonic pulsar wind nebulae, The Astrophysical Journal, 2015, vol. 805, p. 82

Murase K., Waxman E., Constraining high-energy cosmic neutrino sources: implications and prospects, Physical Review D, 2016, vol. 94, p. 103006

Nagai H., Kawakatu N., Diffuse Synchrotron Emission Associated with the Starburst in the Circumnuclear Disk of NGC 1275, The Astrophysical Journal Letters, 2021, vol. 914, p. L11

Neronov A., Semikoz D., Galactic diffuse gamma-ray emission at TeV energy, Astronomy & Astrophysics, 2020, vol. 633, p. A94

Nishiwaki K., Asano K., Murase K., Particle Reacceleration by Turbulence and Radio Constraints on Multi-Messenger High-Energy Emission from the Coma Cluster, arXiv preprint arXiv:2105.04541, 2021

Norman C. A., Melrose D. B., Achterberg A., The origin of cosmic rays above 10 18.5 eV, The Astrophysical Journal, 1995, vol. 454, p. 60

Paliya V. S., Böttcher M., Diltz C., Stalin C., Sahayanathan S., Ravikumar C., The violent hard X-ray variability of MRK 421 observed by NuSTAR in 2013 April, The Astrophysical Journal, 2015, vol. 811, p. 143

Parizot E., Cosmic ray origin: lessons from ultra-high-energy cosmic rays and the Galactic/extragalactic transition, arXiv preprint arXiv:1410.2655, 2014

Pe'er A., Waxman E., Prompt gamma-ray burst spectra: detailed calculations and the effect of pair production, The Astrophysical Journal, 2004, vol. 613, p. 448

Penzias A. A., Wilson R. W., A measurement of excess antenna temperature at 4080 Mc/s., The Astrophysical Journal, 1965, vol. 142, p. 419

Peretti E., Blasi P., Aharonian F., Morlino G., Cristofari P., Contribution of starburst nuclei to the diffuse gamma-ray and neutrino flux, Monthly Notices of the Royal Astronomical Society, 2020, vol. 493, p. 5880

Peretti E., Morlino G., Blasi P., Aharonian F., Cosmic ray transport in Starburst galaxies and possible observables, PoS ICRC 2019, 2019, p. 382

Peretti E., Morlino G., Blasi P., Cristofari P., Particle acceleration and multi-messenger emission from starburst-driven galactic winds, arXiv preprint arXiv:2104.10978, 2021

Pfrommer C., Simulating cosmic rays in clusters of galaxies–III. Non-thermal scaling relations and comparison to observations, Monthly Notices of the Royal Astronomical Society, 2008, vol. 385, p. 1242

Pinzke A., Pfrommer C., Simulating the γ-ray emission from galaxy clusters: a universal cosmic ray spectrum and spatial distribution, Monthly Notices of the Royal Astronomical Society, 2010, vol. 409, p. 449

Planelles S., Borgani S., Fabjan D., Killedar M., Murante G., Granato G., Ragone-Figueroa C., Dolag K., On the role of AGN feedback on the thermal and chemodynamical properties of the hot intracluster medium, Monthly Notices of the Royal Astronomical Society, 2014, vol. 438, p. 195

Priest E. R., Solar magnetohydrodynamics. vol. 21, Springer Science & Business Media, 2012

Prokhorov D., Churazov E., Counting gamma rays in the directions of galaxy clusters, Astronomy & Astrophysics, 2014, vol. 567, p. A93

Protheroe R., Biermann P., A new estimate of the extragalactic radio background and implications for ultra-high-energy γ-ray propagation, Astroparticle Physics, 1996, vol. 6, p. 45

Protheroe R. J., Effect of energy losses and interactions during diffusive shock acceleration: Applications to SNR, AGN and UHE cosmic rays, Astroparticle Physics, 2004, vol. 21, p. 415

Pshirkov M., Tinyakov P., Kronberg P., Newton-McGee K., Deriving the global structure of the Galactic magnetic field from Faraday rotation measures of extragalactic sources, The Astrophysical Journal, 2011, vol. 738, p. 192

Ptitsyna K. V., Troitsky S. V., Physical conditions in potential accelerators of ultra-high-energy cosmic rays: updated Hillas plot and radiation-loss constraints, Physics-Uspekhi, 2010, vol. 53, p. 691

Raffelt G., Stodolsky L., Mixing of the photon with low-mass particles, Physical Review D, 1988, vol. 37, p. 1237

Reesman R., Walker T., Probing the scale of ALP interactions with Fermi blazars, Journal of Cosmology and Astroparticle Physics, 2014, vol. 2014, p. 021

Reynolds C. S., Marsh M. D., Russell H. R., Fabian A. C., Smith R., Tombesi F., Veilleux S., Astrophysical limits on very light axion-like particles from Chandra grating spectroscopy of NGC 1275, The Astrophysical Journal, 2020, vol. 890, p. 59

Ringwald A., Exploring the role of axions and other WISPs in the dark universe, Physics of the Dark Universe, 2012, vol. 1, p. 116

Risken H., , 1996 in , The Fokker-Planck Equation. Springer pp 63–95

Robertson A., Massey R., Eke V., What does the Bullet Cluster tell us about self-interacting dark matter?, Monthly Notices of the Royal Astronomical Society, 2016, p. stw2670

Rodríguez-Ramírez J. C., de Gouveia Dal Pino E. M., Alves Batista R., Very-high-energy Emission from Magnetic Reconnection in the Radiative-inefficient Accretion Flow of SgrA, The Astrophysical Journal, 2019, vol. 879, p. 6

Rordorf C., Grasso D., Dolag K., Diffusion of ultra-high energy protons in galaxy clusters and secondary X-and gamma-ray emissions, Astroparticle Physics, 2004, vol. 22, p. 167

Rosati P., Borgani S., Norman C., The evolution of X-ray clusters of galaxies, Annual Review of Astronomy and Astrophysics, 2002, vol. 40, p. 539

Roth M. A., Krumholz M. R., Crocker R. M., Celli S., The diffuse γ-ray background is dominated by star-forming galaxies, Nature, 2021, vol. 597, p. 341

Rybicki G., Lightman A., RADIATIVE PROCESSES IN ASTROPHYSICS. Wiley-VCH, 1986

Sanders J., Fabian A., Taylor G., Russell H., Blundell K., Canning R., Hlavacek-Larrondo J., Walker S., Grimes C., A very deep Chandra view of metals, sloshing and feedback in the Centaurus cluster of galaxies, Monthly Notices of the Royal Astronomical Society, 2016, vol. 457, p. 82

Schallmoser S., Krippendorf S., Chadha-Day F., Weller J., Updated Bounds on Axion-Like Particles from X-ray Observations, arXiv preprint arXiv:2108.04827, 2021

Schlickeiser R., A new cosmic ray transport theory in partially turbulent space plasmas: extending the quasilinear approach, The Astrophysical Journal, 2011, vol. 732, p. 96

Schlickeiser R., Cosmic ray astrophysics. Springer Science & Business Media, 2013

Schlickeiser R., Miller J. A., Quasi-linear theory of cosmic ray transport and acceleration: the role of oblique magnetohydrodynamic waves and transit-time damping, The Astrophysical Journal, 1998, vol. 492, p. 352

Schneider P., Extragalactic astronomy and cosmology: an introduction. vol. 146, Springer, 2006

Schneider P., Extragalactic astronomy and cosmology: an introduction. Springer, 2014

Schröder F. G., News from Cosmic Ray Air Showers (ICRC 2019–Cosmic Ray Indirect Rapport), arXiv preprint arXiv:1910.03721, 2019

Senno N., Mészáros P., Murase K., Baerwald P., Rees M. J., Extragalactic star-forming galaxies with hypernovae and supernovae as high-energy neutrino and gamma-ray sources: the case of the 10 TeV neutrino data, The Astrophysical Journal, 2015, vol. 806, p. 24

Shulevski A., Morganti R., Barthel P., Harwood J., Brunetti G., van Weeren R., Röttgering H., White G., Horellou C., Kunert-Bajraszewska M., et al., AGN duty cycle estimates for the ultra-steep spectrum radio relic VLSS J1431. 8+ 1331, Astronomy & Astrophysics, 2015, vol. 583, p. A89

Sigl G., Astroparticle Physics: Theory and Phenomenology, 2017

Sigl G., Miniati F., Enßlin T. A., Cosmic magnetic fields and their influence on ultra-high energy cosmic ray propagation, Nuclear Physics B-Proceedings Supplements, 2004, vol. 136, p. 224

Simionescu A., Nakashima S., Yamaguchi H., Matsushita K., Mernier F., Werner N., Tamura T., Nomoto K., De Plaa J., Leung S., et al., Constraints on the chemical enrichment history of the Perseus Cluster of galaxies from high-resolution X-ray spectroscopy, Monthly Notices of the Royal Astronomical Society, 2019, vol. 483, p. 1701

Sisk-Reynés J., Matthews J. H., Reynolds C. S., Russell H. R., Smith R. N., Marsh M. D., New constraints on light Axion-Like Particles using Chandra Transmission Grating Spectroscopy of the powerful cluster-hosted quasar H1821+ 643, Monthly Notices of the Royal Astronomical Society, 2022, vol. 510, p. 1264

Slane P., Lee S.-H., Ellison D. C., Patnaude D., Hughes J. P., Eriksen K., Castro D., Nagataki S., A CR-hydro-NEI model of the structure and broadband emission from Tycho's supernova remnant, The Astrophysical Journal, 2014, vol. 783, p. 33

Sobacchi E., Lyubarsky Y. E., Magnetic energy dissipation and origin of non-thermal spectra in radiatively efficient relativistic sources, Monthly Notices of the Royal Astronomical Society, 2020, vol. 491, p. 3900

Sokolsky P., Thomson G., Highest energy cosmic-rays and results from the HiRes experiment, Journal of Physics G: Nuclear and Particle Physics, 2007, vol. 34, p. R401

Sokolsky P., Thomson G., Introduction to ultrahigh energy cosmic ray physics. CRC Press, 2020

Sonzogni A., NuDat 2.0: Nuclear structure and decay data on the internet. In AIP Conference Proceedings , vol. 769, 2005, p. 574

Springel V., The cosmological simulation code GADGET-2, Monthly notices of the royal astronomical society, 2005, vol. 364, p. 1105

Springel V., Yoshida N., White S. D., GADGET: a code for collisionless and gasdynamical cosmological simulations, New Astronomy, 2001, vol. 6, p. 79

Sreekumar P., Bertsch D., Dingus B., Esposito J., Fichtel C., Hartman R., Hunter S., Kanbach G., Kniffen D., Lin Y., et al., EGRET observations of the extragalactic gamma-ray emission, The Astrophysical Journal, 1998, vol. 494, p. 523

Stecker F. W., Malkan M. A., Scully S., Intergalactic photon spectra from the far-IR to the UV Lyman limit for 0¡ z¡ 6 and the optical depth of the universe to high-energy gamma rays, The Astrophysical Journal, 2006, vol. 648, p. 774

Stecker F. W., Scully S. T., Malkan M. A., An empirical determination of the intergalactic background light from UV to FIR wavelengths using FIR deep galaxy surveys and the gamma-ray opacity of the universe, The Astrophysical Journal, 2016, vol. 827, p. 6

Stecker F. W., Venters T. M., Components of the extragalactic gamma-ray background, The Astrophysical Journal, 2011, vol. 736, p. 40

Steinmetz M., GRAPESPH: cosmological smoothed particle hydrodynamics simulations with the special-purpose hardware GRAPE, Monthly Notices of the Royal Astronomical Society, 1996, vol. 278, p. 1005

Steinmetz M., Mueller E., On the capabilities and limits of smoothed particle hydrodynamics, Astronomy and Astrophysics, 1993, vol. 268, p. 391

Strauss R. D. T., Effenberger F., A hitch-hiker's guide to stochastic differential equations, Space Science Reviews, 2017, vol. 212, p. 151

Strong A. W., Moskalenko I. V., Propagation of cosmic-ray nucleons in the galaxy, The Astrophysical Journal, 1998, vol. 509, p. 212

Strong A. W., Moskalenko I. V., Reimer O., A new determination of the extragalactic diffuse gamma-ray background from EGRET data, The Astrophysical Journal, 2004, vol. 613, p. 956

Sunyaev R., The thermal history of the universe and the spectrum of relic radiation. In Symposium-International Astronomical Union , vol. 63, 1974, p. 167

Sveshnikova L., Strelnikova O., Ptuskin V., Spectrum and anisotropy of cosmic rays at TeV–PeV-energies and contribution of nearby sources, Astroparticle Physics, 2013, vol. 50, p. 33

Tamborra I., Ando S., Murase K., Star-forming galaxies as the origin of diffuse high-energy backgrounds: Gamma-ray and neutrino connections, and implications for starburst history, Journal of Cosmology and Astroparticle Physics, 2014, vol. 2014, p. 043

The IceCube-Gen2 Collaboration IceCube-Gen2: The Window to the Extreme Universe, arXiv e-prints, 2020, p. arXiv:2008.04323

Thoudam S., Rachen J., van Vliet A., Achterberg A., Buitink S., Falcke H., Hörandel J., Cosmic-ray energy spectrum and composition up to the ankle: the case for a second Galactic component, Astronomy & Astrophysics, 2016, vol. 595, p. A33

Tibolla O., Blandford R. D., Cosmic Ray Origin–Beyond the Standard Models, Nuclear and particle physics proceedings, 2018, vol. 297, p. 1

Tibolla O., Drury L., Prolegomena, Nuclear Physics B-Proceedings Supplements, 2014, vol. 256, p. 1

Tinker J., Kravtsov A. V., Klypin A., Abazajian K., Warren M., Yepes G., Gottlöber S., Holz D. E., Toward a halo mass function for precision cosmology: the limits of universality, The Astrophysical Journal, 2008, vol. 688, p. 709

Tinyakov P., Tkachev I. I., Deflections of cosmic rays in a random component of the Galactic magnetic field, Astroparticle Physics, 2005, vol. 24, p. 32

Tjus J. B., Merten L., Closing in on the origin of Galactic cosmic rays using multimessenger information, Physics Reports, 2020, vol. 872, p. 1

Unger M., Farrar G. R., Anchordoqui L. A., Origin of the ankle in the ultrahigh energy cosmic ray spectrum, and of the extragalactic protons below it, Physical Review D, 2015, vol. 92, p. 123001

Vazza F., Brüggen M., Gheller C., Hackstein S., Wittor D., Hinz P. M., Simulations of extragalactic magnetic fields and of their observables, Classical and Quantum Gravity, 2017, vol. 34, p. 234001

Vazza F., Brüggen M., Wittor D., Gheller C., Eckert D., Stubbe M., Constraining the efficiency of cosmic ray acceleration by cluster shocks, Monthly Notices of the Royal Astronomical Society, 2016, vol. 459, p. 70

Verzi V., Ivanov D., Tsunesada Y., Measurement of energy spectrum of ultra-high energy cosmic rays, Progress of Theoretical and Experimental Physics, 2017, vol. 2017, p. 12A103

Voit G. M., Tracing cosmic evolution with clusters of galaxies, Reviews of Modern Physics, 2005, vol. 77, p. 207

Völk H., Aharonian F., Breitschwerdt D., The nonthermal energy content and gamma ray emission of starburst galaxies and clusters of galaxies, Space Science Reviews, 1996, vol. 75, p. 279

Wang H., Ma X., Zhao Y., An improved Wiener process model with adaptive drift and diffusion for online remaining useful life prediction, Mechanical Systems and Signal Processing, 2019, vol. 127, p. 370

Wang X.-Y., Liu R.-Y., Aharonian F., Constraining the emissivity of ultrahigh energy cosmic rays in the distant universe with the diffuse gamma-ray emission, The Astrophysical Journal, 2011, vol. 736, p. 112

Waxman E., Extra-galactic sources of high-energy neutrinos, New Journal of Physics, 2004, vol. 6, p. 140

Waxman E., , 2017 in , neutrino astronomy: current status, future prospects. World Scientific pp 33–45

Wiener J., Oh S. P., Guo F., Cosmic ray streaming in clusters of galaxies, Monthly Notices of the Royal Astronomical Society, 2013, vol. 434, p. 2209

Winchen T., Buitink S., Energy spectrum of fast second order Fermi accelerators as sources of ultra-high-energy cosmic rays, Astroparticle Physics, 2018, vol. 102, p. 25

Witten E., Some properties of O (32) superstrings, Physics Letters B, 1984, vol. 149, p. 351

Wolfe B., Melia F., The broadband spectrum of galaxy clusters, The Astrophysical Journal, 2008, vol. 675, p. 156

Xu H., Li H., Collins D. C., Li S., Norman M. L., Turbulence and dynamo in galaxy cluster medium: implications on the origin of cluster magnetic fields, The Astrophysical Journal Letters, 2009, vol. 698, p. L14

Xu S., Lazarian A., Trapping of cosmic rays in MHD turbulence, The Astrophysical Journal, 2020, vol. 894, p. 63

Xu S., Yan H., Cosmic-ray parallel and perpendicular transport in turbulent magnetic fields, The Astrophysical Journal, 2013, vol. 779, p. 140

Yang R.-Z., Wang Y., The diffuse gamma-ray emission toward the Galactic mini starburst W43, Astronomy & Astrophysics, 2020, vol. 640, p. A60

Yoast-Hull T. M., Everett J. E., Gallagher III J., Zweibel E. G., Winds, clumps, and interacting cosmic rays in M82, The Astrophysical Journal, 2013, vol. 768, p. 53

Yoon Y., Ahn H., Allison P., Bagliesi M., Beatty J., Bigongiari G., Boyle P., Childers J., Conklin N., Coutu S., et al., Cosmic-ray proton and helium spectra from the first CREAM flight, The Astrophysical Journal, 2011, vol. 728, p. 122

Yoshida S., Hayashida N., Honda K., Honda M., Imaizumi S., Inoue N., Kadota K., Kakimota F., Kamata K., Kawaguchi S., et al., Lateral distribution of charged particles in giant air showers above 1 EeV observed by AGASA, Journal of Physics G: Nuclear and Particle Physics, 1994, vol. 20, p. 651

Yuan C., Murase K., Mészáros P., Secondary Radio and X-Ray Emissions from Galaxy Mergers, The Astrophysical Journal, 2019, vol. 878, p. 76

Yue C., Ma P.-X., Yuan Q., Fan Y.-Z., Chen Z.-F., Cui M.-Y., Dai H.-T., Dong T.-K., Huang X., Jiang W., et al., Implications on the origin of cosmic rays in light of 10 TV spectral softenings, Frontiers of Physics, 2020, vol. 15, p. 1

Yüksel H., Kistler M. D., Beacom J. F., Hopkins A. M., Revealing the high-redshift star formation rate with gamma-ray bursts, The Astrophysical Journal Letters, 2008, vol. 683, p. L5

Zahri M., Stochastic diffusion problems: Comparison between euler-maruyama and runge-kutta schemes, Journal of Numerical Mathematics and Stochastics, 2009, vol. 1, p. 65

Zandanel F., Pfrommer C., Prada F., On the physics of radio haloes in galaxy clusters: scaling relations and luminosity functions, Monthly Notices of the Royal Astronomical Society, 2014, vol. 438, p. 124

Zandanel F., Tamborra I., Gabici S., Ando S., High-energy gamma-ray and neutrino backgrounds from clusters of galaxies and radio constraints, Astronomy & Astrophysics, 2015, vol. 578, p. A32

Zatsepin G. T., Kuz'min V. A., Upper limit of the spectrum of cosmic rays, Soviet Journal of Experimental and Theoretical Physics Letters, 1966, vol. 4, p. 78

Zhang B. T., Murase K., Kimura S. S., Horiuchi S., Mészáros P., Low-luminosity gamma-ray bursts as the sources of ultrahigh-energy cosmic ray nuclei, Physical Review D, 2018, vol. 97, p. 083010

Zhang C., Churazov E., Zhuravleva I., Pairs of giant shock waves (N-waves) in merging galaxy clusters, Monthly Notices of the Royal Astronomical Society, 2021, vol. 501, p. 1038

Zhang M., A Markov stochastic process theory of cosmic-ray modulation, The Astrophysical Journal, 1999, vol. 513, p. 409

Appendix

Appendix A

GADGET Code

A.1 Basic MHD Equations

In the collisionless dynamics and gravity, dark matter and stars are modeled as self gravitating fluid. They can be described by the collisionless Boltzmann equation,

$$\frac{df}{dt} = \frac{\partial f}{\partial t} + v\frac{\partial f}{\partial x} - \frac{\partial \Phi}{\partial r}\frac{\partial f}{\partial v}, \tag{A.1}$$

$$\nabla^2\Phi(r,t) = 4\pi G \int f(r,v,t)dv, \tag{A.2}$$

where $f(r,v,t)$ is the mass density in particle phase space and Φ is the self-consistent potential and the solution of the above Poisson's equation A.2. Dolag et al. (1999) solved this coupled system using a N-body approach (Dolag et al., 2002, 2005).

The IGM, ICM, and/or ISM can be described by modeling it as an ideal gas (e.g., Dolag et al., 1999, 2002; Springel et al., 2001). Then the equation of continuity for the ideal, inviscid gas is,

$$\frac{d\rho}{dt} + \rho\nabla.v = 0. \tag{A.3}$$

The general equation of motion, under the condition of electrical neutrality of the plasma can be written

$$\rho\frac{dv}{dt} = -\nabla P + \vec{j} \times \vec{B} + F, \tag{A.4}$$

where

$$\vec{j} \times \vec{B} = (\nabla \times \vec{B}) \times \vec{B}/\mu = (\vec{B}.\nabla)\vec{B}/\mu - \nabla(B^2/(2\mu)), \tag{A.5}$$

the first term on the right-hand side of equation A.5 is the magnetic tension and the second term $(B^2/2\mu)$ represents the magnetic field per unit area (μ is the magnetic permeability), and F represents the effect due to gravity and viscosity in equation A.4. Further, the evolution of thermal energy (u) per unit mass, according to the first law of thermodynamics

$$\frac{\partial u}{\partial t} = -\nabla.\left(u + P + \frac{B^2}{8\pi}\right)v - \frac{\Lambda(u,\rho,B)}{\rho} \tag{A.6}$$

Where $\Lambda(u,\rho,B)$ is a net cooling function that describes the sources of heating and radiative losses for the gas. In equations A.3, A.4, and A.6 the ρ and P are the density and thermal pressure of the gas, respectively. We used the Lagrangian time derivatives which is defined as $\frac{d}{dt} = \frac{\partial}{\partial t} + v.\nabla$, in equations A.3 and A.4. The equation of state for the ideal gas is $P = (1-\gamma)\rho u$, where the γ is the adiabatic exponent, For the mono-atomic ideal gas its value is $\gamma = 5/3$.

The induction equation for the ideally conducting plasma (with neglible resistivity) is e.g.,

$$\frac{d\vec{B}}{dt} = (\vec{B}.\nabla)\vec{v} - \vec{B}(\nabla.\vec{v}) + \vec{v}(\nabla.\vec{B}) \tag{A.7}$$

Theoretically, we can neglect the last term of equation A.7. But numerically, it will not vanish, exactly. One has to take care of this fact as it is done in all numerical simulations (e.g., Dolag et al., 1999, 2005).

The back-reaction of the magnetic field on the plasma can be calculated by the Lorentz force,

$$\vec{L} = -\nabla\left(\frac{\vec{B}^2}{8\pi}\right) + \frac{1}{4\pi}(\vec{B}.\nabla)\vec{B}. \tag{A.8}$$

The Lorentz force in the tensor form is,

$$L_j = \frac{\partial M_{ij}}{\partial x_i}, \quad \text{where} \quad M_{ij} = \frac{1}{4\pi}\left(\vec{B}_i\vec{B}_j - \frac{1}{2}\vec{B}^2\delta_{ij}\right) \tag{A.9}$$

The GADGET code developed by Springel et al. (2001) is a Lagrangean code that employs the Smoothed Particle Hydrodynamics (SPH) technique (e.g., Gingold and Monaghan, 1977; Monaghan, 1982, 1992; Steinmetz and Mueller, 1993). SPH is a particle interpolation method where any physical quantity is expressed in terms of its values at a set of disordered points (the SPH particles). SPH employs the Lagrangian equations of the fluid described above and does not need a grid to calculate spatial derivatives, thus avoiding problems associated with mesh tangling and distortion. The derivatives are calculated by analytical differentiation of interpolation formulae (as described below, in Section A.2). GADGET can be used for isolated self-gravitating systems including gas and also for cosmological SPH/N-body simulations. This code uses either a tree algorithm or the special

purpose hardware GRAPE (Gravity Pipe) in order to compute the interactions between neighbor SPH particles (Ito et al., 1993; Steinmetz, 1996). Dolag et al. (1999, 2005) used GRAPE to calculate the gravitational forces of the two components: dark matter (which interacts only through gravity) and baryonic gas.

A.2 SPH Description of the Fluid Equations

Smooth-particle hydrodynamics (SPH, Monaghan (1992)) replaces parcels of the flow with smoothed particles of variable radius. The average mass density of an ensemble of these types of particles with mass m_a at position $\vec{r}_a$ is defined as $\langle\rho(\vec{r})\rangle = \sum_a m_a W(\vec{r} - \vec{r}_a h)$. The radius of extended particles is specified by the SPH kernel $W(\delta\vec{r}, h)$ (also denominated smoothing or weigh function), that depends on the distance $\delta\vec{r}$ from the point of consideration and the finite width h (also denominated the SPH particle smoothing length). Dolag et al. (2005) followed the kernel from Monaghan (1992).

Following the SPH description as described in (e.g., Monaghan, 1992; Dolag et al., 1999) the momentum equation for a particle at a position $\vec{r}_a$ takes the form (without the magnetic force component)

$$\left(\frac{d\vec{v}_a}{dt}\right)_{hyd} = \sum_b m_b \left(\frac{P_b}{\rho_b^2} + \frac{P_a}{\rho_a^2} + \Pi_{ab}\right) \times \nabla_a W(\vec{r}_a - \vec{r}_b, h) \tag{A.10}$$

Similarly, the internal energy (u_a) equation can be written as

$$\left(\frac{d\vec{u}_a}{dt}\right) = \sum_b m_b \left(\frac{P_b}{\rho_b^2} + \frac{1}{2}\Pi_{ab}\right)(\vec{v}_a - \vec{v}_b) \times \nabla_a W(\vec{r}_a - \vec{r}_b, h) \tag{A.11}$$

These equations are supplemented by the equation of state of ideal gas, $P = (\gamma - 1)\rho u \implies P_i = (\gamma - 1)\rho_i u_i$, with $\gamma = 5/3$. Where P_a, P_b, and ρ_a, ρ_b are the pressure and density at positions $\vec{r}_a$ and $\vec{r}_b$, respectively. To capture shocks, Monaghan (1992); Dolag et al. (1999); Springel et al. (2001) incorporate the viscosity tensor Π_{ab}.

In the SPH language the induction equation A.7 becomes,

$$\frac{d\vec{B}_{a,j}}{dt} = \frac{1}{\rho_a} \sum_b m_b (\vec{B}_{a,j}\vec{v}_{ab} - \vec{B}_a \vec{v}_{ab,j}) \times \nabla_a W(\vec{r}_a - \vec{r}_b, h) \tag{A.12}$$

and the equation A.9 takes the form

$$\left(\frac{d\vec{v}_a}{dt}\right)_{mag} = \sum_b m_b \left[\left(\frac{M}{\rho^2}\right)_a + \left(\frac{M}{\rho^2}\right)_b\right] \times \nabla_a W(\vec{r}_a - \vec{r}_b, h) \tag{A.13}$$

To describe the complete equation of motion in MHD we added equations A.10 and A.13

$$\left(\frac{d\vec{v}_a}{dt}\right) = \sum_b m_b \left(\left[\frac{P_b}{\rho_b^2} + \frac{P_a}{\rho_a^2} + \Pi_{ab} \right] + \left[\left(\frac{M}{\rho^2}\right)_a + \left(\frac{M}{\rho^2}\right)_b \right] \right) \times \nabla_a W(\vec{r}_a - \vec{r}_b, h). \quad \text{(A.14)}$$

For more detailed implemention of the GADGET code and SPH technique one can see Monaghan (1992); Steinmetz and Mueller (1993); Dolag et al. (1999, 2005); Springel et al. (2001); Springel (2005) (and reference therein).

Appendix B

Simulation of CR propagation into a turbulent magnetic field environment with uniform background radiation

Employing the CRPropa 3 code (Alves Batista et al., 2016), we simulated the propagation of CRs in a three-dimensional turbulent environment. We assume the turbulent magnetic field with a Kolmogorov spectrum (e.g., Kolmogorov, 1991; Boldyrev and Cattaneo, 2004; Bovino et al., 2013). We consider uniform distribution of sources at different distances, emitting UHECRs in the energy range $(10^{18} - 10^{21})$ eV with spectral index E^{-1}. We obtained the resulting CR, and neutrino spectra, as well as the deflection angle distribution of the CRs.

Fig. B.1 shows the CR spectrum that arrives at the observer after propagation in a background turbulent magnetic field with maximum intensities 10^{-10} G and of 10^{-9} G ($10^{-9} \equiv$ nG). Figs. B.1 and B.2 present the average deflection angle of CRs per energy bins. It can be seen that the deflection angle for the CR of energy $\lesssim 10^{19}$ eV is much larger than that of the CRs with energy $\gtrsim 10^{19}$ eV. Fig. B.1 also indicates the larger deflection angle due to stronger magnetic field, as expected. Our results are in good agreement with previous predictions (e. g., Medina Tanco et al., 1997; Sigl et al., 2004; Dolag et al., 2004; Tinyakov and Tkachev, 2005; Alves Batista et al., 2017; Arámburo-García et al., 2021).

We observe the suppression of CRs flux in Figs. B.3 and B.4 (appears as bumps at energy 5×10^{19} eV), due to photopion production which is compatible with the GZK cutoff (Greisen, 1966; Zatsepin and Kuz'min, 1966). This suppression is occur obviously due to CRs interactions with the CMB which are more noticeable at high energies ($E > 10^{19}$ eV).

Upper panel of Fig. B.4 shows the suppression of the flux of CRs due to the magnetic

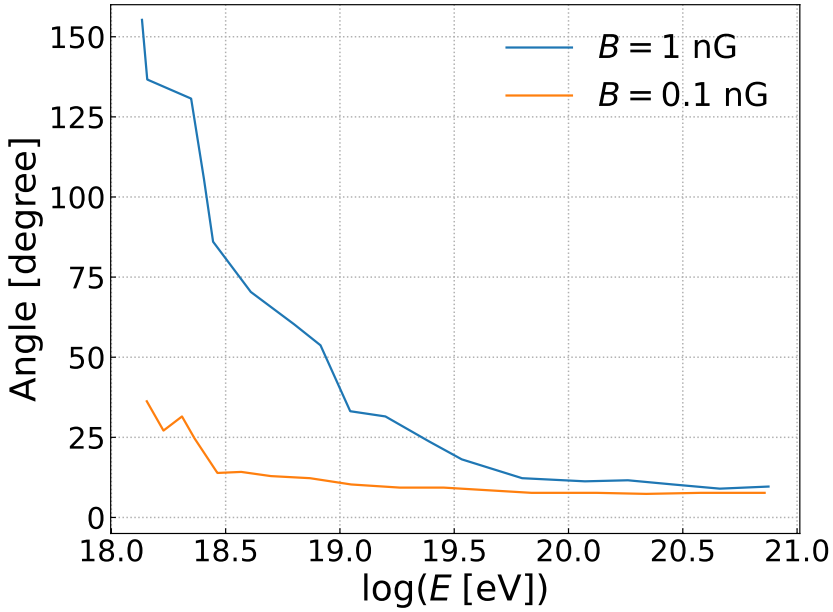

Figure B.1: CR Energy vs deflection angle. This figure shows the deflection angle (due to the magnetic field) of CRs in the energy range $(10^{18} - 10^{21})$ eV, as a function of the energy and for two maximum magnetic field intensities: $B = 10^{-9}$ G and 10^{-10} G. Our results are in good agreement with Dolag et al. (2004); Sigl et al. (2004); Alves Batista et al. (2017).

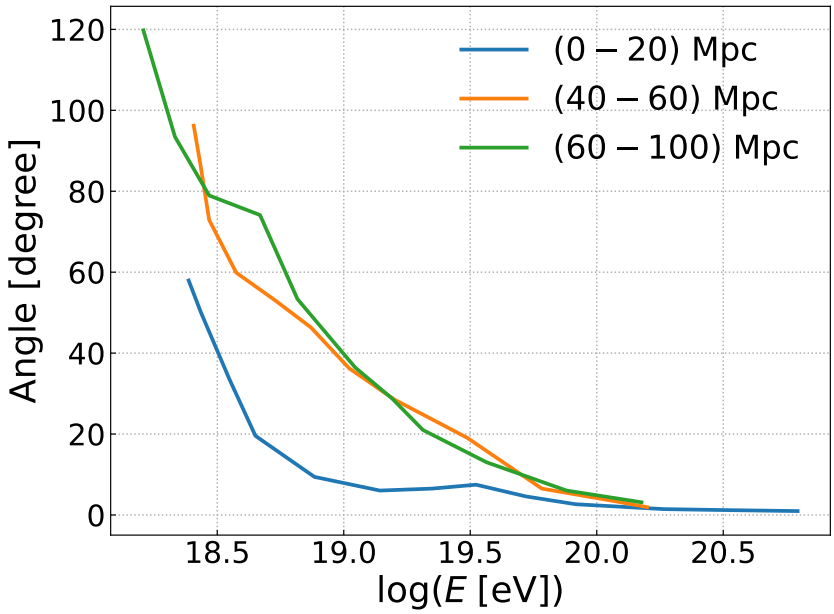

Figure B.2: Energy vs deflection angle. This plot shows the deflection per distance bins (maximum distance is 100 Mpc) considering an energy range at the source $(10^{18} - 10^{21})$ eV.

field for energies $\lesssim 5 \times 10^{18}$ eV. One can see that the suppression is prominent for high magnetic field $B = 1$ nG). In the lower panel of Fig. B.4 we show the flux of neutrinos from

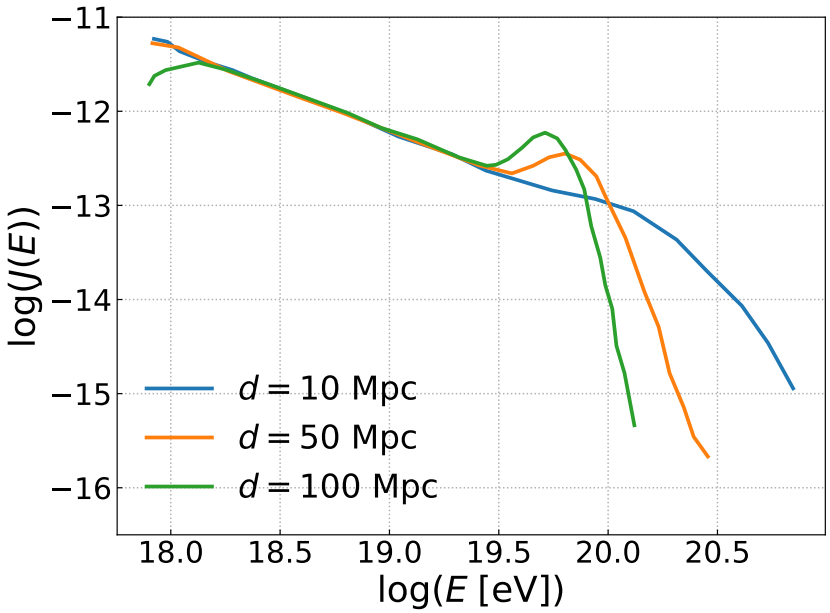

Figure B.3: Here we plotted the flux of ultra high energy CRs for different distance (d) observers. For 100 Mpc and 50 Mpc distances, one can see the suppression of CRs flux due to photopion production, the GZK limit (Greisen, 1966; Zatsepin and Kuz'min, 1966). We note that the appearance of the bumps in the green and red curves is due to the interactions of CRs with CMB that are more pronounced at energy $\gtrsim 5 \times 10^{19}$ eV.

CR sources at different distances. These neutrinos are the product of hadronic interactions of HECRs with the photon fields (CMB and EBL). The EBL interactions are more effective at large distances (see Fig. 3.6). Also, the CRs have more time to interact, therefore, the flux of neutrinos for 100 Mpc distance is higher than that of 10 Mpc. Note that the results presented in Figs. B.3 and B.4 are in arbitrary code units. We did not normalize the flux of CRs and neutrinos with respect to any specific type of astrophysical source.

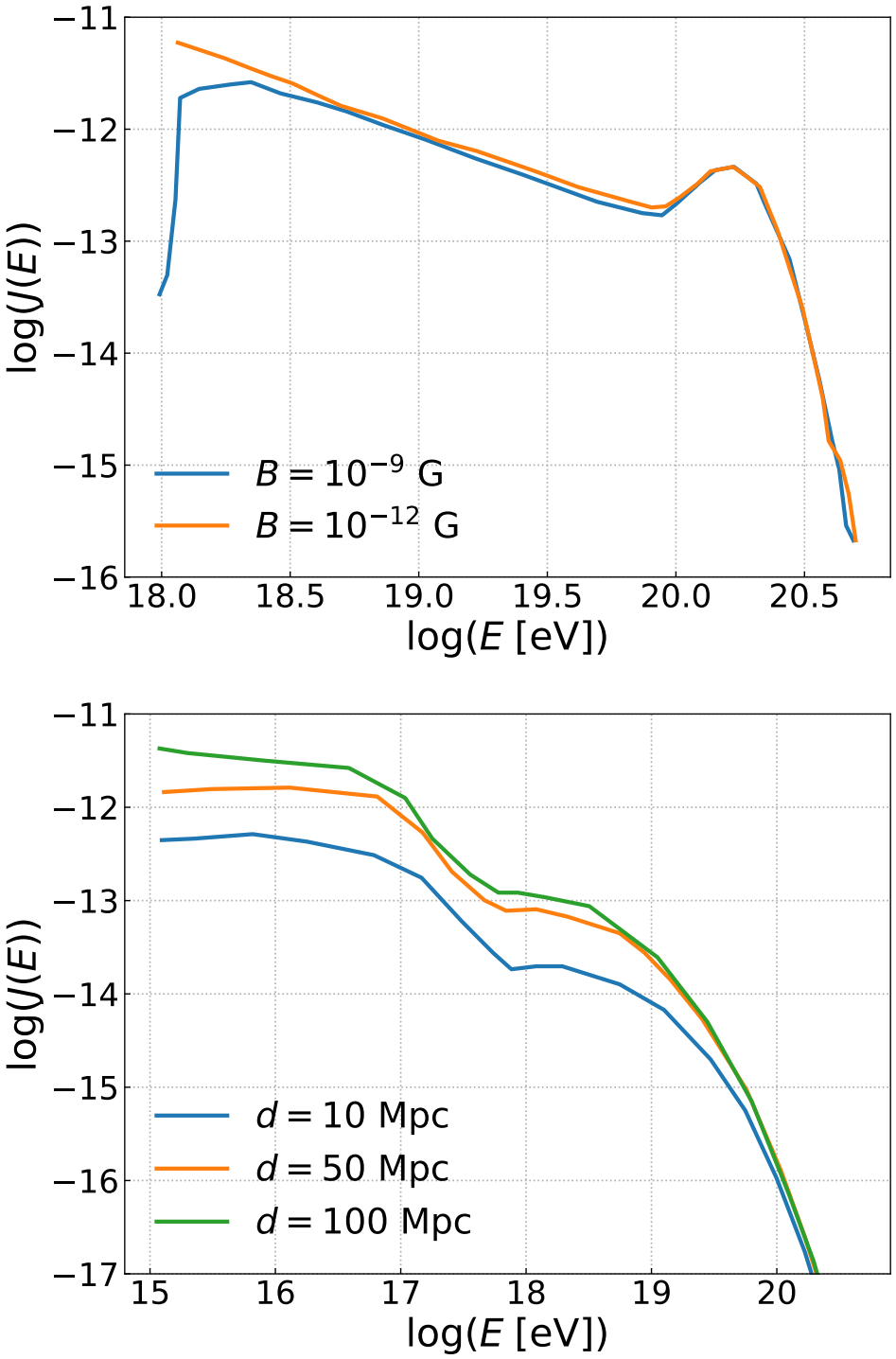

Figure B.4: Upper panel shows the suppression of CRs flux due to magnetic field at energy 10^{18} eV, for three values of the magnetic field $B = 10^{-9}$ and 10^{-12} G. Lower panel shows the flux of neutrinos arriving at different distances (d) from the sources. We note that the change of slope in the lower panels around $E \sim 5 \times 10^{17}$ eV is because above this energy, the interactions of CR with the CMB starts to dominate over the EBL. The bump is the upper panel has the same origin as in Fig. B.3.

Appendix C

Gamma-ray Flux Dependence with the CR Spectral Parameters

In the upper panel of Fig. C.1, we plotted the flux for different combinations of the parameters α and $E_{\max}$. We have constrained, in the lower panel of Fig. C.1, the combinations which are able to reproduce the current observed gamma-ray flux by the Fermi-LAT (Ackermann et al., 2015). The most suitable values for the spectral index are $\alpha = 2.0 - 2.5$, and for $E_{\max}$ the entire tested range $= (10^{16} - 10^{17})$ eV.

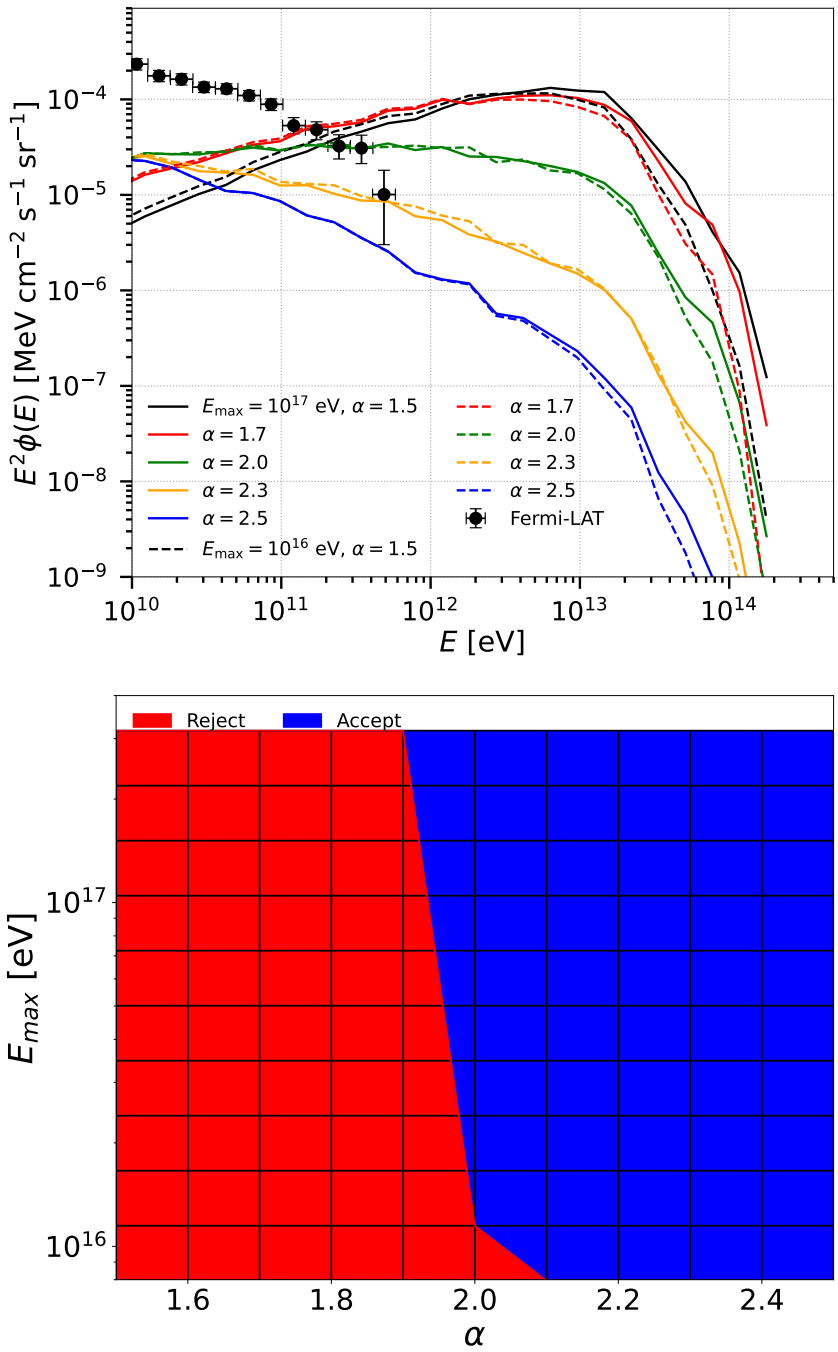

Figure C.1: Upper panel shows the flux for different combinations of of α and $E_{\rm max}$. In the lower panel blue color represents the combination of α and $E_{\rm max}$ which are suitable to reproduce Fermi-LAT gamma-ray flux (Ackermann et al., 2015). The red color region can overproduce the data for the energy bin $(300 - 600)$ GeV.

Appendix D

CRs Propagation of Different Composition of Primaries in the ICM

We here discuss the propagation of CRs of different chemical composition inside two individual clusters of masses $M \sim 10^{15}\ M_{\odot}$ (cluster 1) and $M \sim 2 \times 10^{14}\ M_{\odot}$ (cluster 2). We assume the power law index E^{-1} for the CR injection, with energies between 10^{14} and 10^{19} eV. We take into account all relevant photohadronic and photonuclear processes, namely photopion production, Bethe-Heitler pair production, photodisintegration during the propagation of CRs in clusters, as well as the adiabatic energy losses due to expansion of the universe (see Chapter 3). We consider the injection of protons, nitrogen, and iron nuclei, all with the same power, in three different positions in the clusters: the central region, 200 kpc and 1 Mpc away from the centre. These choices correspond to different scenarios of CR acceleration in clusters. They can be accelerated by sources near their central regions, or by shocks in their outskirts. The CR fluxes are computed by an observer located at the edge of the cluster, i.e., in a sphere of 1 Mpc radius around the center of the cluster for all injection scenarios. Neutrino fluxes are also calculated by the same observer, but only for the CR injection in the central region.

In Figs. D.1 and D.2, we show how the CR spectrum for different species depends on the position where the CRs are injected in the cluster. Fig. D.1 is for protons, and Fig. D.2 is for nitrogen, and iron primaries. From Figs. D.1 and D.2 one can see that the injected spectrum (E^{-1}) is clearly modified for all the three primaries due to interactions inside the clusters. The flux is presented in (arbitrary) code units, i.e., we did not normalize our flux with respect to the luminosity of the clusters. Higher-energy CRs can escape the cluster, whereas the lower energy ones remain trapped within it, suffering continuous

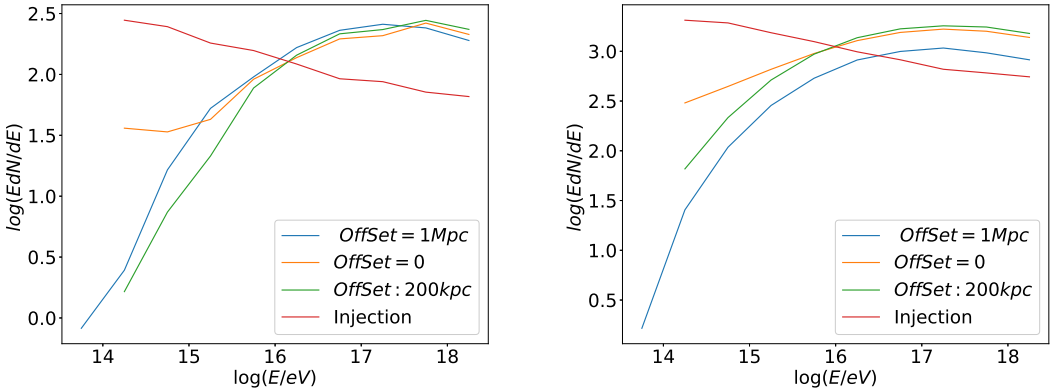

Figure D.1: Spectrum (in arbitrary units) of CRs for cluster 1 (left, $M \sim 10^{14}\ M_{\odot}$) and cluster 2 (right, $M \sim 5 \times 10^{14}\ M_{\odot}$). Here we assume only proton composition at injection: The lines in each plot correspond to: the injected spectrum (red), the flux for a CR source in the centre of the cluster (orange), at 200 kpc (green) and 1 Mpc (blue) away from the centre (Hussain et al., 2019)

electromagnetic cascading thus explaining the decrease of the flux of CRs at energies $E \lesssim 10^{16}$ eV (see also Alves Batista et al., 2018). Even very small magnetic field fluctuations in the ICM, can be enough for the confinement of the CRs in the very large volume of galaxy clusters for a time-period comparable to the age of the clusters themselves (Brunetti and Jones, 2014). This magnetic horizon effect effectively limits the energy of CRs that can escape from clusters, suppressing the contribution of the lower-energy ones. The spectrum of protons is entirely different from that of heavy nuclei (Fe, N) due to photo-disintegration and nuclear decay processes which are obviously important for heavy nuclei.

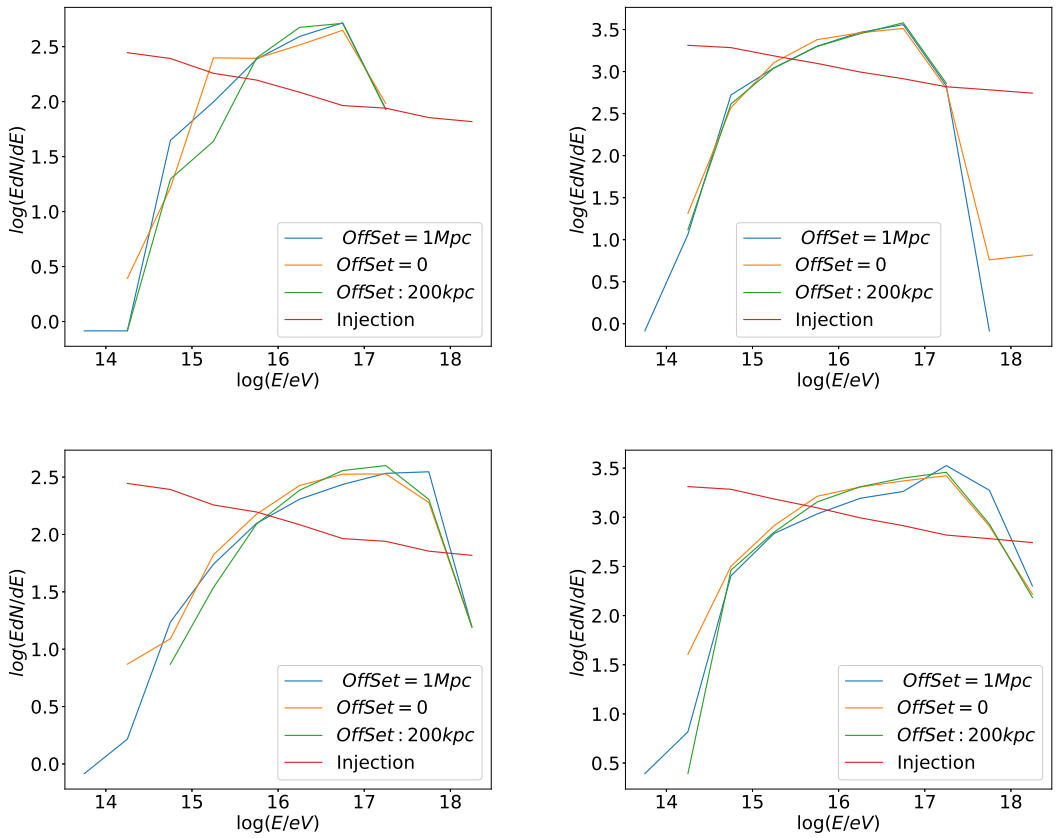

Figure D.2: Spectrum (in arbitrary units) of CRs for cluster 1 (left), mass 10^{15} $M_{\odot}$ and cluster 2 (right column), mass 2×10^{15} $M_{\odot}$. We assume different compositions at injection: iron (upper panels) and nitrogen (lower panels). The lines in each plot correspond to: the injected spectrum (red), the flux for a CR source in the centre of the cluster (orange), at 200 kpc (green) and 1 Mpc (blue) away from the centre (Hussain et al., 2019).